

ENERGY DEPOSITION MECHANISMS FOR PROTON- AND
NEUTRON-INDUCED SINGLE EVENT UPSETS
IN MODERN ELECTRONIC DEVICES

By

Michael Andrew Clemens

Dissertation

Submitted to the Faculty of the
Graduate School of Vanderbilt University
in partial fulfillment of the requirements

for the degree of

DOCTOR OF PHILOSOPHY

in

Physics

May 2012

Nashville, Tennessee

Approved:

Professor Robert A. Weller

Professor Robert A. Reed

Professor Marcus H. Mendenhall

Professor Sokrates T. Pantelides

Professor Volker E. Oberacker

To my children:
May you forever feel the need to discover

ACKNOWLEDGMENTS

I am indebted to many people who have helped me over the course of my graduate studies. First and foremost, I would like to express my deep appreciation and love to my wife, Michelle, for her tremendous encouragement and support. Without her, I certainly wouldn't be where I am today.

Much of the experimental portion of this work was made possible by the help and friendship of my colleague Nathaniel Dodds. From building and debugging the pulse height analysis system, to packing equipment and accompanying me on numerous trips to cyclotron facilities, his assistance was invaluable. I am also deeply appreciative of the advice and help I've received from my advisor, Prof. Robert Weller, as well as Profs. Marcus Mendenhall and Robert Reed. The assistance I've received from these three professors has been selfless and essential in my scientific endeavors. I would also like to thank Nick Hooten for his help and useful discussions. Additionally I would like to acknowledge my colleagues from Sandia National Laboratories, Marty Shaneyfelt, Paul Dodd, and Jim Schwank for their help in obtaining the diodes used in this study and for useful feedback in my work. I would like to thank Ewart Blackmore and Michael Trinczek for their help in using the facilities at TRIUMF, and also Steve Wender for his help in my experiment at the Los Alamos neutron beam facility. Steve went above and beyond what was required of him to make sure that I was able to obtain useful data, and I thank him for that.

The computational part of this work was conducted through Vanderbilt University's Advanced Computing Center for Research and Education (ACC-RE). Funding for this work was provided by the Defense Threat Reduction

Agency under grants HDTRA 1-08-1-0033 and HDTRA 1-08-1-0034, and in part by the NASA Electronics Parts and Packaging Program and the Department of Defense Science Mathematics and Research for Transformation (SMART) Scholarship for Service Program.

Lastly, I would like to thank my parents, Marc and Monica, for their examples of hard work and integrity, and for encouraging me throughout my life to do my best. Much of who I am I owe to them.

TABLE OF CONTENTS

DEDICATION	iii
ACKNOWLEDGMENTS	v
LIST OF TABLES	vii
LIST OF FIGURES	viii
I INTRODUCTION	1
II BACKGROUND	6
Radiation Environments	6
Space	7
Terrestrial Level	8
Single Event Upsets (SEUs)	9
Linear Energy Transfer	11
Critical Charge	14
Monte Carlo Simulation	15
Sensitive Volume Modeling for SEUs	17
Single and Multiple Bit Upsets	19
Proton and Neutron-Induced SEUs - Nuclear Reactions	21
III EXPERIMENTAL AND SIMULATION METHODS	27
Charge collection measurements	27
Pulse height analysis (PHA)	27
16 channel PHA system	33
Diode Structures	35
Particle Beam Experiments	39
Proton Irradiations	39
Neutron Irradiations	40
Time of Flight (TOF) Measurements	42
Description of TOF setup	42
TOF Calculation	43
Monte Carlo Simulations	46
Description of Simulation Tool	46
Uses of Simulation Tool	47
Nuclear Physics Models	48

IV MECHANISMS OF PROTON-INDUCED SINGLE EVENT EFFECTS	50
Introduction	50
Charge Collection Measurements	52
Monte Carlo Simulations	57
Model Validation	57
Proton-Induced Nuclear Reactions	60
Conclusions	63
V MECHANISMS OF NEUTRON-INDUCED SINGLE EVENT EFFECTS	64
Introduction	64
Charge Collection Measurements	66
SEU and MCU Simulations	68
Monte Carlo Simulations	68
Effect of W Overlayer on MCU Response	70
WNR and 14 MeV Neutron Spectra Compared	72
Effect of Neutron Energy on MCUs	78
Conclusions	81
VI CONCLUSIONS	83
A LINEAR ENERGY TRANSFER	85
Overview	85
Physics of LET	86
Accuracy of LET Theory	89
B MRED STANDARD MODE EXAMPLE CODE	91
C MRED SINGLE EVENT MODE EXAMPLE CODE	97
BIBLIOGRAPHY	107

LIST OF TABLES

1	Maximum Energies of Particles in Space	7
2	Alpha Sources Used for PHA Calibration	29
3	Hadronic Nuclear Physics Models in MRED	49
4	14 MeV Neutron-Silicon Reactions Producing Ionizing Secondaries . .	75

LIST OF FIGURES

1	Particle Abundance and Energy of Galactic Cosmic Rays	8
2	Terrestrial Neutron Energy Spectrum with JEDEC Fit	9
3	Importance of SEEs for Smaller Devices	10
4	Types of SEEs	11
5	LET in Silicon as a Function of Energy for Various Ions	13
6	Cosmic Ray Fluence vs. Energy/LET and Cyclotron Energy Ranges .	16
7	Illustration of a Single Sensitive Volume	17
8	Illustration of Nested Sensitive Volume	18
9	SBU and MCU Trends with Technology Nodes	20
10	Representation of a Proton-Induced MCU Event	21
11	Nuclear Emulsion Image of Cosmic-ray Tracks & Nuclear Reaction . .	22
12	Stages of an Inelastic Nuclear Collision	24
13	Block Diagram of PHA System	28
14	Measured Alpha Spectrum with PHA	30
15	Generating an Integral Cross Section Curve	32
16	Diagram of 16 Channel PHA System	34
17	Cross Sectional Diagram of Diode Overlayer Configurations	36
18	Top-Down Diagram of Diodes	37
19	Picture of PCB Holding the Diodes in Beamline	39
20	WNR, T4FP15L and Terrestrial Neutron Energy Spectra	41
21	Time of Flight vs Neutron Energy	45
22	Charge Deposition Cross Section from Howe <i>et al.</i>	51
23	90, 200 and 500 MeV Proton-Induced Charge Collection Measurements	52
24	Experimental Proton-Induced Fission Cross Section	54
25	500 MeV Proton-Induced Charge Collection Measurements at Different Angles of Incidence	55
26	500 MeV Proton-Induced Charge Collection Measurements at Front and Backside	56
27	Validation of Physics Models with Charge Collection Data	59
28	Calculated Angular Distribution of Secondary Products from Proton- Silicon Reaction	61
29	Calculated Angular Distribution of Secondary Products from Proton- W Reaction	61
30	Ratio of SEU Cross Sections from Normand and Dominik	66
31	Neutron-Induced Charge Collection Measurements with Diodes	67
32	Neutron Energy vs. Charge Collected Scatter Plots	68

33	MRED Validation with Neutron-Induced Charge Collection Measurements	69
34	Simulated SBU and 2BU Cross Sections for Devices with and without W Overlayers	71
35	Simulated 2-4BU Cross Sections for Devices with and without W Overlayers	72
36	Simulated SBU and 2BU Cross Sections for Devices Exposed to the WNR and 14 MeV Neutrons	73
37	Simulated 3-5BU Cross Sections for Devices Exposed to the WNR and 14 MeV Neutrons	74
38	Ratio of Simulated MCU Cross Section for WNR to 14 MeV Neutrons	75
39	Range and LET of Alphas in Silicon	76
40	Percentage of MCU Response for 2 to 6+BU	77
41	3-D Cross Section Plot for the 65 nm SRAM with Q_{crit} of 1.3 fC . . .	78
42	WNR Neutron Energy Spectrum	79
43	3-D Cross Section MCU Plots for Devices with a Q_{crit} of 5 fC	80

CHAPTER I

INTRODUCTION

Over the past 50+ years, computers have become increasingly powerful and ever-present, appearing in an increasing number of modern devices. The individual components of the integrated circuits (ICs) in computers have shrunk to sub-micron sizes following a well-known trend known as Moore's law [1]. While the shrinking of IC component size has effectively increased computer power, speed and lowered cost, the decrease in feature size has not come without consequences. One of the consequences for semiconducting devices has been an increased susceptibility to failure by a mechanism that was predicted about 50 years ago.

In 1962, Wallmark and Marcus [2] published a prediction that ionizing radiation would be able to upset the normal operation of electronic devices as their dimensions decreased with the advance of technology. They postulated that smaller devices would be more susceptible to cosmic ray radiation, and concluded that this would impose a lower limit on the size of silicon-based devices (interestingly, the minimum device volume they predicted was $10 \mu\text{m}^3$). Although it hasn't yet restricted the practical dimensions of electronic devices, the postulate of upset susceptibility increasing with smaller devices has proved generally true. However, it wasn't until the 1970's that this effect was observed. Anomalies in orbiting communications satellites were observed in 1975 by Binder *et al.* [3] who attributed the anomalies to cosmic ray radiation. In 1979, errors were observed by May and Woods [4] in ground-based DRAMs and CCDs which were attributed to alpha particles emitted by radioactive isotopes of uranium and thorium in parts-per-million levels in packaging materials. Since that

time electronic devices have shrunk in size by many orders of magnitude (beyond $10 \mu\text{m}^3$) and the interest in radiation effects has grown accordingly, particularly for space-bound electronics.

Of the types of radiation effects that plague modern-day electronic devices, single event effects (SEEs - radiation effects caused by a single particle strike) have become increasingly important. A subset of SEEs, the single event upset (SEU), is the topic of this dissertation. This dissertation presents new research which furthers the understanding of mechanisms behind SEUs in modern-day devices, both for devices exposed to the natural space radiation environment and that of the terrestrial level.

In space, the dominant form of radiation is energetic protons. However, because of their single electric charge, most of the energetic protons found in space do not have a high enough linear energy transfer (LET - a measure of how much charge an energetic particle will deposit in a material it traverses) to cause SEUs through direct ionization. Instead, proton-induced SEUs are typically caused by secondary particles that result from proton-nuclei collisions in materials in or near a sensitive node in the semiconducting device. These secondary particles are either nuclei recoils from elastic collisions, or nuclear fragments from inelastic collisions. In either case, it is the heavy-ion secondary products that are often the mechanism of proton-induced SEUs. Thus, accurate computer simulation of proton-induced radiation effects becomes, in part, a question of correct nuclear physics modeling, as well as particle transport and energy deposition calculations.

The role of high atomic number (high-Z) materials found in modern-day devices, such as tungsten (W), in proton-induced radiation effects is not fully understood. Howe *et al.* [5] published Monte Carlo calculations which predicted that, when irradiated with protons, devices containing W overlayers would have the same radiation response as devices with similarly placed oxide layers. Conversely, Schwank *et al.* [6]

observed proton-induced radiation effects in static random access memories (SRAMs) which could not be explained by only considering proton-silicon reactions. Through simulations, they concluded that the observed effects were possibly caused by higher-LET secondary particles from proton collisions with high-Z materials in the SRAMs.

Chapter IV of this dissertation presents new experimental and Monte Carlo simulation data which demonstrate that the presence of W in a device can significantly increase the effects of proton-induced radiation due to proton-induced fission in W. Proton-induced fission is shown to occur in W for incident protons with sufficiently high energy ($>\sim 100$ MeV). It is shown that the high-LET secondaries from proton-induced fission are sufficiently ionizing to cause the effects reported by Schwank *et al.* [6]. Additionally, it is found that the prediction reported by Howe *et al.* is inaccurate due to the miscalculation of proton-induced fission in W by the nuclear physics model used in their work. With the increasing diversity of materials found in today's semiconductor devices, it is apparent that nuclear physics models used for radiation effects prediction must not only model proton-silicon interactions correctly, but also proton interactions with high-Z materials.

At a terrestrial level, one of the major causes of radiation effects in electronics is neutrons originating from cosmic-ray particles colliding with nuclei in atmospheric atoms. Because of their neutral charge, the neutrons produced in such collisions are able to reach the earth's surface in a significant number spanning energies from less than 1 eV to up to 100s of GeV [7]. In recent years, neutron-induced radiation effects have become a major concern for the reliability of modern and developing semiconductor technologies [8,9]. While much research has been done on the subject matter, the effect that high-Z materials can have on neutron-induced SEUs has not been investigated.

Chapter V of this dissertation presents experimental and Monte Carlo simula-

tion data which show that neutron-induced fission in W can increase the effects of terrestrial-level radiation. Like proton-induced fission, these events only occur for high-energy neutrons and can also produce high-LET secondary particles. However, the data shown here suggest that the presence of W would only significantly increase neutron-induced SEUs only for radiation hardened devices resistant to SEUs. This is due, in part, to the relatively small number of high energy neutrons which are able to cause neutron-induced fission in W.

Because of the natural neutron radiation at a terrestrial level, computer chip makers must now qualify their electronic parts that are to be used in an unshielded environment. It is ideal to qualify parts in a radiation environment that is as similar to the natural one as possible. There are a few facilities that provide accelerated neutron testing with an energy spectrum similar to that of the natural terrestrial environment, among them is the Los Alamos National Laboratories' Weapons Nuclear Research (WNR) facility [10]. However, due to cost and accessibility, alternative test methods for neutron vulnerability of electronic devices have been investigated [11, 12]. One of the more prominent alternatives is using a monoenergetic 14 MeV neutron beam generated by a fusion reaction of deuterium and tritium [13]. How well the 14 MeV neutron beam is able to assess radiation susceptibility of an electronic device is the topic of much debate and research. In [12], a comparison was made of the SEU cross sections measured using a 14 MeV neutron source and the WNR neutron spectrum. It was observed that, for multiple static random access memories (SRAMs) from various technology nodes, the SEU cross section measured using 14 MeV neutrons was within a factor of two of that measured using WNR neutrons. The smallest technology node measured in this study was 90 nm, and the analysis was only done for single bit upsets (SBUs) and not multiple cell upsets (MCUs - when more than one bit is upset by a single incident neutron).

Chapter V of this dissertation presents new Monte Carlo simulation results which compare the SBU and MCU cross sections for a 65 nm SRAM irradiated with the WNR neutron spectrum and 14 MeV neutrons. These results show that the SBU cross section caused by WNR and 14 MeV neutrons in this device agree to within factor of two, in agreement with the trend shown in [12]. However, the 14 MeV neutrons under predict the MCU cross section when compared with the WNR neutrons, for the device considered here. The mechanism behind the 14 MeV-neutron-induced MCU events is investigated and shown to be secondary alpha particles from inelastic neutron-silicon collisions. These secondary alpha particles have a high enough LET and range to cause multiple bits to upset in the SRAM at a significant cross section. Higher-energy neutrons in the WNR neutron spectrum are able to cause MCU events through heavy ion secondary particles and silicon nuclei recoils. These secondaries are able to deposit more charge over a longer range. For this reason, 14 MeV neutrons under predict the WNR neutron MCU cross section for the device considered here.

The original research which is presented in this dissertation spanned the years 2008-2011. The results of this work have been presented at the Nuclear and Space Radiation Effects Conference over the course of those years and published [14,15] in the peer-reviewed journal *IEEE Transactions on Nuclear Science*, the premier journal for radiation effects publications.

CHAPTER II

BACKGROUND

This chapter gives an introduction to and overview of the study of radiation effects on electronic devices, focusing on the physics and modeling techniques relevant to the research presented in this work. All of the radiation-effects-specific terms that are used in later chapters are defined in this chapter as well. The mechanisms of proton- and neutron-induced single event upsets, which is the topic of this document, can be understood, and are placed in context, by the concepts discussed in this chapter.

Radiation Environments

Companies which design and make electronic components must understand the natural radiation environments which those parts will encounter during their lifetime of use. In many cases, these companies must also test their parts by irradiation with man-made particle accelerators. Historically, this has been more critical for parts designed for satellites and aircraft because of the comparatively harsh radiation environment in low-earth orbit and at aircraft cruising altitudes. However, in recent years, even parts made for use at sea level have been sufficiently sensitive to upset that they must be qualified for that radiation environment by irradiation with neutrons. This section discusses the radiation environments found in space, and also at a terrestrial level.

Table 1 Maximum Energies of Particles in Space

Particle Type	Maximum Energy
Trapped Electrons	10s of MeV
Trapped Protons & Heavy Ions	100s of MeV
Solar Protons	GeV
Solar Heavy Ions	GeV
Galactic Cosmic Rays	TeV

Space

The radiation environment outside of the earth’s atmosphere contains a wide range of particle types and energies as shown in table 1 [16]. An in-depth discussion of the radiation environment in space can be found in refs [17–22], however, for the scope of this work, it is sufficient to understand the species and energies of radiation that a space-bound system could encounter. The types of radiation that exist are: 1) trapped particles in the earth’s magnetic field (forming the Van Allen belts), 2) energetic particles emitted by the sun (solar particles), and 3) particles originating from outside our solar system (galactic cosmic rays (GCRs)). The heavy ion population in the GCR spectra is represented by most elements in the periodic table, but only elements up to iron are found in significant amounts (see Fig. 1A) [17]. The energetic heavy ions ($Z > 2$) and alpha particles are rare in comparison to protons, and comprise only about 1% of the total GCR flux. Fig. 1B shows the flux versus kinetic energy for the different GCR ions. Each ion species has a large range of energies spanning several orders of magnitude, but all fluxes peak at roughly 500 MeV/u [5, 23].

Although these energetic particles don’t reach the terrestrial environment in appreciable amounts without interacting with the atmosphere, the secondary, tertiary,

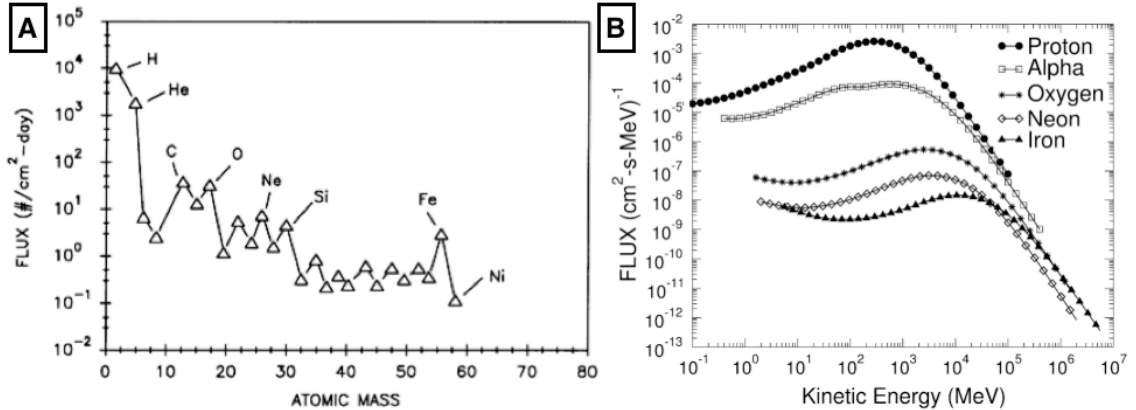


Figure 1 A) Particle composition of galactic cosmic rays [17]. Note that hydrogen and helium nuclei (i.e., protons and alpha-particles) account for the vast majority of GCR flux, while heavy ions comprise only about 1%. B) Particle flux as a function of energy [5, 23]. Note the peak flux at roughly 500 MeV/u for each particle.

etc. neutrons from nuclear interactions can and do reach airplane electronics and even sea-level systems because they don't interact electromagnetically. These particles, in addition to man-made and natural radiation sources near devices [4] make radiation effects an important factor even when designing ground-based systems.

Terrestrial Level

At sea level, electronics are constantly bombarded with a flux of energetic neutrons that span a wide range of energies as shown in Fig. 2. The data in Fig. 2 are experimentally measured and reported in [7]. The Joint Electronic Devices Engineering Council (JEDEC), which is a semiconductor engineering standards organization, has published a fit to these data that is often used as a standard for estimating the terrestrial neutron spectrum flux [24]. The JEDEC standard neutron flux is also shown in Fig. 2 for comparison.

Although the terrestrial neutron spectrum spans a wide range of energies, only neutrons with an energy between 1 MeV and 10 GeV are relevant to this work. The

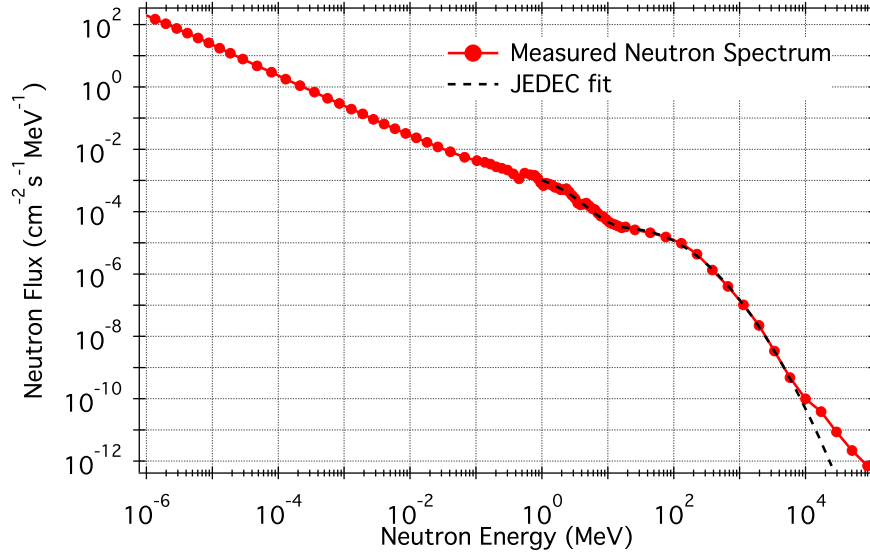


Figure 2 Measured terrestrial neutron energy spectrum [7] plotted with the published JEDEC fit to the data [24].

lower-energy neutrons (< 1 MeV) are not considered here because they do not have sufficient energy to produce a secondary particle in a device which has a high enough LET to cause a single event upset. The higher-energy neutrons are not considered here because their flux is sufficiently low that effects due to these neutrons are so rare as to be negligible.

Single Event Upsets (SEUs)

Radiation effects research focuses on either the sustained degradation in a device over a long period of radiation exposure (total dose), the degradation of a device due to displacement of atoms in the silicon lattice due to nuclear collisions (displacement damage) or the errors due to a single strike of an energetic ion in a device (single event effects (SEEs)) [25–27]. The two effects which are most commonly the subject of research are total dose effects and SEEs. Historically, total dose effects have been the most prominent radiation effect in devices. However, as technology has advanced,

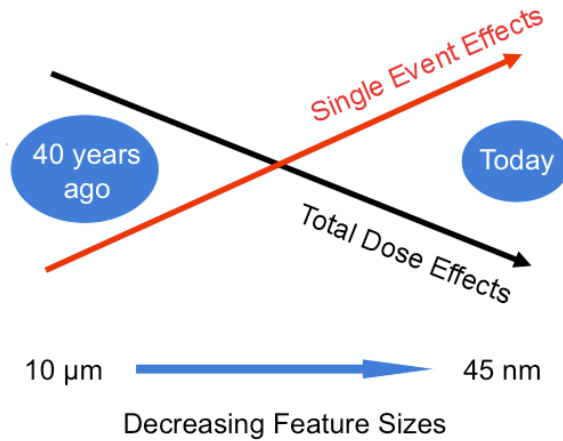


Figure 3 Smaller devices at lower voltages with less charge movement have resulted in increased single event effects [28].

SEEs have become a more important consideration for radiation effects research. This is partially due to the thinner oxides in transistors and improved oxide/silicon interfaces which reduce the effects of total dose. But more importantly the decreased size of devices, along with the reduced operating voltages, have increased the importance of SEEs [28](see Fig. 3).

The various ways in which a single particle strike can cause problems in semiconducting devices is reflected in the various classifications of SEEs. Fig. 4 shows several of the different classifications of SEEs, both hard and soft errors, which are currently researched. The type of SEE which is the subject of this work is the single event upset (SEU), both for single and multiple bit upsets (SBU and MBU). Although single event transients (SETs) may cause SEUs, SET research is typically separate from SEU research and often studies transient propagation on a circuit level.

In digital devices, SEUs are caused by a single incident particle causing sufficient charge to be deposited in one or more sensitive nodes in a device that there is a bit flip, and thus a soft error. Although there exist techniques which can mitigate these soft errors, these can increase memory complexity and access time and may not

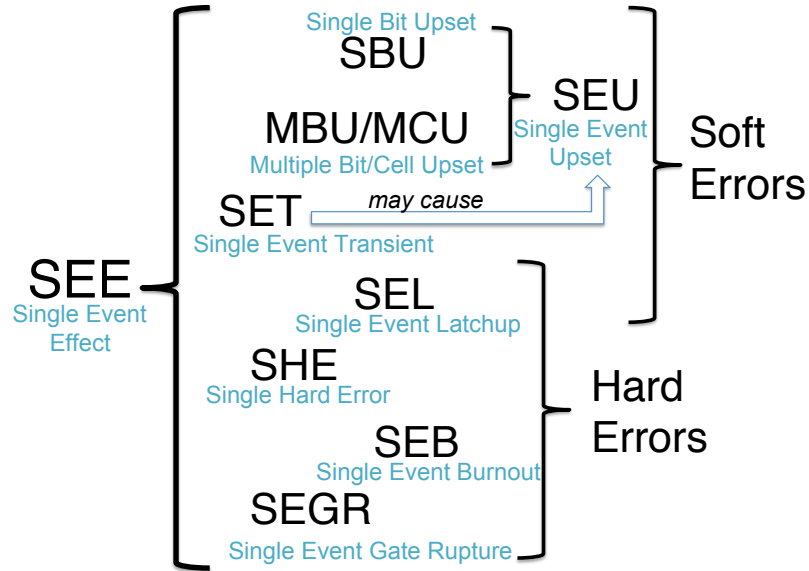


Figure 4 Different types of SEEs which are actively researched with their corresponding acronyms. Single Event Latchup can cause both soft and hard errors.

be suitable for all devices [29]. Additionally, if multiple bits are flipped by a single particle strike (MBU) these mitigation techniques can fail. Thus, SEU research is ongoing and understanding the mechanisms of how SEUs occur is essential.

Because electrons are usually a concern only for total dose and spacecraft charging [30, 31], they usually aren't considered for SEU analysis. It is typically the protons, alphas and heavy ions that are a major concern for space, and neutrons for terrestrial-level environments. The following section will describe the mechanism of how energetic particles can deposit charge, in order to understand how these particles can produce SEUs in devices.

Linear Energy Transfer

Linear energy transfer (LET), or stopping power, is defined as the rate at which energy is transferred from an energetic charged particle to a material through means

of an electromagnetic interaction between them. This happens through a series of collisions between the incident particle and the atoms in the material. The result is either the excitation or the ionization of the target atom, and a loss of kinetic energy for the incident particle. The mathematical expression for LET is given by the Bethe-Bloch equation [32]:

$$LET = K z^2 \frac{Z}{A} \frac{1}{\beta^2} [L_0(\beta) + zL_1(\beta) + z^2L_2(\beta)\dots] \quad (1)$$

where K is a constant, z is the atomic number of the incident ion, Z and A are the atomic and mass number of the target atoms, and β is v/c for the incident ion. The term in brackets is the expansion of the stopping number, $L(\beta)$ which is actually a function of various terms other than β . The origin of Eq. 1 is covered in depth in Appendix A. LET is most commonly expressed in units of $\text{MeV}\cdot\text{cm}^2/\text{mg}$.

In semiconducting materials, charge is generated when enough energy is transferred to the material to excite electrons from the conduction band to the valence band creating an electron-hole pair. In silicon (the semiconductor of choice for most modern electronic devices), the average energy required to generate an electron-hole pair is 3.6 eV [33]. Thus the conversion from energy transferred (as calculated with Eq. 1) to charge deposited is 22.5 MeV/pC .

If the density of the material, ρ , that the energetic particle is traversing is known, then one can multiply LET by the density to give energy loss in units of $\text{MeV}/\mu\text{m}$. Using this we can calculate the amount of charge per unit length that is deposited on average in a material for a given LET. For example, a particle with an LET of 97 $\text{MeV}\cdot\text{cm}^2/\text{mg}$ will deposit on average 1 $\text{pC}/\mu\text{m}$ in silicon ($\rho = 2.33 \text{ g}\cdot\text{cm}^{-3}$), assuming the LET doesn't decrease appreciably over the distance in question.

It is critical to understand that the energy deposition process is highly stochas-

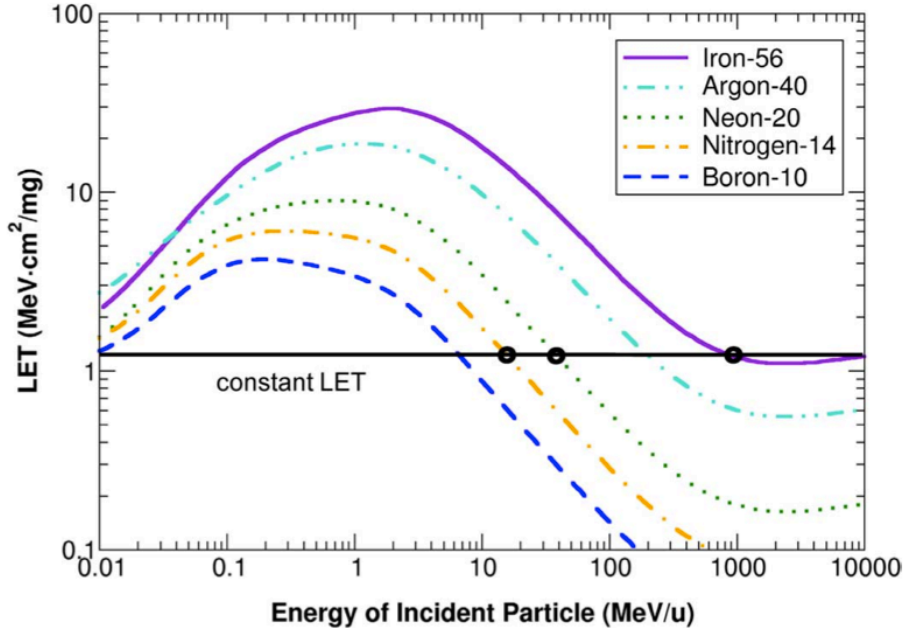


Figure 5 LET in silicon as a function of energy for various ions over a wide range of energy. Note that the horizontal axis is in units of MeV/u. From [34].

tic due to the quantum mechanical nature of the particle-electron collisions. Thus, the calculated LET value gives the most probable amount of energy lost/charge deposited over the track of the ion, and actual measured values will result in a Gaussian distribution around that value. This emphasizes that good counting statistics are necessary when performing any experiments or Monte Carlo calculations concerning charge deposition.

Fig. 5 shows LET in silicon as a function of energy for several heavy ions [34]. Note that even though for a given particle energy LET increases with atomic number (as one would expect given Eq. 1), particles with different atomic numbers and energies can have the same LET value. Another point to note from Fig. 5 is that as particle energy decreases down to about 1 MeV/u, the LET value increases. That is, as the particle slows down in the material it begins to lose energy more rapidly. The reason for the drop in LET for low energies is that the particle cannot lose energy as rapidly

simply because it doesn't have very much energy.

How much charge is deposited by an incident particle in a sensitive volume of a device is dependent on the LET of the particle as it traverses the sensitive volume. Whether or not an SEU occurs depends not only on the amount of charge deposited, but also on the critical charge of the sensitive node. Critical charge is discussed in the following section.

Critical Charge

When an energetic particle passes through a sensitive part of a semiconducting device and deposits energy, it creates electron-hole pairs which can be swept away from each other by an existing electric field in the area. These collected electrons and holes constitute the collected charge from the single event. This collected charge can cause a SEU in the device if the collected charge is equal to or larger than a threshold value. This quantity is called the critical charge, Q_{crit} , and is dependent only on the device, not the radiation environment [35]. Q_{crit} can be extracted from experimental measurements or circuit simulation methods [36] and in practice, it is often used as a figure of merit when comparing different devices and technologies. In general, as devices are scaled down in size (with nothing else changed but the size of the components), the Q_{crit} decreases and single event strikes that weren't a problem for larger devices become a serious issue for their smaller counterparts (see Fig. 3). There are many techniques for radiation hardening of these smaller devices that can, in effect, increase the Q_{crit} and effectively decrease the SEU rate in newer technologies [37, 38].

It is important to note that the Q_{crit} of a device is not a well-defined quantity in that it can vary for different sensitive volumes in a device, and can even vary for the same sensitive volume depending of the timing of the strike in relation to the circuit

dynamics [27]. The estimated Q_{crit} is then a best estimate of the amount of charge necessary to cause an SEU. In Monte Carlo simulations of SEUs, Q_{crit} is necessarily used to determine whether an incident ion causes an SEU or not. Therefore, Monte Carlo simulation techniques shouldn't be used without understanding the limitations of the Q_{crit} value.

Monte Carlo Simulation

The high cost of putting electronics into space, only to have them fail when introduced to the harsh radiation environment that exists there has led to techniques for predicting SEE radiation susceptibility. The most predominant techniques are: 1) testing devices at ground-based cyclotron facilities and 2) using Monte Carlo computer simulations to predict SEU rates. A handful of cyclotron facilities exist that are typically used for SEE testing, including cyclotrons located at Lawrence Berkeley National Lab [39], Texas A&M University [40], and Indiana University [41]. While there are a few facilities that are capable of producing beams of ions with energies at or near the energy of galactic cosmic ray maximum flux, the beamtime at such facilities is expensive and often not available.

Fig. 6 shows the energy range that is typically available at these facilities superimposed on the galactic cosmic ray spectra for iron. It is important to note that while these facilities are only able to produce 1-100 MeV/u ions, they are in the range of highest particle LET. It is clear from Fig. 6 that it is impossible to test parts in the same radiation environment that they will be exposed to in space, and thus very difficult to predict exactly how a part will react to the harsh radiation environment found there.

JEDEC has published guidelines for SEE testing of parts using energetic heavy ion or proton beams at existing cyclotron facilities in order to best qualify parts [24, 42].

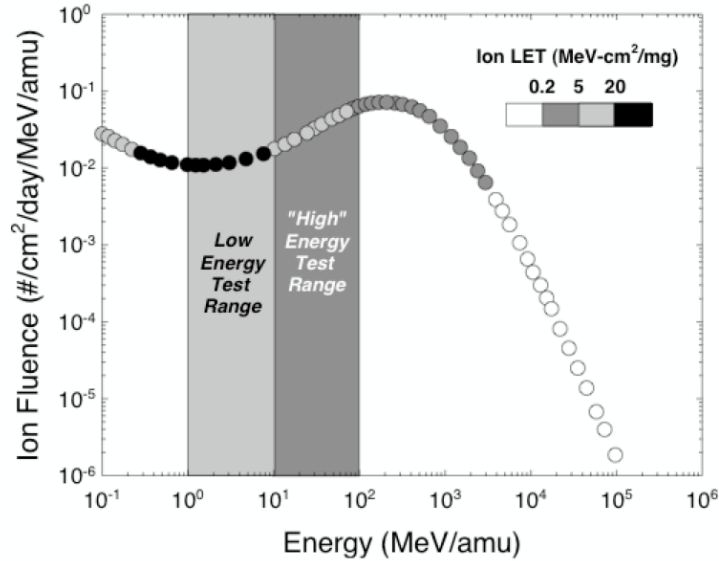


Figure 6 Galactic cosmic ray iron spectrum vs. energy with LET denoted by symbol shading. Ion energies available at typical ground-based SEE testing facilities range from approximately 1-100 MeV/u [38].

These test methods are designed to give a best estimate of the SEU rate of the devices using the available facilities. However, these test methods are unable to give insight into the mechanisms which cause SEUs. In order to understand the mechanisms behind SEU events, one must design custom devices or turn to computer simulation.

Because the deposition of energy in a material is stochastic in nature, computer modeling of SEUs is done using Monte Carlo methods. Monte Carlo simulations rely on repeated calculations using a random number to vary the result with the physical parameters of the problem. For the SEU calculations done in this work, the tool called Monte Carlo Radiative Energy Deposition (MRED - commonly pronounced, “Mister Ed”) is used [43]. In this tool, the a 3D model of the device is created and the incident radiation is specified in its type, energy and direction. The radiation is transported through the device, losing energy along its trajectory by depositing energy in the material or by creating secondary particles. These secondary particles are either caused by collisions with electrons (creating delta-rays) or by collisions with

nuclei, and these particles are also transported through the device, along a trajectory, depositing energy. The physics models involved in MRED will not be discussed here, but are discussed in section III. When simulations are run in MRED, the number of incident ions must be high to obtain statically significant calculation, just like in an experiment. An SEU is determined to occur if the amount of energy/charge deposited, by either the incident particle or by a secondary particle, in a sensitive volume exceeds the Q_{crit} of the device. The following section describes how the sensitive volumes are defined in a device.

Sensitive Volume Modeling for SEUs

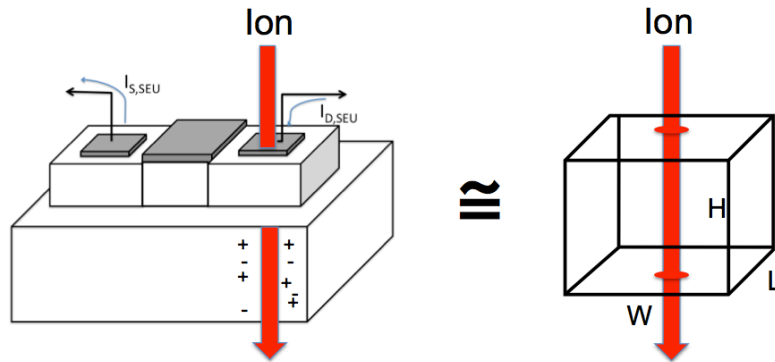


Figure 7 Illustration of placement of a SV below the drain node of a transistor. From [36].

For older technologies with larger device dimensions, it is possible to describe the sensitive volume (SV) of the device with a single rectangular parallelepiped (see Fig. 7). The exact dimensions of the SV are often found by irradiating the device with heavy ions whose LET value will be constant while traversing the SV. The location of the SV is determined by knowing the physical dimensions of the device, although actual placement of the SV isn't critical for technologies whose sensitive nodes aren't closely spaced, and the probability of multiple nodes being upset by a single ion strike

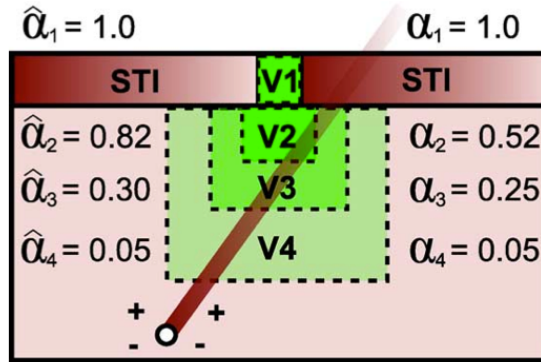


Figure 8 Illustration of nested sensitive volumes at one sensitive node. The different volumes have different charge collection efficiencies, $\hat{\alpha}$. Because the volumes are nested, the actual assigned charge collection efficiencies, α , are smaller. From [46].

is low. An example is shown in Fig. 7 where the SV is positioned below the drain node of a transistor as a plausible location of charge collection [36]. All of the energy deposited in this volume from a single particle strike, as calculated with MRED, is converted to charge (using 22.5 MeV/pC for silicon [33]) and this charge is compared with the Q_{crit} of the device to determine if the strike results in an SEU. This is repeated many times, as per the Monte Carlo method, to obtain a calculated SEU cross section.

Despite the success of the single SV model in calculating SEU rates for older technologies and large devices, it fails to account for an observed spacial variation in charge collection efficiency [36, 44, 45]. A proposed solution to this shortcoming, which has had success, is to incorporate multiple, nested sensitive volumes of different sizes and charge collection efficiencies for each sensitive node [36, 46]. An illustration of a nested sensitive volume from [46] is shown in Fig. 8. Here each volume is given a different size, and charge collection efficiency, $\hat{\alpha}$, as defined using experimental heavy ion induced SEU cross sections. The details of how the sensitive volumes are defined are found in [46].

In this dissertation, a calibrated nested sensitive volume model of a 65 nm SRAM is used to perform MRED calculations of SEU cross section. This is done both for single and multiple bit upset events from a single particle strike. The following section will describe single and multiple bit upsets.

Single and Multiple Bit Upsets

As technology has scaled down, the size of a device's SV has, in general, also decreased, and the spacing between two sensitive nodes in a device has decreased as well. Additionally, the Q_{crit} of devices has decreased. Together, these factors have increased the probability of an event where a single particle strike can cause sufficient charge to be deposited in two or more SVs to cause a coincident upset. These coincident upsets on multiple SVs are called multiple bit upsets (MBUs) or multiple cell upsets (MCUs). Although these two terms are sometimes used synonymously, there is a somewhat subtle, but important, difference between them. A single bit upset (SBU) occurs when one bit/cell is upset by a single particle strike. An MCU occurs when multiple bits/cells are upset by a single incident particle. A MBU occurs when the multiple bits/cells that are upset are in the same data word [24, 47]. Thus the calculated MCU cross section can be considered a worst-case MBU cross section, depending on word bit placement. Because a Monte Carlo calculation of an MBU cross section would necessarily make some assumptions about the word bit placement of the device (which can vary) all of the calculations done in this work are of MCU cross sections.

In the past, the term SEU has been used synonymously with SBU because MBU rates were low, or nonexistent for older technologies. Thus, the terms SBU and SEU are often used interchangeably, even though an MBU is a type of SEU. Fig. 9 shows how SBU and MCU probabilities have changed with Intel's different technology nodes.

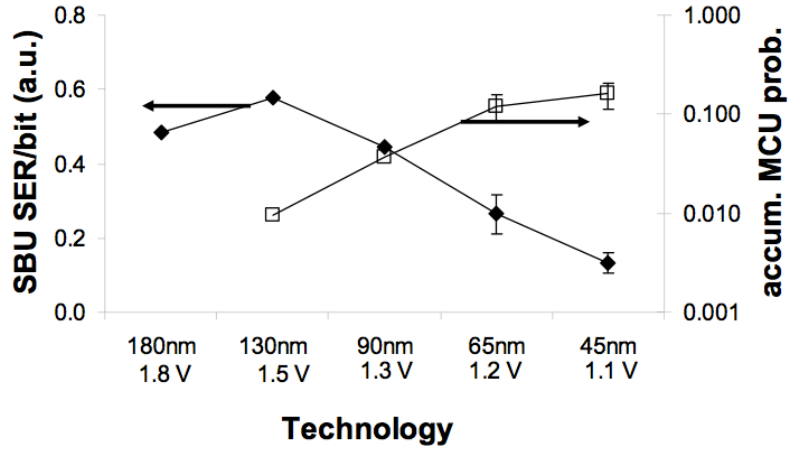


Figure 9 The neutron-induced SBU and MCU trends with Intel’s 180 nm to 45 nm technology nodes. As the technology has scaled down, the SBU rate has decreased while the MCU rate has increased [48].

The smaller technologies show a lower probability for SBU events. This is due to the decrease in SV size with smaller devices. Note that this is scaled per bit, so even though SBU/bit number has decreased, the number of bits in a device has increased so as to cause the total SBU rate to increase [48]. Fig. 9 also shows that the MCU probability has increased by an order of magnitude (note the log scale on the right) from the 130 nm node to the 65 nm node. This emphasizes the need for testing newer devices for MBUs.

MBUs and MCUs can occur by a single ionizing particle passing through the sensitive region of more than one cell and depositing enough charge in each cell to cause multiple cells to upset. For incident protons and neutrons, this ionizing particle is a secondary particle, like the one shown causing an MCU event in Fig. 10. In the figure, the incident proton undergoes an inelastic nuclear reaction with a silicon nucleus near a SV. Among the secondary particles generated is an energetic oxygen which is able to deposit charge in several SVs. The device being simulated is a 130 nm SRAM, and each SV is a single rectangular parallelepiped [49]. Events like

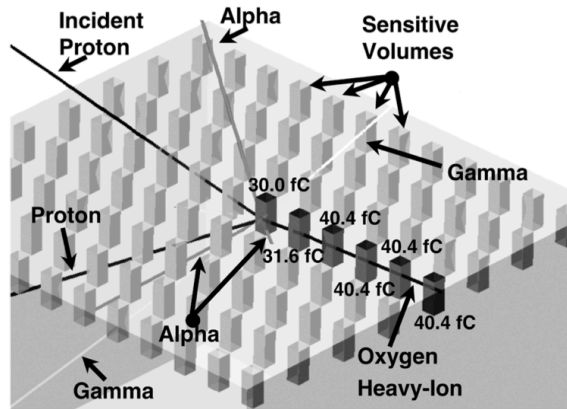


Figure 10 Representation of a MCU event in a 130 nm SRAM caused by an oxygen recoil from a proton-silicon nuclear collision. From [49].

the one shown in Fig. 10 illustrate the need to understand nuclear collisions in order to gain insight into the underlying mechanisms of SEUs, particularly for ones caused by protons and neutrons. The following section discusses nuclear collisions and their role in proton- and neutron-induced SEUs.

Proton and Neutron-Induced SEUs - Nuclear Reactions

Eq. 1 shows that LET scales with z^2 , and inversely with β^2 . Because β^2 scales classically with energy/amu, lower- Z ions and highly energetic ions will have lower LET values and will thus deposit less charge in materials. However, this does not mean they can be excluded in SEU studies. Protons, neutrons, and highly energetic heavy ions can still produce significant upset rates due to indirect interactions. These particles can undergo inelastic nuclear collisions (see Fig. 11B) with materials in and surrounding a device, producing heavier and/or less energetic secondary particles that can have a higher LET than the primary ion [38, 50–53]. Fig. 11 shows charge deposition from energetic particles as recorded by nuclear photographic emulsions.

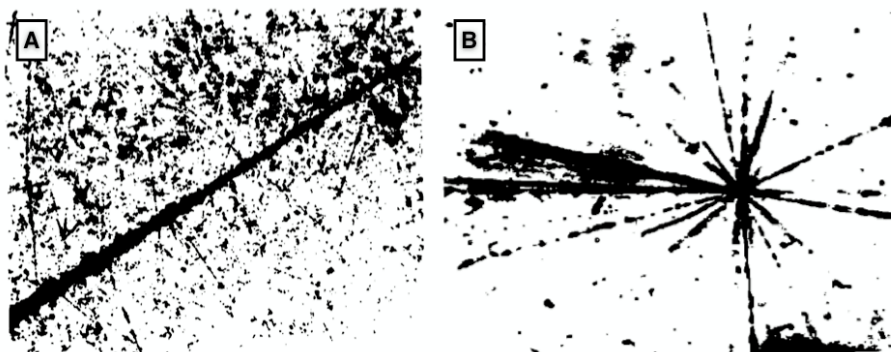


Figure 11 Cosmic-ray trajectories recorded by nuclear photographic emulsions flown in space and subsequently developed: A) track of heavily ionizing particle, B) inelastic nuclear reaction and secondary particle tracks [53].

Fig. 11B captures a nuclear event between the incident ion and a nuclei, note that the largest concentration of charge deposition is along the trajectory of a recoiling nuclear fragment.

Since these nuclear collisions are rare and difficult to simulate, they were historically excluded from SEU rate computer simulations. However, computational models which exclude the effects from secondary particles for space applications have been seen to underestimate SEU rates by over two orders of magnitude [54]. For radiation-hardened (rad-hard) devices, this is an especially significant issue. A rad-hard device may have a Q_{crit} that is large enough that high-energy, low-LET particles don't deposit enough charge to cause an SEU, while secondary products from an inelastic nuclear collisions of these particles and nuclei do [55]. It is apparent that when building computational physics codes to simulate SEUs that correct physics models are necessary to simulate these nuclear reactions.

When dealing with nuclear physics models, it is important to bear in mind that models are simplified imitations of the real thing. As scientists began to experimentally observe the properties of the nucleus, they invented simple models to describe it, based on their experience with other systems that demonstrated similar properties.

For example, the similarities seen between the interaction of protons and neutrons in the nucleus of an atom and the interactions of atoms in liquids gave rise to the liquid drop model [56] of the atomic nucleus. As experimental nuclear physics expanded the knowledge of the nucleus, new models were created to explain the new properties observed. For example, the shell model [57] of the nucleus.

Because models are not typically created by a rigorous derivation from first principles, but rather based on observation and analogy, the understanding that can be gained from models is often qualitative in nature, particularly when dealing with many-body problems. Because nuclear reactions can involve a large number of particles and are extremely complicated in nature, models shall never achieve an exact solution. A nuclear reaction model is thus a simpler physical system whose properties we can understand and calculate more easily, and possibly even visualize. It is a first order approximation to the nuclear system and can be further refined to make it approach reality [58]. However, it will not be able to reproduce all nuclear parameters perfectly. This could only be achieved by solving the original quantum many-body problem, which is too complicated and time consuming even for modern-day computers. A given nuclear physics model will provide a description of the set of properties upon which it is based. It cannot assure us an accurate description of other properties that haven't been experimentally observed. Thus models are in constant need of validating, refining and perhaps even merging with alternative models which accurately describe a separate set of properties.

There exist multiple physics models that have been developed to understand the nuclear fragmentation process. These models vary in complexity and popularity. The approach that has been implemented in most current computer simulation models involves a multiple stage approach with anywhere between two and five different stages [59, 60], and are based on experimental observation of particle emissions from

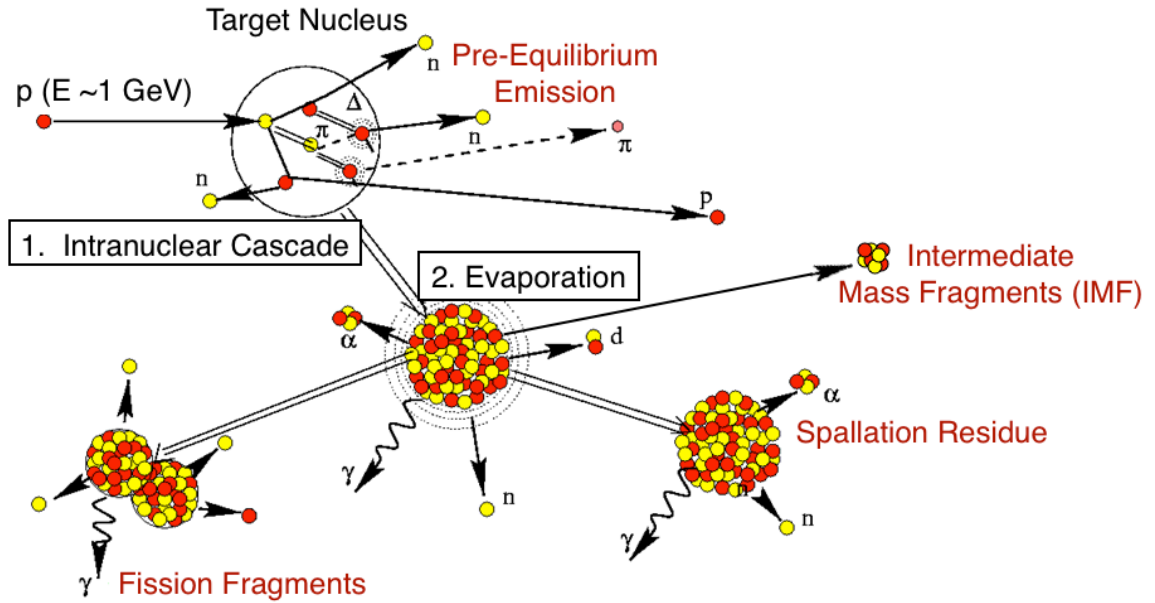


Figure 12 Illustration of the stages of an inelastic nuclear collision, and the secondary products created.

nuclear reactions [61]. The following paragraphs describe two generalized stages that are common to most codes and describe the overall process from a high level. The two stages, along with the types of nuclear fragmentation products, are depicted in Fig. 12.

The first stage is often called the intranuclear cascade. In this stage, the incoming particle enters the target nucleus and deposits a fraction of its energy through scattering events with the nucleons that will then scatter with other nucleons. These scattering events cause the prompt ejection of some energetic nucleons and leave the residual compound nucleus in an excited state. The nucleus will then cool itself through various processes in the second stage.

The second stage can be called evaporation. In this stage, the excited nucleus will decay to a lower energy state either through splitting (fission) or through energetic particle emission which can be in the form of multiple gamma rays, nucleons, or alpha particles. If there is sufficient time before breaking up, then the nucleus will equi-

brate. Fragments can form in this equilibrated nucleus and repel each other through the Coulomb interaction leading to IMF products. Once the residual nucleus's energy drops below its binding energy, it will decay via pure gamma emission to a stable or radioactive state, which is the spallation residue.

The secondary products from nuclear reactions which are of most interest from a radiation effects standpoint can then be classified into three categories [60, 62, 63]:

1. **Spallation** - A spallation reaction produces one or more secondary nucleons and/or light ions as the excited nucleus decays leaving a heavy residual fragment from the target nucleus. These heavy fragments have a mass typically greater than or equal to about $2/3$ of the target atom mass for incident protons and neutrons, and often have a comparatively short range and high LET value.
2. **Fission** - Induced fission productions are only common for very heavy nuclei (about $Z > 65$). Fragments have a mass typically about $1/2$ of the target atom mass on average. Because induced fission is an exothermic process, these fission fragments can have a substantial amount of energy and thus a high range compared to spallation products. Because of their high mass, they often will have a high LET value as well.
3. **Intermediate Mass Fragmentation (IMF)** - IMF products are emitted from an equilibrated compound nucleus created by the joining of the incident ion and the target atom. IMF fragments have a mass between about $Z = 3$ and $Z = 20$. IMF production cross section increases with incident particle mass and energy.

A variety of secondary products can be created from inelastic nuclear collisions. Thus it is essential for a nuclear physics model to come as close to reality as possible, particularly for proton- and neutron-induced single event upset simulations.

An accurate nuclear physics model in a SEU simulation tool not only can allow for SEU prediction of a device, but can give insight into the mechanisms of SEUs. In this work, the mechanisms of proton- and neutron-induced SEUs is investigated via experimental techniques and Monte Carlo simulation using the SEU simulation tool, MRED. The following chapter details the experiments performed in this work, and describes how MRED was used.

CHAPTER III

EXPERIMENTAL AND SIMULATION METHODS

This chapter describes the experimental and simulation techniques and devices used in this study. Details are given of a pulsed height analysis system with an integrated time of flight measurement capability, which was constructed as part of this work. A description of the diode structures which were fabricated specifically for this study is also presented. Finally, the Monte Carlo simulation tool and its use in this work is described.

Charge collection measurements

For the experiments performed in this work, the amount of deposited charge collected in a the sensitive volume region of a device due to incident protons and neutrons is measured and histogrammed. This is accomplished through pulse height analysis (PHA). This section describes the principles of pulse height analysis and the 16 channel PHA system which was built for this study to perform the measurements [64].

Pulse height analysis (PHA)

In general, the technique of pulse height analysis (PHA) takes a radiation-induced current pulse from a detector and converts it to a pulse whose amplitude is proportional to the integrated current, which is equal to the total charge collected in the detector. The pulse height can then be stored, and many radiation-induced events

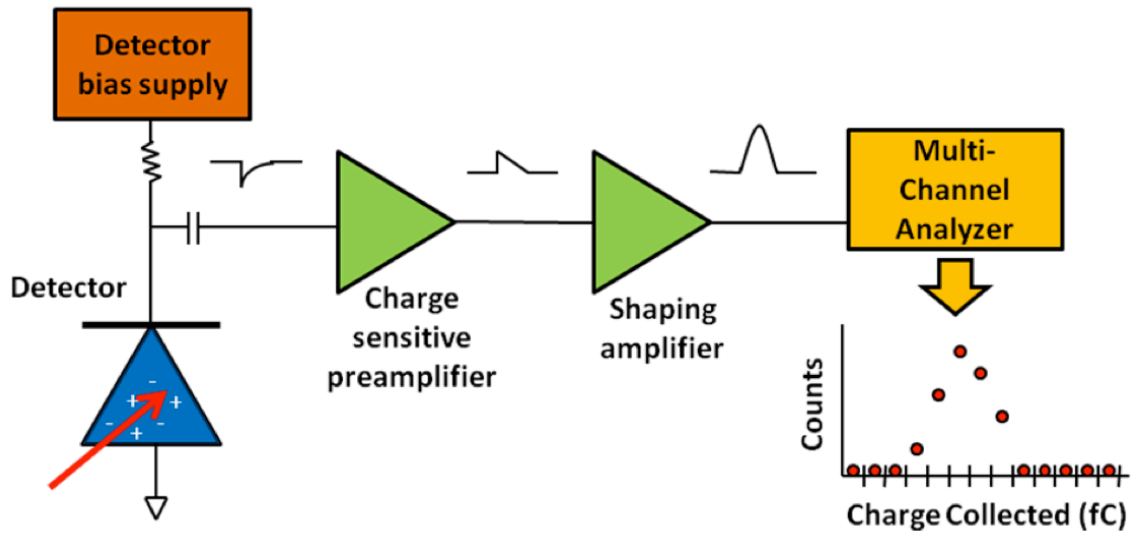


Figure 13 Block diagram of a pulse height analysis system. The red arrow represents ionizing radiation incident on the detector. From [64].

can be collected from the detector and displayed in a histogram. The details of how this is accomplished is shown in the block diagram in Fig. 13. As the figure shows, the radiation-induced current pulse from the detector is passed to a charge sensitive preamplifier which integrates the current over a set time. The connection between the detector and the preamplifier is made as short as possible to reduce resistive losses in the signal. The height of the output pulse from the preamplifier is proportional of the total amount of charge collected. This output pulse is passed to a shaping amplifier which amplifies the pulse, manipulates it into a Gaussian shape, and passes it to a multi-channel analyzer (MCA). The MCA then records the pulse height value, and computer software stores these values in a histogram as depicted in Fig. 13.

Silicon surface barrier detectors (SBDs) are commonly used in conjunction with PHA to characterize the total energy of alpha radiation from radioactive sources. When biased to a specified voltage, the SBD has an active region which is thick enough to completely stop the emitted alpha particles and the charge collected is then

Table 2 Alpha Sources Used for PHA Calibration

Source	Half-life ($t_{1/2}$)	Alpha Energy (MeV)	Comments
Po-210	138 days	5.304 (100%)	Short $t_{1/2}$, single decay product
Am-241	432 years	5.49 (85%), 5.44 (13%)	Long $t_{1/2}$, multiple α energies

proportional to the incident alpha particle's energy. SBDs have a charge collection efficiency of near 100%. The SBD used in this work has an active region that is 500 μm thick, while the range of a 5 MeV alpha particle in silicon is less than 50 μm [65]. Thus, a characterized radioactive source in conjunction with a SBD can be used to calibrate the PHA system so that the histogram channels will correspond to energy deposited/collected by the detector. In this work, either a Polonium (Po-210) or an Americium (Am-241) alpha source was used. Characteristics of each source are listed in Table 2.

An example of an alpha peak histogram as measured with a PHA system is shown in Fig. 14. This figure was measured with a Po-210 source and a 500 μm SBD. A Gaussian is fit to the data to provide an good estimation of the channel corresponding to the alpha peak, and the full width at half maximum (FWHM) of the data. The FWHM is used to estimate the uncertainty in the peak channel. For the measurement shown in Fig. 14, the peak channel is measured as channel 153 ± 8 .

To complete the alpha calibration of a PHA system, the channel associated with a pulse amplitude of zero must be determined. Ideally, a peak with zero amplitude would correspond to channel zero. However, in practice this is almost never the case. In order to determine which channel corresponds to the zero pulse amplitude, a calibrated pulser is used to inject pulses of a known amplitude into the charge sensitive preamplifier. By varying the pulse amplitude, several pulse amplitude vs channel number data points are recorded and plotted. A linear fit to these data is

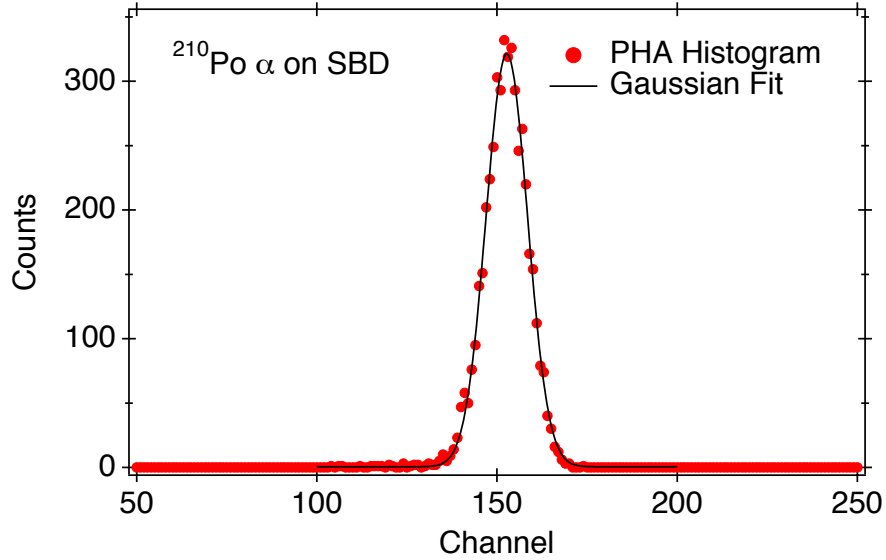


Figure 14 Measured PHA histogram of Po-210 alphas incident on a 500 μm surface barrier detector. The fitted Gaussian was used to determine the channel corresponding to the peak alpha energy.

used to compute the zero amplitude channel.

The location of the alpha peak will vary with the amplifier setting in the PHA system. Also, the number of channels used in the PHA analysis can be changed for different experiments. Additionally, factors such as cable length and background noise can significantly effect the response of a PHA system. For these reasons, the alpha calibrations of the PHA system in this work were done at the cyclotron facility to reduce errors. During the calibrations, the alpha sources were placed on the SBD in air, and were not under vacuum. Therefore the amount energy lost by the alpha particles while traversing the air gap before reaching the SBD surface must be taken into account. SRIM [65] was used to calculate the energy lost in the air gap. For the Po-210 source, the air gap was measured to be 3 ± 0.2 mm. For a 5.304 MeV alpha particle in air, SRIM reports the energy loss to be 0.097 MeV/mm. Thus the peak energy of the alpha particles reaching the SBD is 5.013 ± 0.036 MeV. The uncertainty in the energy loss is assumed to be small, and the propagated uncertainty is due to

the uncertainty in the air gap measurement. Note that the air gap not only increases the uncertainty in the alpha energy, but also causes the alpha energy peak to broaden due to straggling [65].

Once the alpha peak and the zero amplitude channels are known, the conversion from channel number to energy deposited can be calculated for the PHA system. This is done simply by determining the linear relationship between channel number and energy, using the two data points. For example, suppose the zero channel was found to be channel 7, and the channel for the 5.013 ± 0.036 MeV alpha particles was found to be 153 ± 8 , as shown in Fig. 14. The slope of the line determined by these two data points would be: $(5.013 - 0)/(153 - 7) = 0.03434 \pm 1.81 \times 10^{-3}$ MeV/channel. The uncertainty associated with the energy calibration is greater for higher channel numbers. For example, channel 2000 in this example would correspond to 68.7 ± 3.6 MeV. It is important to take these uncertainties into account when evaluating the data taken by a PHA system which has used the described method for energy calibration.

Energy deposited in silicon generates charge with a conversion factor of 0.0225 MeV/fC [33]. The charge collection region of modern semiconducting devices is most often composed of doped silicon. Thus this factor is commonly used to convert between deposited energy and charge collected. It is used in this study to convert energy in the PHA energy calibration to collected charge.

In this work, all of the PHA data are analyzed in integral cross section form. This is illustrated in Fig. 15. To generate the integral cross section curve, the raw PHA data are converted to counts vs collected charge through an alpha calibration, rendering the plot on the left of the figure. This histogram is then integrated, generating the plot on the right using

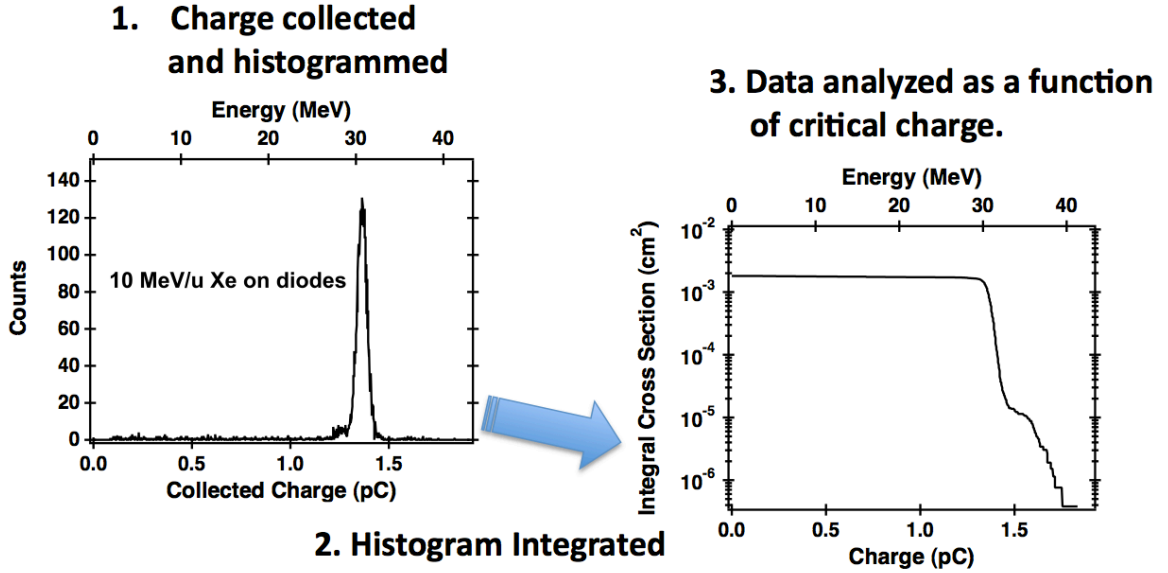


Figure 15 Illustration of how the PHA data are analyzed by creating an integral cross section curve.

$$\sigma(Q) = \sum_{i=i(Q)}^{\infty} \frac{N_i}{f}, \quad (2)$$

where σ is the integral cross section, Q is charge, N_i is the counts in bin i , and f is the particle fluence in cm^{-2} . The advantage of plotting the data in this way is that the single event upset cross section of a particular device can be read directly off the plot by knowing the critical charge of the device. Alternatively, if the device doesn't have a critical charge, the cross section for collecting at least a given amount of charge in a device can be interpreted easily from the figure. This is the preferred way of plotting simulation and charge collection PHA data when performing radiation effects research.

16 channel PHA system

In order to allow for parallel data collection with multiple devices, a 16 channel PHA system was designed and built, in part, for this work. This system has the capability of performing simultaneous charge collection measurements on up to 16 devices, although for reasons stated below, only 8 devices were tested in parallel in this study. This parallel data acquisition not only allowed for simultaneous irradiation of different devices, but also redundant devices for added confidence in the measurements. This 16 channel PHA system was used for all of the experimental data reported in this work. Some details of this PHA system are also given in [64], but are listed here as well for the reader.

A block diagram of the 16 channel PHA system used is shown in Fig. 16. In this 16 channel PHA system, a Mesytec MPRS-16 preamplifier/shaping amplifier is used in conjunction with the Phillips Scientific 7164H peak sensing analog-to-digital converter (ADC). The 7164H is a module following the Computer Automated Measurement And Control (CAMAC) standard, so a CAMAC crate controller is needed to interface with it. A Kinetic Systems 3988 General Purpose Interface Bus (GPIB) crate controller was used to interface a computer with the CAMAC crate modules. In order to prevent the long latency of the GPIB standard from reducing the PHA systems bandwidth, a Hytec 1342 auxiliary crate controller was used in List Mode. The 1342 stored the PHA events in a buffer, which was periodically read out by the 3988. The software used to interface and control the CAMAC modules was written by Marcus Mendenhall using the Python Laboratory Operations Toolkit. This software saves every digitization event from each of the 16 channels along with a timestamp, which was useful for post processing of the data.

A discriminator board was designed and built as a custom printed circuit board

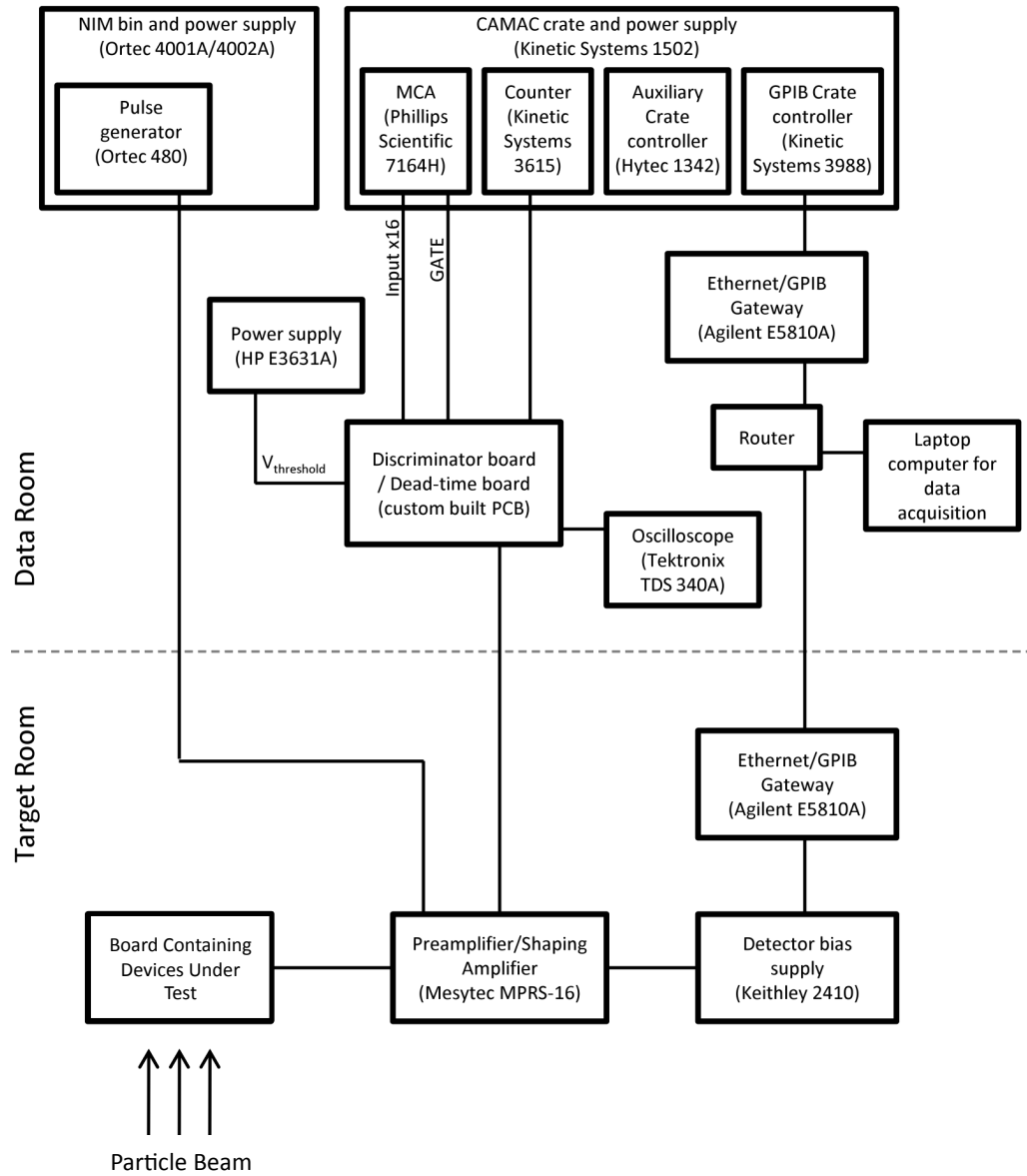


Figure 16 Block diagram of the 16 channel PHA system used for the experimental part of this work. From [64].

(PCB). The discriminator board detects when a shaped pulse from any of the channels in the MPRS-16 exceeds an adjustable threshold voltage, and then triggers the 7164H to digitize the pulse on each channel. The detailed design of the discriminator board is given in [64]. Note that, once triggered, the 7164H digitizes the signals present at that moment on all 16 inputs. This increases the dead time of the PHA system. However, it also allows for the identification of anomalous events that are manifest as large-amplitude charge collection events affecting multiple channels at the same time. These events were identified as being caused by noise spikes on the detector bias supply power line (see Fig. 13). These events were easily identified and removed from the pulse height spectra through post processing of the data. The dead time of the system was measured by sampling the BUSY signal of the 7164H at 10 MHz. The fraction of the time that BUSY was asserted was defined as the dead time, and was determined using a Kinetic Systems 3615 Counter.

Because of the variability in the response between channels, it is necessary to perform an energy calibration on each channel on site before device irradiation using the alpha calibration technique described in the previous section. For the energy calibration, the SBD was connected to the PCB which held the devices under test, and biased using the Keithley 2410 power supply shown in Fig. 16. This PCB will be described in the following section.

Diode Structures

In order to determine experimentally the effect that high-Z materials, like tungsten (W), can have on proton- and neutron-induced charge collection, custom-made diodes were fabricated for this study. Sandia National Laboratories fabricated the vertical n+/p diodes shown in Fig. 17. This figure shows the two diode overlayer configurations that were fabricated. One configuration has AlCu overlayers and layers with

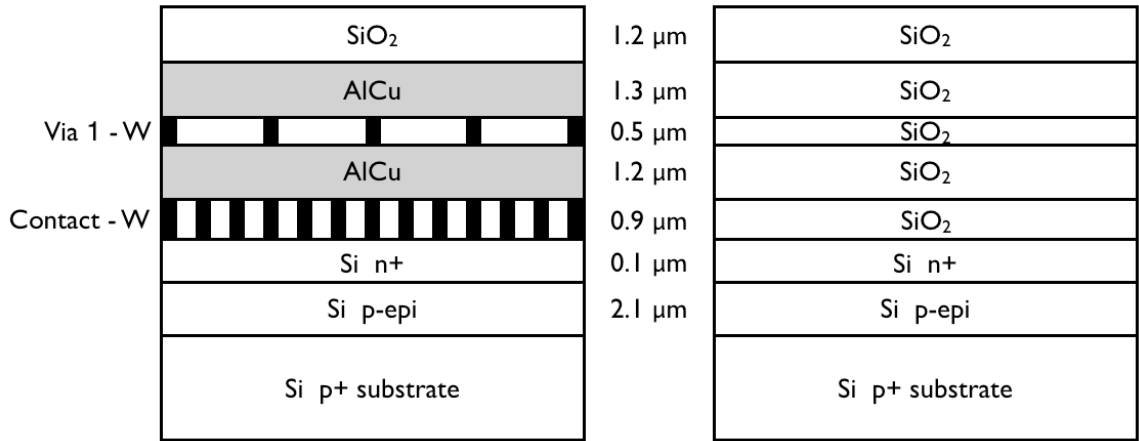


Figure 17 Overlayer configuration diagrams of the two types of bulk silicon diodes used in this study. One diode has W overlayers while the other does not. Published in [14].

W (with SiO₂ between the W), while the other has only SiO₂ overlayers. The AlCu layers consist of 99.5% Al and 0.5% Cu. The total thickness of material covering the diodes is the same in both cases. For the first diode configuration, there is W present in two layers. On the layer labeled Via 1, the W plugs are spaced evenly to provide 5% coverage of the diodes surface. On the Contact layer, the W is laid out in strips spanning the length of the diode to provide 43% coverage. The AlCu overlayers have 100% coverage, but only contain 0.5% Cu, and thus it is not expected that they will contribute significantly to charge collection any more than similarly placed SiO₂ layers because the atomic number of Al is close to that of Si.

The lateral dimensions of the diodes are 300 μm × 780 μm (see Fig 18). The thickness of the sensitive volume in the diodes was determined experimentally by irradiating the diodes with heavy ions at the Lawrence Berkeley National Laboratory (LBNL) cyclotron facility. The diodes were reverse biased with 5 V, and the charge collected from the ion irradiation was measured. The sensitive volume thickness was then calculated to be 2.1 μm using the known LET of the ion. The same result was obtained when repeating the test using ions of different LETs.

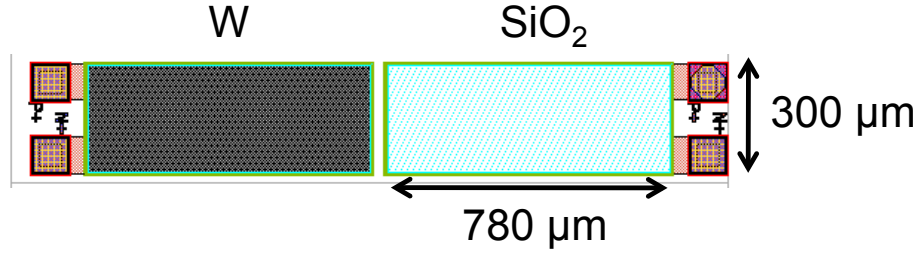


Figure 18 A top-down view of a pair of diodes with the two overlayer configurations as they were fabricated.

Initial Monte Carlo simulations using the dimensions shown in Fig. 17 for the sensitive volume region revealed that the placement of the sensitive volume region with respect to the W overlayers significantly affected the calculated charge deposition. For this reason, doping profile measurements were made on the diodes via destructive analysis and 2-D technology computer-aided design (TCAD) simulations were performed to better understand the location and dimensions of the charge collection region. The simulated diode structure replicated the doping profiles and geometries of the n+, p-epi and p+ substrate regions of the diodes. Heavy ion strikes emulating the linear energy transfer (LET) of those used in the LBNL experiments were used to strike the n+ region of the diode. Current transients were measured at the n+ region contacts, which were then integrated over the duration of the simulation to get the total collected charge for a given ion strike. Device physics models activated in the simulations were: Poisson and Fermi-Dirac statistics, Shockley-Reed-Hall and Auger recombination, and dopant-dependent mobility models. All simulations were carried out at room temperature settings. The TCAD simulations were done by Vishwa Ramachandran.

The TCAD simulations showed that, under a 5 V bias, the depletion region only extends 1.2 μm into the epitaxial layer, however, charge deposited throughout the 2.1 μm thick layer is collected. This type of charge collection from an epitaxial layer

is consistent with [66]. TCAD simulations that stopped the incident ion at the top edge of the p-epi region shown in Fig. 17 revealed that charge collection from the n+ region is negligible. Therefore, for the Monte Carlo simulations performed in this work, the 2.1 μm thick sensitive volumes of the diodes are placed directly below the n+ silicon region.

These test structures are unique in that they allow for isolating the influence of W overlayers on charge collection, and also provide structures with a well-defined sensitive volume region for Monte Carlo simulation comparison. The diodes relatively large cross sectional area allows for more frequent detection of the proton- or neutron-induced nuclear reaction events, and thus provides better statistics over short exposure times. Also, the inclusion of larger-than-typical amounts of W in the diode overlayers was intentional in order to make their role in charge collection more observable than they would be in a typical device.

The diodes were fabricated in pairs with the two diode overlayer configurations adjacent to each other as shown in Fig. 18. The diode pairs were mounted and bonded out in 40 pin dual in-line packages (DIPs), with each DIP containing two pairs of diodes. Only four diodes were mounted in each DIP due to the size of the diodes. Custom PCBs which were designed to be integrated into the 16 channel PHA system were used to mount the diodes in the beamline for the experiments. These PCBs were designed to connect 8 channels to each of the 40 pin DIP sockets. Since only four diodes were mounted in each DIP, only 8 out of the 16 channels were utilized at a given time for the charge collection experiments.

After being exposed a high particle fluence ($\sim 3 \times 10^{13} \text{ cm}^{-2}$), the diodes showed signs of displacement damage, and were not suitable for reliable charge collection. For this reason, the diodes were monitored for displacement damage and replaced when they were no longer usable. Also, fresh set of diodes were used for each experiment.

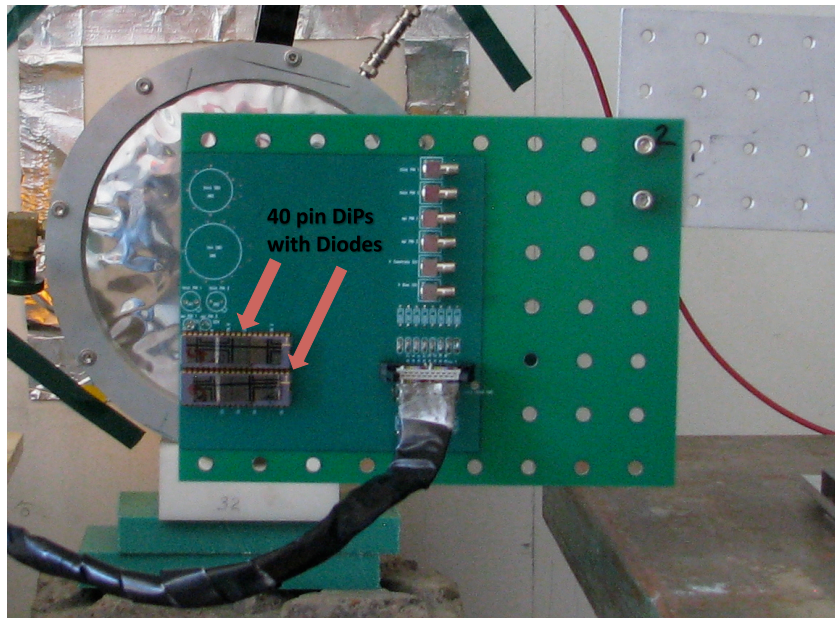


Figure 19 Picture of the PCB holding the 40 pin DIPs which housed the diodes in this study. The connector on the right connects the 16 channels in the PCB to the MPRS-16 preamplifier.

Charge collection experiments were performed with these diodes at different cyclotron facilities with both proton and neutron beams. The details behind the experiments performed at these facilities is discussed in the following section.

Particle Beam Experiments

Proton Irradiations

Proton irradiations were performed on the diodes at the TRIUMF proton irradiation facility and the Indiana University Cyclotron Facility (IUCF). In both cases, the proton energies were high enough (and thus the LET values were low enough) that the contribution of direct ionization by the protons to the overall charge collected is negligible. Thus all of the charge collection events were due to nuclear reaction events

between a proton and a nucleus from the material in or surrounding the sensitive volume. Because the cross section for proton-induced nuclear reactions is small, the devices were exposed to a minimum fluence of $5 \times 10^{12} \text{ cm}^{-2}$ for each run in order to obtain statistically significant data.

Irradiations were performed at TRIUMF using the 500 MeV beamline. Irradiations were performed at TRIUMF at 0° (normal incidence), 180° (backside) and $\sim 85^\circ$ (grazing). The IUCF irradiations were all performed at normal incidence. Several proton energies were used at IUCF. The highest proton energy available is 198 MeV. Lower proton energy can be obtained by inserting copper degraders between the end of the beamline and the diodes. However, this does increase the FWHM of the energy peak due to straggling. In this work, proton energies of 198, 90, 55 and 27 MeV were used. Due to the similarity of the charge collection curves for 90, 55 and 27 MeV energies, only the results from the 90 MeV protons is presented in this document. The FWHM of the 198 and 90 MeV proton energy peaks are 1.2 and 2.5 MeV respectively.

Neutron Irradiations

Neutron irradiations were performed on the diodes at the Weapons Neutron Research (WNR) facility at Los Alamos National Laboratory using the Target 4 Flight Path 15L (T4FP15L). This flight path is different from the ICE House (Irradiation of Chips and Electronics), flight path 30L, which is commonly used to simulate the terrestrial neutron environment for radiation effects research. However, the neutron energy spectrum of this flight path is similar, with a slightly higher flux of the higher energy neutrons (see Fig. 20). In many radiation effects publications, the ICE House neutron spectrum is referred to as the WNR neutron spectrum, so this nomenclature is used here as well.

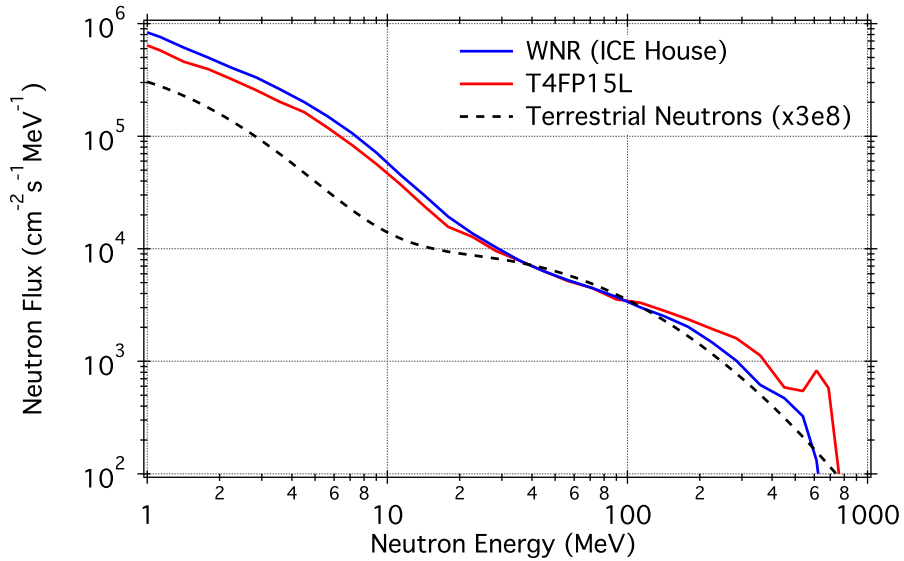


Figure 20 Measured values for the neutron energy spectra of the WNR and T4FP15L neutrons. The JEDEC terrestrial neutron spectrum is also shown for comparison.

Like the WNR neutrons, the T4FP15L neutron spectrum is similar to the terrestrial neutron energy spectrum, but with a flux over eight orders of magnitude greater. Both of these neutron beams are generated in the same way: high-energy protons are accelerated and collided into a tungsten metal target. The secondary neutrons created from the proton-tungsten collision are emitted at a wide spectrum of energies and angles. The WNR neutrons are collected at a 30° horizontal angle, with respect to the incident proton beam, while the T4FP15L beam line is collected at 15° . The neutron energies in these flight paths extend up to nearly 800 MeV, which is the energy of the protons used to create the spectrum. Because of the small cross section for neutron-induced nuclear reactions and the relatively low flux of high energy neutrons in the spectrum, the devices were irradiated to a high fluence of $\sim 3 \times 10^{12} \text{ cm}^{-2}$ at both normal incidence and at a grazing angle.

Like the experiments using proton irradiation, all of the charge collection events recorded were due to neutron-nuclei collisions. Beyond simply measuring the charge

collected due to irradiation by a wide range of neutron energies, insight into the charge collection mechanism was obtained by correlating a charge collection event with the incident neutron energy which caused the event. This was accomplished with time of flight measurements. The following section discusses the time of flight measurements performed in this work with the neutrons in the T4FP15L beam line.

Time of Flight (TOF) Measurements

For the neutron irradiations done at the WNR facility, a time of flight (TOF) measurement capability was integrated into the 16 channel PHA system. The facility at WNR provided a pulse signaling the collision of the proton beam with the tungsten target, generating the neutron beam. This allowed the time between the neutron generation and a charge collection event to be measured. Using the measured TOF, the neutron energy is calculated for the neutron whose nuclear collision caused the measured charge collection in the diode structure. So for each charge collection event, a corresponding neutron energy is recorded. This section discusses the experimental details of the TOF setup, the energy calculation, and the limitations in the TOF measurements.

Description of TOF setup

Because only 4 diodes were bonded out into each DIP as described in Section III, only 8 of the 16 available channels were used for charge collection measurements. The TOF measurements were then made by passing the signal from an Ortec 566 time-to-amplitude converter (TAC) to an unused channel in the PHA system. The output from the TAC was connected directly to one of the channels in the discriminator board (see Fig. 16), with the trigger disabled on that channel. So for every charge collection event exceeding a given threshold, the MCA would also record a

corresponding pulse height from the TAC, but pulses from the TAC would never trigger the MCA. The start pulse for the TAC is provided by the facility signaling the time of the neutron generation. The stop pulse for the TAC was retrieved from the NIM output of the Mesytec MPRS-16 preamplifier/shaping amplifier used for the charge collection measurement. The amplitude of the pulse from the TAC is then proportional to the time between neutron generation and the charge collection event.

The TAC was calibrated by connecting a pulser to the start input, while the same signal was sent to the stop input through a cable of known delay time. The original time window for pulse measurement on the discriminator board was 1.5 μs , while the TAC's full range of time measurement was 2 μs . In order to measure the full range of time pulses from the TAC, the capacitor on the discriminator board's timer was changed to extend the time window for pulse measurement to 6 μs . Because the charge collection events from the neutron beam were observed every 5-10 seconds, this extended time window didn't cause any deadtime or pileup problems. The calibrated TAC had a measured bin width of 0.62 ns/channel.

Because neutrons cause charge deposition through secondary particles from nuclear collisions, the TOF measured includes the time after a neutron-nucleus collision, the emission of secondary particles, and the collection of charge deposited by one or more secondary particle. The time scale of these events is estimated to be less than a nanosecond, and thus the effect that these events have in delaying the second time signal is considered negligible.

TOF Calculation

The setup described above is capable of measuring the time between the creation of each neutron and the charge collection event. For the analysis of these data, it is necessary to relate that time of flight with a particle energy with a TOF equation.

The calculation of the TOF equation for a non-relativistic particle is straightforward. By inserting $v = d/t$, where v is velocity, d is distance traveled and t is time, into the non-relativistic equation for kinetic energy one gets:

$$E = \frac{1}{2}mv^2 = \frac{md^2}{2t^2} \quad (3)$$

where E is kinetic energy, and m is the particle mass. However, for particles with energy greater than about 10 MeV, the relationship between kinetic energy and TOF needs to take relativistic effects into account. For relativistic particles, the total particle energy, E_T is given by

$$E_T = \gamma mc^2, \quad (4)$$

where c is the speed of light, and γ is given by

$$\gamma = \left(1 - \frac{v^2}{c^2}\right)^{-1/2}.$$

Because a particle is usually characterized by its kinetic energy, E , the total particle energy, E_T , can be replaced with $E + mc^2$. Also the velocity can be replaced with the time and distance as measured in the lab reference frame. Making these substitutions, and rearranging terms, Eq. 4 becomes

$$E = \left(\left(1 - \frac{d^2}{c^2 t^2}\right)^{-1/2} - 1 \right) mc^2 \quad (5)$$

Eq. 5 is used to calculate the kinetic energy of each particle according to their time of flight. Fig. 21 shows the calculated particle kinetic energy vs TOF for neutrons

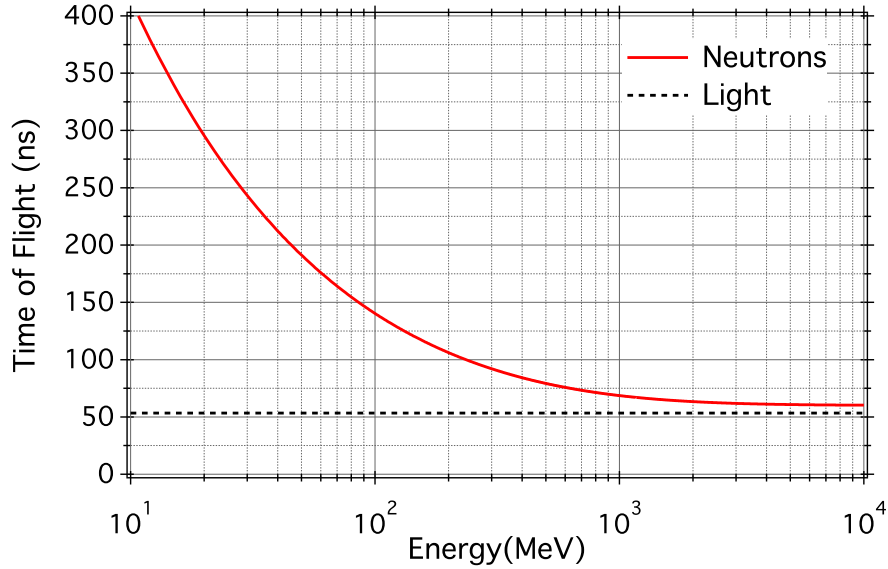


Figure 21 Calculated time of flight vs neutron energy using Eq. 5 for a distance of 18 m. The dashed dotted line shows the time for light to travel the same distance.

using Eq. 5 and the following values: $c = 0.2998$ m/ns, $mc^2 = 939.6$ MeV, $d = 18$ m. The neutron flight distance for the T4FP15L beam line is 18 m.

Fig. 21 shows that the time of flight doesn't scale linearly with particle energy and particles with higher energy will have TOF values closer together. The binning in the MCA, however, is linear, and thus the time bin widths are also linear. For high particle energy, small steps in time result in large steps in energy. So as particle energy increases, so does the relative bin width in energy. Since the bin width for the pulses from the TAC are 0.62 ns/channel, this means that there are only 5 channels for energies between 650 MeV and 800 MeV, while there are about 1400 channels representing energies between 1 and 10 MeV. This is a cause for an increase in uncertainty for high energy neutron measurements. The uncertainty in TOF, and thus energy, is cumbersome to represent when plotting, and thus isn't represented on the plots. However, it is important to bear in mind when interpreting the TOF data.

Monte Carlo Simulations

This section includes a description of the Monte Carlo simulation tool used, as well as how it was used in this work. A description of the simulations run as a part of this work is also described. Finally, a list of the available nuclear physics models for the simulations is given.

Description of Simulation Tool

Various Monte Carlo transport codes exist and are used by different research groups in radiation effect research. At Vanderbilt University, a Geant4-based [67] simulation tool called MRED (Monte Carlo Radiative Energy Deposition) has been developed for SEE computer simulations. MRED uses a comprehensive set of physics models from Geant4 for the transport of radiation through matter, and associated energy deposition. Geant4 is a library of c++ classes that was created and is maintained by a large international collaboration [67].

MRED is unique in that it extends basic Geant4 capabilities to include additional nuclear physics models not available in Geant4, novel cross section biasing techniques for variance reduction [68], and several other useful tools pertinent to SEE prediction [43]. In MRED, the nuclear physics model desired can be selected at runtime so that a comparison of the nuclear physics codes is possible while using the same particle transport and energy deposition routines. Interfacing with MRED is done via Python scripts.

Monte Carlo simulations are invaluable in radiation effects research due to their potential of realistically simulating the space environment, the device structure, and the physics of electronic and nuclear interactions between radiated particles and matter. To this end, great importance is placed on the correctness of the computational

physics used in these simulations, and also on understanding their limitations.

Uses of Simulation Tool

MRED can be used in two different modes for different purposes. These are referred to in this document as “standard mode” and “single event mode”. In the either mode, MRED is used to simulate the irradiation of a defined 3D structure with one or more sensitive volumes. The user specifies radiation type, energy and angle of incidence and location on the structure. The particle can be simulated from all angles, where then the angle is chosen randomly for each particle. The incident particles are transported, one at a time, through the 3D structure and tracked, as are any secondary particle that are generated, and the calculated energy that is deposited in each sensitive volume (SV) is recorded.

In standard mode, the user specifies how many incident particles are desired and energy deposited in the SV is recorded in a weighted histogram. This weighted histogram takes factors such as cross section biasing and geometry into consideration for easy conversion from a weighted histogram to a cross section curve. For each run, MRED reports a “fluence_unit” variable which is used in place of fluence in Eq. 2 to create an integral cross section curve.

An example Python script that uses MRED in standard mode is given in Appendix B. This code runs in MRED version 9.2.0. This example script was used in this work to simulate proton radiation incident on the pair of diodes described in section III. The incident protons are randomized over the surface of the diodes at the specified angle of incidence, simulating the proton beamlines at TRIUMF and IU.

In single event mode, the user has access to all of the information about the incident particle’s track, as well as any secondary particles which are created. Single event mode can be used for various purposes. In this work it was used for replaying an

event by giving MRED the known random seeds, checking events for a nuclear collision to gain information about secondary particles, and generating custom histograms to save multiple cell upset (MCU) information.

An example Python script that uses MRED in single event mode is given in Appendix C. This code also runs in MRED version 9.2.0. This script defines a 32×32 bit array of nested SVs to simulate an SRAM. The nested SV size, charge collection efficiency and spacing were calibrated to simulate a 4 Mbit Texas Instruments SRAM fabricated in a commercial 65 nm Bulk CMOS process. The SV information was provided by Brian Sierawski. The script runs MRED in single event mode and for each particle strike, it saves the amount of charge that was deposited in each SV, along with the weight and random seeds for that event. The data was post-processed to obtain SEU and MCU cross sections for the device when irradiated by different neutron energy spectra. The script was also used to replay events of interest for this work.

Nuclear Physics Models

As stated above, MRED allows the user to choose from various available physics models at runtime. There is a different set of physics models used for simulations done for hadrons and for heavy ions. In this work, only the hadronic nuclear physics models are considered since all of the simulations were done with protons or neutrons. Because the conclusions drawn from the simulations rely heavily on the nuclear physics model used, a validation was done using the experimental data collected in this work, as well as nuclear physics experiments not discussed in this document (see [69, 70]). These validations are done in addition to the many validations and checks that are performed by the authors of each physics model [67, 71–73]. Table 3 shows a list of the available physics models in MRED.

Table 3 Hadronic Nuclear Physics Models in MRED

Model	Source
Bertini Cascade	Geant4 version 9.3 [67]
Binary Cascade	Geant4 version 9.3 [67]
G4 Quantum Molecular Dynamics (G4QMD)	Geant4 version 9.3 [67]
Cascade-Exciton Model (CEM)	Los Alamos code CEM03 [71]
JAERI Quantum Molecular Dynamics (JQMD)	PHITS version 2.1.4 [72]

CHAPTER IV

MECHANISMS OF PROTON-INDUCED SINGLE EVENT EFFECTS

Introduction

Due to the proton-rich environment in space, proton-induced SEUs continue to be an area of interest to the radiation effects community. As was mentioned previously, most of the energetic protons found in space do not have a high enough linear energy transfer (LET) to cause SEUs through direct ionization. Instead, proton-induced SEUs are typically caused by secondary particles that result from proton-nucleus collisions in materials in or near a sensitive volume. While this is well-understood, it is not understood what effect that high atomic number (high-Z) materials found in devices, such as tungsten (W), can have on proton-induced SEUs.

Howe *et al.* [5] showed Monte Carlo calculations that predicted that, when irradiated with protons, devices containing W overlayers would have the same SEU response as devices with similarly placed oxide layers (See Fig. 22). An increase in the SEU response was only seen for the device with a W overlayer, when the incident particle was a heavy ion. The authors concluded that there is a limited energy and momentum transfer possible by protons compared to heavier ions, and that the presence of W would have no foreseeable effect on proton-induced SEUs.

Conversely, Schwank *et al.* observed proton-induced single event latchup (SEL) in SRAMs whose SEL LET thresholds were greater than the maximum LET of a silicon recoil atom ($\sim 13 \text{ MeV}\cdot\text{cm}^2/\text{mg}$) [6]. Through simulations, they concluded

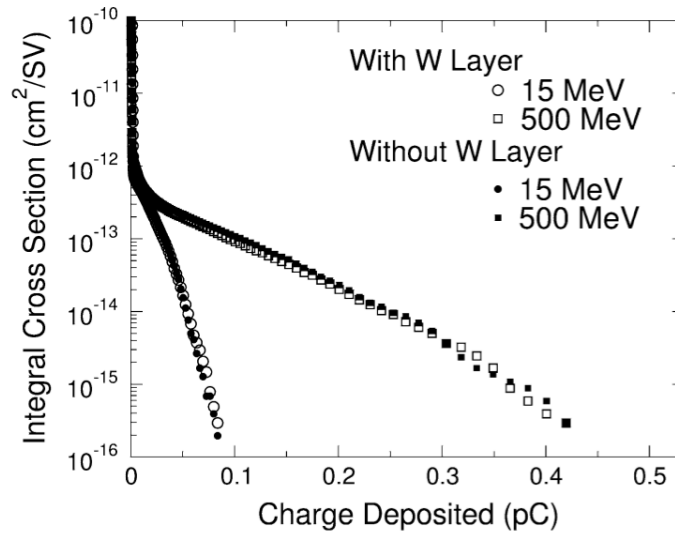


Figure 22 Figure from Howe *et al.* [5] showing no increase in proton-induced charge collection for devices with a W and an oxide overlayer.

that these SEL events were likely caused by higher-LET secondary particles from proton collisions with high-Z materials in the SRAMs. However there was no experimental verification of this conclusion, nor was any analysis of how these higher-LET secondary particles could effect proton-induced SEUs.

In this chapter, experimental observations of the dependence of the charge collection cross section on proton energy and angle of incidence for devices with and without a W overlayer are presented. These data are used to infer the role of high-Z materials near the sensitive volume on proton-induced SEUs for a given Q_{crit} . The charge collection data are compared with computer simulations using various available nuclear physics codes that have been integrated into the Monte Carlo Radiative Energy Deposition tool (MRED) developed at Vanderbilt University [43], and this comparison is used to validate a nuclear physics model. Using this validated model in MRED, the particle species and angular distribution of secondary particles from proton-nucleus collisions is investigated.

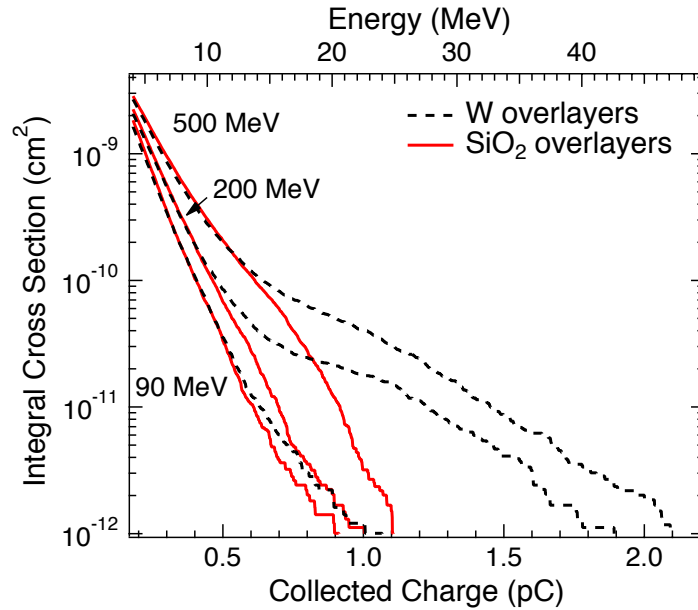


Figure 23 Measured integral charge collection cross sections for both diode configurations with normally incident 90, 200, and 500 MeV protons. Published in [14].

Charge Collection Measurements

The results of normally incident 90, 200 and 500 MeV proton irradiations on the diode structures discussed in section III are shown in integral cross section form in Fig. 23. The integral cross section is proportional to the probability that the collected charge exceeds the charge value shown on the x-axis. Displaying the data in this form is useful because it allows the charge collection cross section to be read directly from the curve for a given amount of minimum charge collected, Q_{\min} . That is, it is the cross section for collecting at least that given amount of charge. In this way, the dependence of the charge collection cross section on proton energy and angle can be analyzed as a function of minimum charge collected. This charge collection cross section is analogous to the SEU cross section of a device with the same sensitive volume dimensions. The SEU cross section could then be read from the cross section

plots for a given critical charge. It is important to note that the quantitative SEU cross section found in this way is only accurate for devices with a sensitive volume geometry equal to that of the diodes used in this experiment. However, a qualitative understanding of the proton-induced SEU cross section can be obtained with these data.

As is seen in Fig. 23, the charge collection cross section increases with proton energy for the diodes with SiO₂ overlayers for any Q_{\min} . This is possibly due to an increased energy (and thus range) of the high-LET secondary particles. Fig. 23 also shows that, for 200 and 500 MeV protons, the presence of W near the sensitive volume region of a device causes a significant increase in the cross section for charge collection events above ~ 0.5 pC. This effect is even more pronounced for higher charge.

Fig. 23 shows that the impact of the W overlayer strongly depends on the energy of the incident proton. While the data for the different diode configurations diverge at cross sections below about 10^{-10} cm² for 200 and 500 MeV protons, a similar divergence is not seen for the 90 MeV protons until about 10^{-11} cm², and the difference between the two curves after the divergence is minor. Schwank *et al.* [6] showed through computer simulation that a probable cause for high-LET secondaries from a proton-W collision is proton-induced fission. Fig. 23 is consistent with that hypothesis since the experimental proton-induced fission cross section for W reported in [62] is < 1 mb for proton energies below 100 MeV and increases rapidly to ~ 4 mb at 200 MeV and ~ 10 mb at 500 MeV (see Fig. 24).

There is a significant difference between secondary particles that originate from proton-induced fission and those that originate from proton-induced spallation. Proton-induced spallation fragments consist of one or more energetic nucleons and/or light ion fragments, which typically have a long range and a low LET, and an energetic residual nucleus, which typically has a high mass number (and thus high LET) but

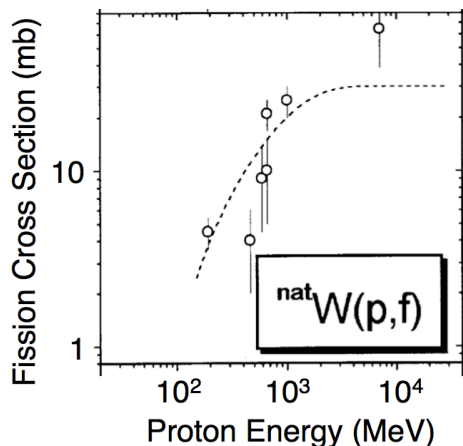


Figure 24 Experimental measurements of proton-induced fission in $^{\text{nat}}\text{W}$, compiled by Prokofiev [62].

a relatively short range. Proton-induced fission produces two energetic fragments that each typically has a mass number roughly equal to half the parent nucleus mass number. These fission fragments have a much higher energy, and thus a longer range, than a high-LET spallation fragment and can thus deposit more charge in the large sensitive volumes of the diodes used in this study. It is important to note that proton-induced fission is not possible in silicon, but is only seen in high- Z materials, such as W . Monte Carlo simulations confirm that proton-induced fission fragments from W , and not simply proton-induced spallation fragments, are the cause of the increased charge collection cross section seen in Fig. 23 (See section IV).

Fig. 23 shows that the dependence of the charge collection cross section on proton energy varies with Q_{min} . For low charge collection events 0.2 pC, the charge collection cross section measured with 500 MeV protons is only about 30% larger than with 200 MeV protons. However, for higher Q_{min} , the charge collection cross section measured with 500 MeV protons could be as much as an order of magnitude larger than that measured with 200 MeV protons. This means that the SEU cross section for SEU hardened devices with a high Q_{crit} would depend more on the incident proton energy than devices with a low Q_{crit} . In addition, the effect that the presence of W

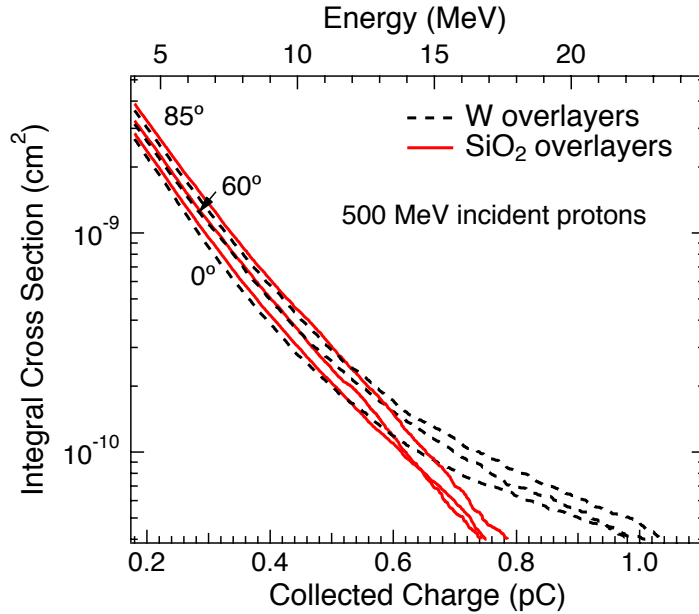


Figure 25 Measured integral charge collection cross sections for both diode configurations tested with 500 MeV protons at 0° , 60° and 85° . Published in [14].

near the sensitive volume of a device has on the SEU cross section varies with Q_{crit} . For low Q_{crit} devices, W near a sensitive volume would have little to no effect on the SEU cross section to protons. For high Q_{crit} devices, however, the presence of W could cause a significant increase in the SEU cross section and even cause upsets in devices that would otherwise be considered SEU immune to protons.

Charge collection data obtained by irradiating the diodes at different angles with 500 MeV protons are shown in Fig. 25. The charge collection cross section here is seen to increase only slightly as the angle of incidence is varied from 0° (normal incidence) to 85° (grazing) for both diodes. Because of the thin charge collection region in these diodes, one might expect a significant increase in the charge collection cross section at grazing angles. If the high-LET secondary particles from 500 MeV proton-nucleus collisions are forward directed, these particles would have a longer path length through the charge collection region than they would at normal incidence, and thus deposit

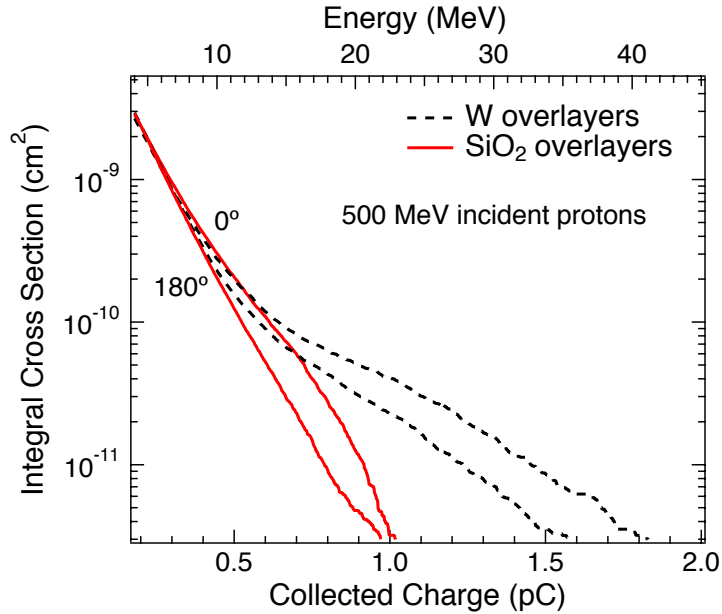


Figure 26 Measured integral cross section plots for collected charge from 500 MeV incident protons on the diode test structures. The normally incident curve and backside (180°) incidence are compared. Published in [14].

more charge. However, Fig. 25 is consistent with data reported in [74]. The devices used in [74] were similar to the diodes in Fig. 17 in that they also had thin sensitive volumes. That is, their vertical dimension was over an order of magnitude smaller than their horizontal dimensions. For these devices, the proton-induced SEU cross section was shown to increase at incident grazing angles for 63 MeV protons, but not for 200 MeV protons. As we will show in section IV, the direction of high-LET secondary particles from proton-silicon collisions is dependent on the incident proton energy. It is probable that a significant increase in charge collection cross section would be observed for the diodes if irradiated on angle at lower proton energies.

In addition to the three angles shown in Fig. 25, the diodes were irradiated from the backside at 500 MeV. Fig. 26 shows the comparison between frontside and the backside measurement. There is an unexpected discrepancy between the two curves for diode with SiO_2 overlayers. The protons incident on the backside do pass through

a few millimeters of packaging and substrate materials, however the LET (in Si) of 500 MeV protons is $\approx 2 \times 10^{-3}$ MeV·cm²/mg, so the protons would only lose a few MeV of energy by passing through the backside materials. Since protons incident at both angles would react with silicon nuclei to produce high-LET secondary particles, one would expect a similar cross section curve. A possible cause of the discrepancy would be unforeseen materials present near the diode. The secondary products from proton interactions with these materials would likely be ranged out in the silicon substrate, and thus be absent in the backside measurement, but would contribute to the charge collection in the normally incident protons. This would account for the larger cross section curve for the normally incident protons.

Fig. 26 also shows comparable charge collection measurements for the diodes with W overlayers for both frontside and backside irradiations, even though W was only present above the sensitive volume. This shows that the proton-induced fission reaction products are relatively isotropic in their direction of emission, as confirmed by computer simulations in the following section. Simulations also show that proton-induced spallation fragments tend to be forward directed, and thus aren't the major cause of the high charge collection events.

Monte Carlo Simulations

Model Validation

In addition to providing insight into the role of overlayer metallization on charge deposition in devices exposed to protons, the data from section IV also allow for validation of SEE modeling tools for proton effects. The well-defined layers and sensitive volumes of the diodes lend themselves to straightforward modeling. For the computer simulations performed in this study, the MRED tool developed at Vanderbilt Univer-

sity [43] was used. The physics models used for validation against experimental data in Fig. 27 are given in Table 3.

Simulations of protons normally incident on both diode configurations were run with the hadronic models listed above for 90, 200, and 500 MeV protons. Fig. 27 shows these simulation results along with the experimental data. The experimental data are represented by a band due to the uncertainty in the energy calibration of the measurements. This error was not represented in Figs. 23-26 because each of those data sets had the same calibration error so the data are still comparable to one another without taking this calibration uncertainty into consideration. All of the models except the Bertini Cascade show good agreement for the SiO₂ overlayer diode configurations for 90 and 200 MeV protons, and that the JQMD/PHITS model significantly overpredicts the data at 500 MeV particularly for the W overlayer configuration. An important observation from Fig. 27 is that the Bertini Cascade shows almost no difference in its predictions for the two different diode configurations at any proton energy. Note that it was the Bertini Cascade model that Howe *et al.* [5] used in their study which also showed no difference in calculated proton-induced SEU cross section when a W overlayer was present. Fig. 27 shows the great importance of model validation with experimental data.

The reason for the behavior of the Geant4 Bertini Cascade model seen in Fig. 27 was investigated by looking at proton-W secondary particles with MRED. The simulations showed that the Bertini Cascade was predicting high-LET secondary particles from proton-induced fission for both 200 and 500 MeV protons, however the branching ratios for the production of these particles were one to two orders of magnitude lower than the branching ratios calculated with the Geant4 Binary Cascade model. Note that even though this model includes proton-induced spallation of W, it shows no predicted difference in the charge collected cross section for the device with W

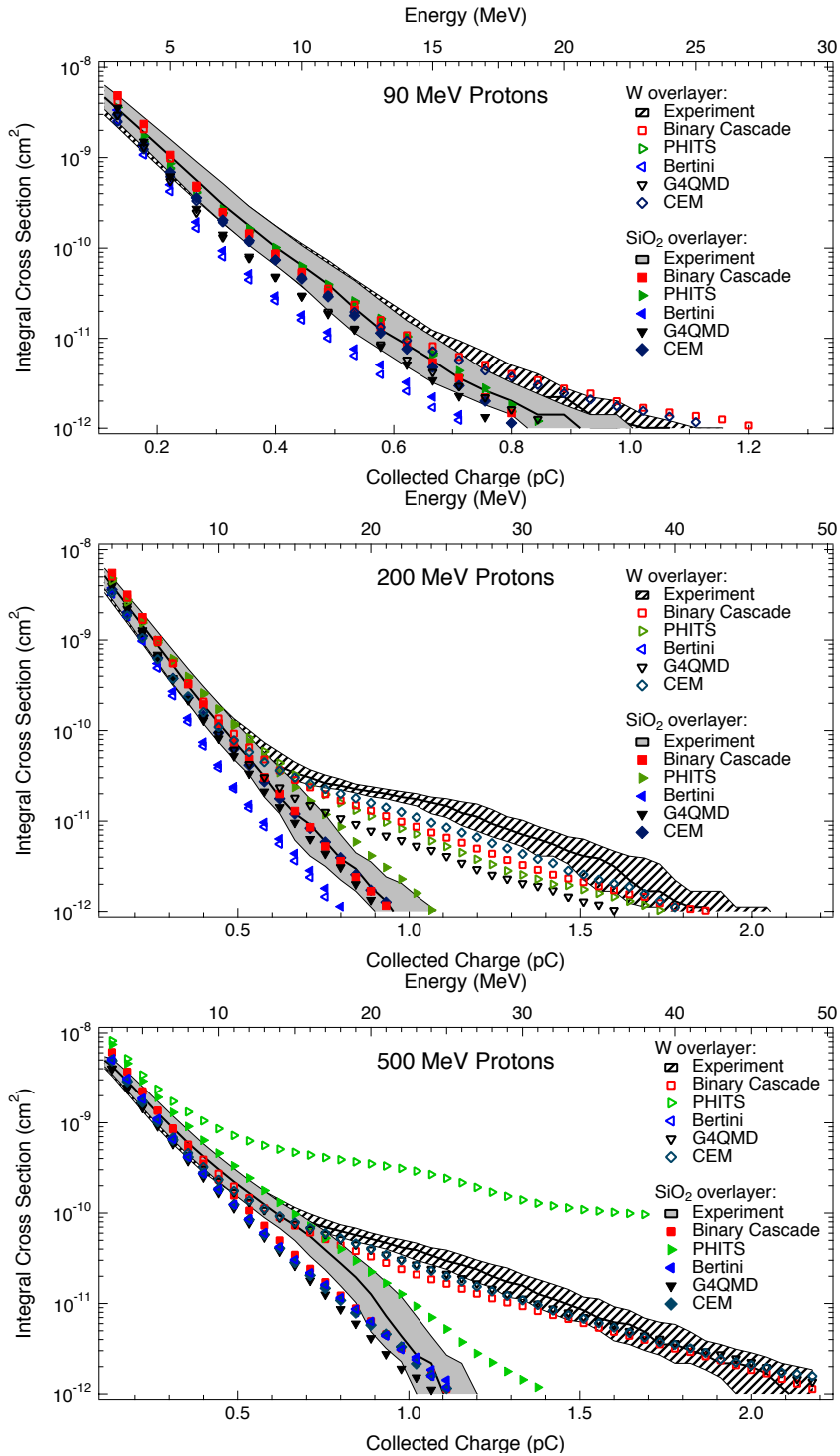


Figure 27 Comparison of computer simulations done with MRED calling different hadronic physics models for 90, 200 and 500 MeV protons normally incident on both of the diode structures shown in Fig. 17. The shaded bands representing the experimental data are plotted as such to represent the uncertainty in the energy calibration of the data. The CEM model is seen to provide the best overall comparison with the experimental data and is thus used for the remainder of the simulations in this paper. Published in [14].

overlayers, and that with only SiO₂ overlayers.

Overall, the CEM model agrees the most closely with experimental data for all three energies and both diode configurations. Thus, CEM was used as the hadronic nuclear physics model in the MRED simulations done for the remainder of this work.

Proton-Induced Nuclear Reactions

Proton-induced SEEs are not typically caused by direct ionization from protons, but by secondary particles from proton-induced nuclear reactions. In order to understand what types of secondary particles are produced by such reactions on silicon, MRED simulations were done which capture the secondary particle charge, energy, and angle (with respect to the direction of the incident proton). The LET values of the secondary particles were calculated using the Geant4 stopping power libraries [67]. To gain insight into the emission angles of high-LET secondaries, the angular distributions are plotted for three different ranges of LET values. 10⁵ incident protons were simulated for 90, 200, and 500 MeV incident protons on silicon nuclei as shown in Fig. 28. In the simulations, the secondary particles with an LET greater than 10 MeV·cm²/mg (all of the LET values are calculated in silicon) comprise fragments ranging from sodium (Z=11) to phosphorous (Z=15). The maximum observed LET particle was a phosphorous ion with an LET of 14.3 MeV·cm²/mg. Fig. 28 reveals that for 90 MeV protons, almost all of the high-LET secondary particles tend to be forward directed, while for the 200 and 500 MeV protons, the high-LET secondary particle distribution becomes broader in angular distribution. This would account for the increase in the angular dependence of proton-induced SEUs for lower energy protons observed in [74].

Fig. 29 shows the corresponding plots for 90, 200, and 500 MeV protons incident on ¹⁸⁴W. Again, 10⁵ incident protons were simulated and the secondary particles were

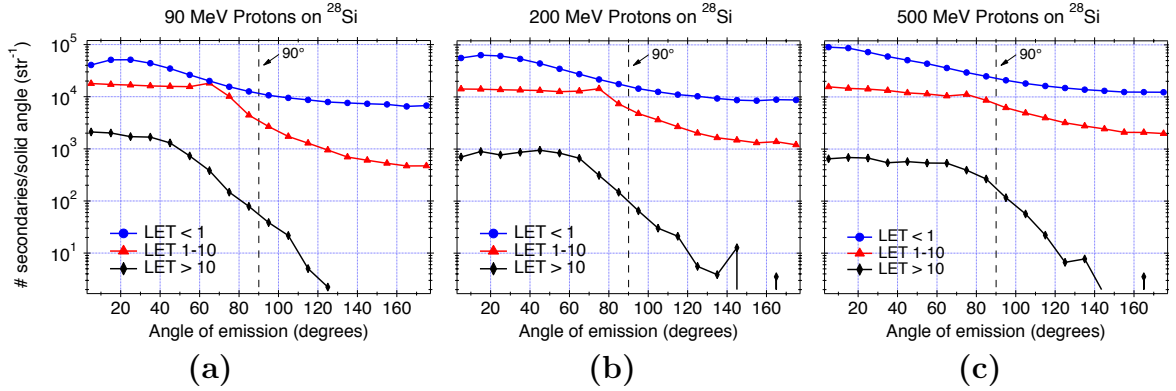


Figure 28 Calculated angular distribution of secondary particles from 90, 200 and 500 MeV protons colliding with silicon nuclei. 10^5 total incident protons were simulated and the secondary particles are grouped according to their LET value (in Si) in $\text{MeV}\cdot\text{cm}^2/\text{mg}$. Published in [14].

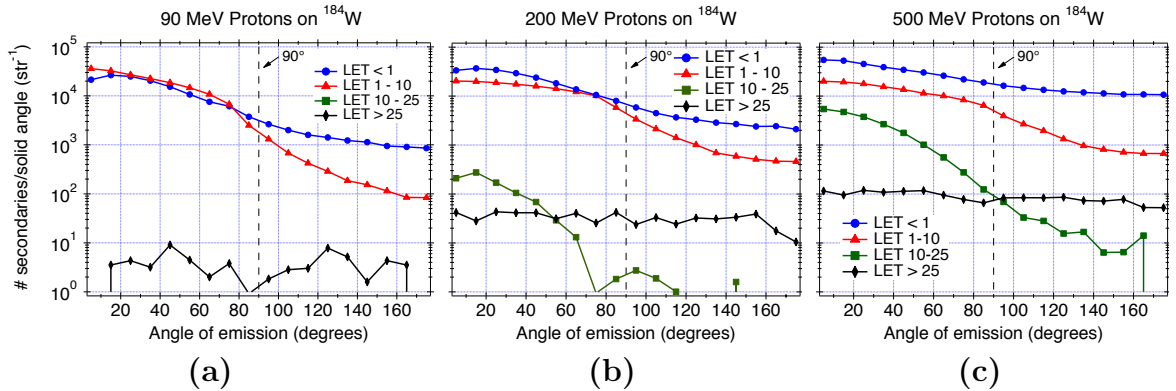


Figure 29 Calculated angular distribution of secondary particles from 90, 200 and 500 MeV protons colliding with tungsten nuclei. 10^5 total incident protons were simulated and the secondary particles are grouped according to their LET value (in Si) in $\text{MeV}\cdot\text{cm}^2/\text{mg}$. Published in [14].

grouped according to their LET values and plotted versus emission angle. In this case, the secondaries with an LET greater than $10 \text{ MeV}\cdot\text{cm}^2/\text{mg}$ range from sulfur ($Z=16$) to rhenium ($Z=75$). All of the fragments with an LET greater than $25 \text{ MeV}\cdot\text{cm}^2/\text{mg}$ are originate from proton-induced fission. These fission fragments have a maximum observed LET value of $42 \text{ MeV}\cdot\text{cm}^2/\text{mg}$, and particle species ranging from germanium ($Z=32$) to tin ($Z=50$). The ranges of these fission products are between $4 \text{ }\mu\text{m}$ and $22 \text{ }\mu\text{m}$. So sensitive volumes within $\approx 20 \text{ }\mu\text{m}$ of tungsten in an integrated circuit have the potential to effected by proton-induced fission products and these products have the possibility of producing unexpected SEEs in devices [6]. In addition, two fission fragments from a single proton-W collision, both with a long range, and a high LET, have the potential to cause proton-induced multiple-bit upsets in devices that have closely spaced sensitive volumes, although these events would be rare.

A comparison of Figs. 28 and 29 reveals that high-LET secondary particles ($\text{LET} > 10 \text{ MeV}\cdot\text{cm}^2/\text{mg}$) have a significantly more isotropic emission for proton-W reactions than for proton-Si reactions. In fact, the proton-induced fission fragments with an $\text{LET} > 25 \text{ MeV}\cdot\text{cm}^2/\text{mg}$, are seen to be almost completely isotropic in their emission. This is because proton-induced fission of W occurs in the latter stages of a nuclear reaction, after the reaction has reached equilibrium and the excited nucleus doesn't have a memory of the initial direction of the incident particle. For the proton-spallation reaction (such as those depicted in Fig. 28), many of the high-LET secondary particles are the residual nucleus after and their emission angle is somewhat dependent on the direction of the incident proton. Thus, the high-LET secondary particles from the proton-induced spallation reaction do show a higher probability of being emitted in the forward direction. This is in agreement with the backside irradiation measurements shown in Fig. 26.

Conclusions

Experimental data presented here show that the presence of high-Z materials, like tungsten, can significantly increase the charge collection cross section for high incident proton energies, and large charge collection events. This means that high-Z materials can increase the proton-induced SEU cross section for high-energy protons and high critical charge devices. The SEU cross section will increase with higher energy protons for a device with any critical charge, but the effect is more dramatic for devices with a high critical charge. Monte Carlo simulations show that the high-LET secondary particles from a proton-W collision originate from proton-induced fission. These fission fragments are seen to have an LET greater than $25 \text{ MeV}\cdot\text{cm}^2/\text{mg}$, are emitted isotropically and have a range up to $\approx 20 \text{ }\mu\text{m}$.

CHAPTER V

MECHANISMS OF NEUTRON-INDUCED SINGLE EVENT EFFECTS

Introduction

Neutron-induced single event upsets (SEUs) have become a major concern for the reliability of modern and developing semiconductor technologies [8, 9]. As device dimensions continue to shrink, the susceptibility to neutron-induced multiple bit upsets (MBUs) in static random access memories (SRAMs) is increasing [75, 76]. Recent studies have shown that MBUs must be taken into account for 130 nm and smaller technology nodes [76]. Although error correcting codes and bit interleaving can effectively reduce the MBU rate, they increase the memory complexity and access time, and may not be suitable for all memories [29, 47].

Neutrons are not ionizing particles, and thus cannot directly cause SEUs. Neutron-induced SEUs are caused by secondary particles from nuclear interactions between energetic neutrons and the materials in and around a device. Modern semiconductor devices are composed of many materials other than silicon, aluminum, and SiO₂. It is important for current and future technologies to understand how these materials can affect SEU susceptibility. It has been shown that high-energy protons (>100 MeV) can trigger fission events in tungsten (W), and that the resulting fission fragments can have a significantly higher linear energy transfer (LET) and a longer range than silicon or oxygen recoil atoms (see Chapter IV). It is known that highly energetic neutrons can also trigger fission events in otherwise stable W nuclei [77], but it has

not been assessed how significant these events are for devices in a terrestrial neutron environment, nor has the impact of these events on MCUs/MBUs been analyzed.

It is ideal to qualify parts in a radiation environment that is as similar to the natural one as possible. There are a few facilities that provide accelerated neutron testing with an energy spectrum similar to that of the natural terrestrial environment [10]. However, due to cost and accessibility, alternative test methods for neutron vulnerability of electronic devices have been investigated [11,12].

In [12], a comparison was made of the single event upset (SEU) cross sections measured using a monoenergetic 14 MeV neutron source and the at Los Alamos National Laboratories' Weapons Nuclear Research (WNR) facility as shown in Fig. 30. It was observed that, for multiple SRAMs from various technology nodes, the SEU cross section measured using 14 MeV neutrons was within a factor of two of that measured using WNR neutrons. Since the data in [12] were based on only measured cross sections for devices with feature sizes ≥ 90 nm and no MBU data were available for such devices, no MBU data were included in [12]. The results presented in this chapter extends the work of [12] by utilizing the results calibrated Monte Carlo calculations to obtain the SEU and multiple cell upset (MCU) responses of a prototypical 65 nm SRAM, and comparing the responses to both 14 MeV and WNR neutron fields.

In this chapter, experimental charge collection data are presented that demonstrate the effect that high-Z materials near sensitive volumes can have on SEUs for devices in a terrestrial neutron environment. For each charge collection event the incident neutron's time-of-flight (TOF) was measured, thereby showing the effect that neutron energy has on charge deposition. Through Monte Carlo simulations, the effect that high-Z materials and neutron energy can have on SEUs and MCUs is investigated for a representative SRAM structure. Finally, we compare the simulated SEU and MCU response of this SRAM structure when exposed to the WNR neutron

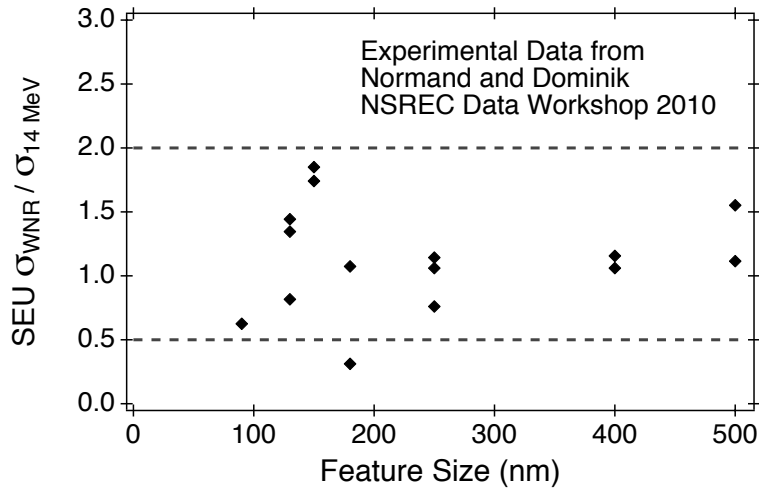


Figure 30 Ratio of experimental SEU cross sections measured with the WNR neutron spectrum to 14 MeV neutrons. Data from Normand and Dominik [12].

spectrum and to a monoenergetic 14 MeV neutron beam.

Charge Collection Measurements

The charge collection data from the normal incidence and grazing angle neutron irradiations done with the T4FP15L beamline are shown in integral cross section form in Fig 31. The large steps at high charge collection values in the plot represent single events in the integrated curve. Since the data are rare for these high charge collection values, the curve remains at a given cross section value until, at a lower charge value, another event is integrated over. Thus, the curves appear smooth at low charge collection values where there are many events and have large steps at high charge collection values where events are rare.

Fig. 31 shows that for a minimum charge collected, Q_{min} , less than 0.6 pC, the effect of the W layer on the charge collection cross section is minor. However, for high Q_{min} , the presence of W can significantly increase the charge collection cross section. These additional high charge collection events are caused by highly ionizing secondary

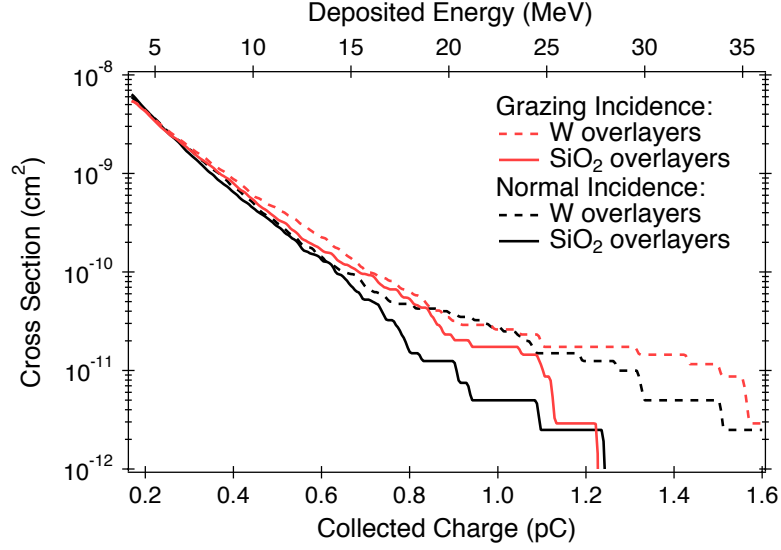


Figure 31 Experimental charge collection cross section curves for the diodes irradiated with the Los Alamos T4FP15L neutron beamline. Published in [15].

particles from neutron-W collisions. By comparing the two device orientations, we see that the grazing angle neutrons increase the charge collection cross section for collected charge greater than 0.6 pC only for the diodes with SiO₂ overlayers. This is because the highly ionizing secondary fragments from neutron-Si collisions tend to the forward direction and these fragments are more likely to traverse the length of the sensitive volume for neutrons incident at grazing angles [75]. Conversely, the two cross section curves for the diodes with W overlayers are similar which indicates that the highly ionizing secondary particles are emitted isotropically from the neutron-W collision. This suggests neutron-induced fission in W, and not neutron-induced spallation with W, as the mechanism. Monte Carlo simulations of the diodes confirm that neutron-induced fission is the main cause of the high charge collection events in the diodes with a W overlayer.

For each charge collection event, TOF measurements were made on the incident neutron. Fig. 32 shows a scatter plot of the neutron energy and corresponding charge

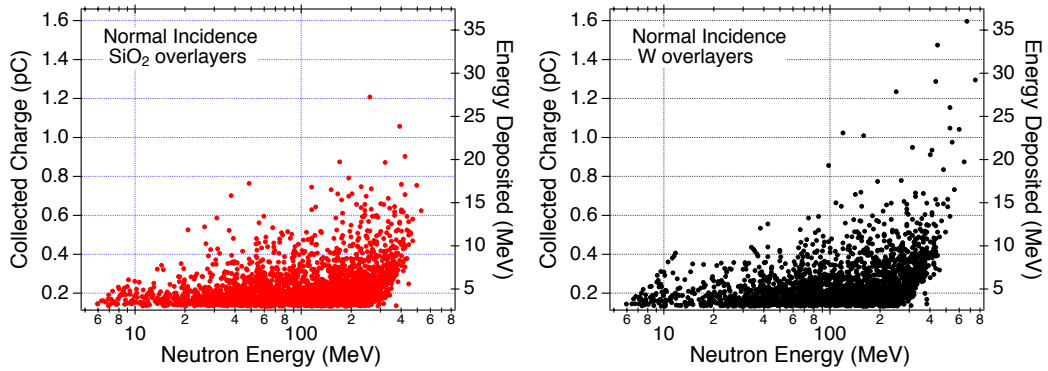


Figure 32 Scatter plots of collected charge versus neutron energy for normally incident neutrons. Neutron energies were measured by time of flight in the Los Alamos T4FP15L neutron beamline. Published in [15].

collected for both diode overlayer configurations. These data show a trend indicating that the higher energy neutrons cause the largest charge collection events, as one would expect. From these data, we can conclude that for devices with a high critical charge, Q_{crit} , low energy neutron beams would greatly under predict the SEU cross section and could even incorrectly predict a device to be single event latchup (SEL) immune to terrestrial level neutrons (see [6, 14]).

SEU and MCU Simulations

Monte Carlo Simulations

For the Monte Carlo computer simulations performed in this study, the Monte Carlo Radiative Energy Deposition (MRED) simulation tool developed at Vanderbilt University was used [43]. MRED version 9.1.2 is based on Geant4 version 9.4. In Chapter IV and [14, 69, 70] it was shown that the hadronic-physics model (used for incident protons and neutrons) available in MRED that most closely compares with experimental data is the Cascade Exciton Model (version CEM03.03) [71]. The validation of CEM included comparisons with experimental cross section data of proton-induced

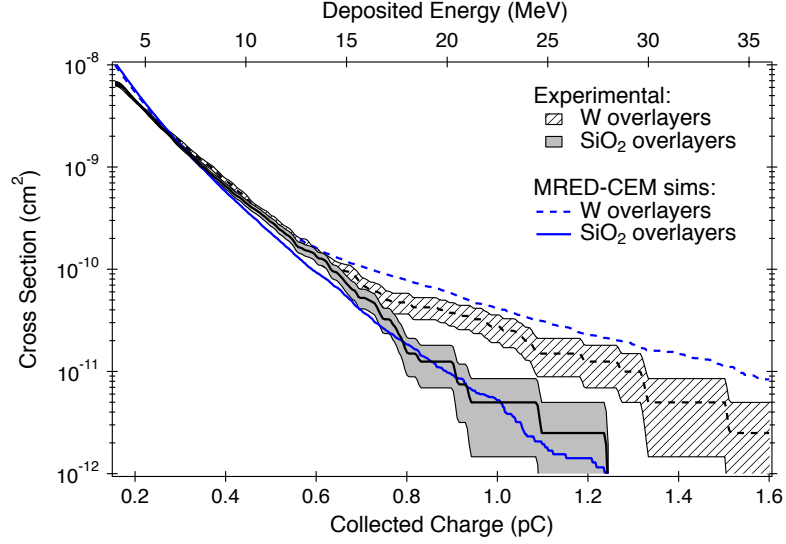


Figure 33 Comparison of experimentally measured charge collection cross sections and MRED simulations. The grey and hatched areas represent uncertainties due to counting statistics. Published in [15].

fission cross sections for multiple high-Z elements, including W [71].

The experimental charge collection data were used to validate MRED with CEM for a spectrum of incident neutron energies for devices with W overlayers and SiO₂ overlayers, as shown in Fig. 33. The grey regions shown around the experimental data in Fig. 33 represent the error bars due to counting statistics. Additional uncertainties in the experimental data come from uncertainties in the charge collection calibration and in the neutron energy spectrum. These uncertainties are not represented in the figure, and it is believed that they are the main cause of the discrepancies between the experimental and simulated cross section curves. CEM is the nuclear physics model used for all of the MRED simulations presented in this chapter.

In [46], Sierawski *et al.* developed a nested sensitive volume model using MRED for the bits of an SRAM fabricated in a commercial 65 nm bulk CMOS process. This model was validated with experimental SEU data on the SRAM for incident heavy ions, high-energy protons and low-energy protons. The estimated critical charge, Q_{crit} ,

for this device is 1.3 fC, which is about the typical Q_{crit} value for a non-SEU-hardened 65 nm SRAM. SEU hardening techniques have been shown effective in increasing the estimated Q_{crit} value of SRAMs by up to a few orders of magnitude [78]. For this reason, the MRED cross section calculations shown in the following sections are plotted as a function of Q_{crit} out to values as high as 50 fC.

This nested sensitive volume model was used in this work to create a 32×32 bit matrix with appropriate bit spacing for MRED simulations of neutron-induced SBUs and MCUs. In each simulation, a minimum of 10^9 neutrons were irradiated at normal incidence at randomized over the surface of the structure. The amount of charge deposited in the sensitive volume groups of each bit from each incident neutron was recorded for post processing. To decrease the runtime of the simulations, cross section biasing techniques were used in MRED (see [43,68]). Checks were performed to assure that the cross section biasing didn't effect the overall cross section calculations.

Effect of W Overlayer on MCU Response

Using the 32×32 bit SRAM structure described above, two device overlayer configurations were simulated: one with only silicon overlayers, and one with silicon overlayers and a thin W overlayer directly above the sensitive volumes. The thickness of the W overlayer is the same as the thickness of typical W vias in a device. This was done to investigate the effect that W vias can have on neutron-induced SBUs and MCUs. Because the W overlayer in these simulations is a complete overlayer rather than W vias, the effects from the W shown in Figs. 4 and 5 are a worst-case scenario and do not represent realistic device overlayers. Comparisons of the cross section curves of these two overlayer configurations are shown as a function of Q_{crit} in Figs. 34 and 35 for SBUs and for 2, 3, and 4 bits upset (BU).

Fig. 34 shows that for $Q_{\text{crit}} < 27$ fC, the W overlayer has no effect on the SBU

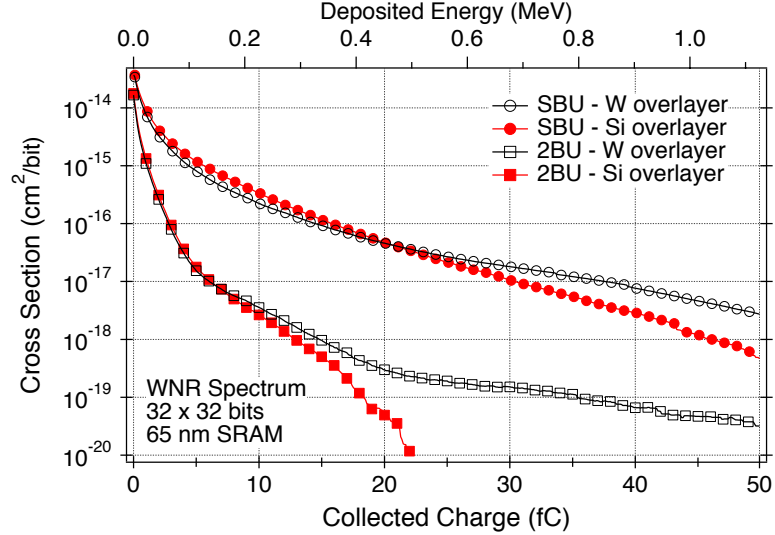


Figure 34 Simulated SBU and 2BU response of the 65 nm SRAM structure to the WNR neutron spectrum for two different overlayer configurations. Published in [15].

cross section, but does cause a significant increase in the SBU cross section for higher Q_{crit} values. The effect that W has on the 2BU cross section for $Q_{\text{crit}} > 16$ fC is more pronounced, causing an increase of over an order of magnitude in the 2BU cross section for $Q_{\text{crit}} > 21$ fC. For the structure without a W overlayer, no 2BU events were observed for $Q_{\text{crit}} > 24$ fC, while 2BU events were observed for $Q_{\text{crit}} > 50$ fC for the structure with a W overlayer.

Fig. 35 shows that the W overlayer will affect the MCU cross section more significantly for higher MCU multiplicity. However, for a device with a Q_{crit} of 1-2 fC (typical Q_{crit} for an unhardened 65 nm SRAM), the MCU events which effect 5 or more bits constitute about 1% of the total MCU events (see Fig. 40). Additionally, Fig. 35 shows that the W overlayer has no significant effect on the MCU cross section for MCU events which effect 2-4 bits at this Q_{crit} . Thus, for a device with this Q_{crit} , the presence of a W overlayer won't significantly affect the SBU or MCU cross section, and the presence of W will only effect high- Q_{crit} devices.

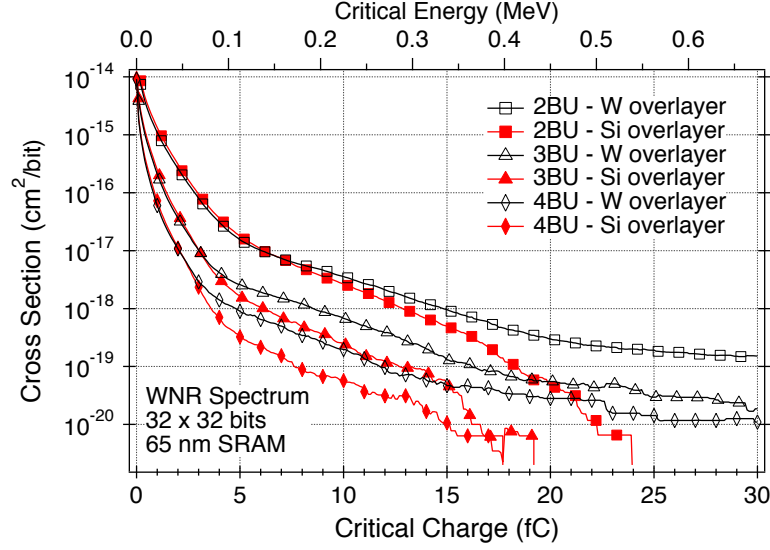


Figure 35 Simulated 2, 3 and 4 BU response of the 65 nm SRAM structure to the WNR neutron spectrum for two different overlayer configurations. Published in [15].

WNR and 14 MeV Neutron Spectra Compared

Simulations performed with the 32×32 bit SRAM structure described above without the W overlayer were used to compare the SBU response of the device in the WNR neutron spectrum with the SBU response in a monoenergetic 14 MeV neutron beam, similar to the experimental study reported in [12]. Additionally, the MCU response to the different neutron energies was investigated via simulations. The cross section curves for these simulations are shown in Figs. 36 and 37.

Fig. 36 shows that for $Q_{\text{crit}} < 27$ fC, the SBU cross section curves for the 14 MeV neutrons and the WNR neutron spectrum agree to within a factor of 2. This is in agreement with the trend published in [12] (see Fig. 30). However, for higher Q_{crit} values, this is not the case and the 14 MeV neutrons underestimate the SBU cross section. These results suggest that a 14 MeV neutron beam can approximate SEU testing at a facility with a neutron spectrum only for SRAMs with an adequately low Q_{crit} , or small enough feature size. This can be seen in testing that was performed on

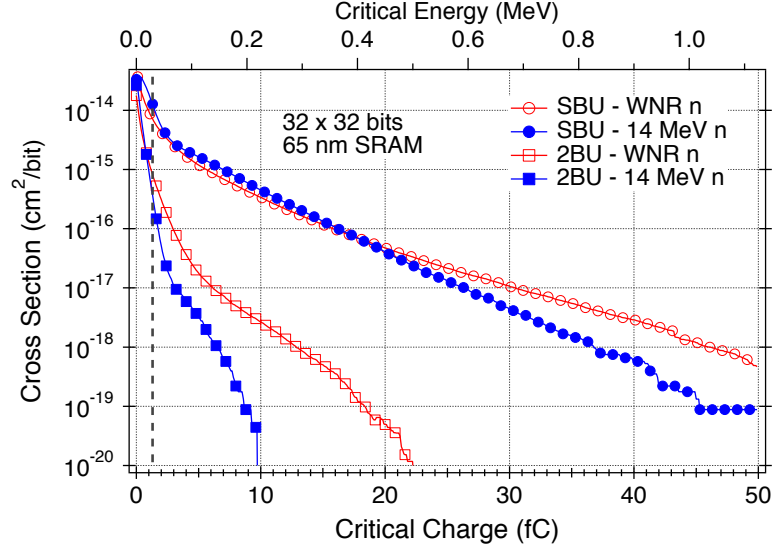


Figure 36 Simulated SBU and 2BU response of the 65 nm SRAM structure to WNR neutrons and 14 MeV neutrons. The dotted grey line marks the critical charge value of 1.3 fC. Published in [15].

older SRAMs from the 1990s that had higher Q_{crit} values and for which the 14 MeV neutron cross section was low compared to the WNR cross section by factors of 3-5 [79].

Fig. 36 also shows that the 2BU cross-section curves agree within a factor of 2 only for $Q_{\text{crit}} < 1.2$ fC, and that 14 MeV neutrons significantly underestimate the 2BU WNR response for higher Q_{crit} values. Fig. 37 shows that for 3+BU events, the 14 MeV neutrons drastically underestimate the MCU cross section except at extremely low (< 0.6 fC) Q_{crit} values.

The ratio of the MCU cross sections of the WNR spectrum to that of the 14 MeV neutrons is shown in Fig. 38, taking Q_{crit} to be 1.3 fC. The trend in Fig. 38 is clear: the 14 MeV neutrons are unable to accurately estimate the MCU response of the SRAM, and the higher the MCU multiplicity, the poorer the agreement. This is because the secondary particles from the 14 MeV neutrons are unable to deposit large amounts of charge across multiple bits.

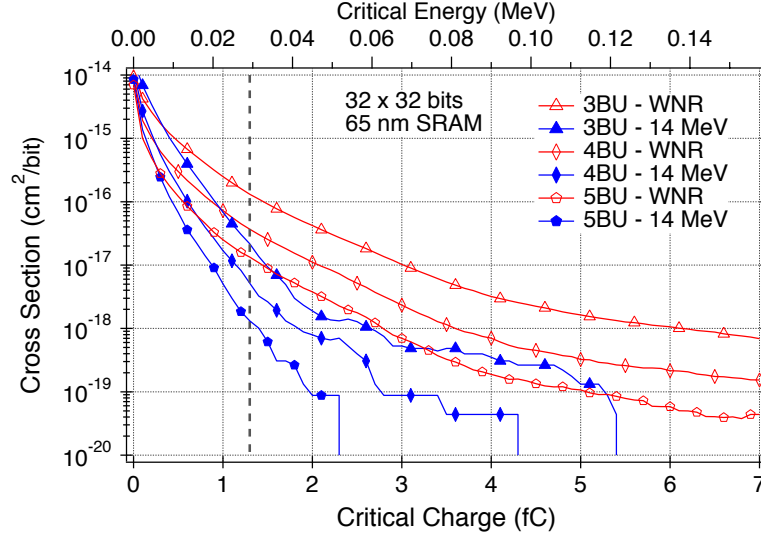


Figure 37 Simulated 3, 4 and 5BU response of the 65 nm SRAM structure to WNR neutrons and 14 MeV neutrons. The dotted grey line marks the critical charge value of 1.3 fC. Published in [15].

In order to understand the mechanism of 14 MeV neutron-induced MCU events, the types of neutron-silicon reactions must be analyzed. Table 4 shows the list of available reaction channels, both elastic and inelastic, which produce ionizing secondary particles from a 14 MeV neutron-silicon reaction. The corresponding cross section values for each reaction are taken from the Evaluated Nuclear Data File [80]. Since the maximum range of the heavy ion recoils (silicon, aluminum and magnesium) from 14 MeV neutron elastic and inelastic collisions is less than $2 \mu\text{m}$, they are unable to cause more than the occasional 2BU event. The proton and deuteron secondary particles can have an LET which is high enough to deposit more than 1.3 fC in a sensitive volume [47], but not in multiple sensitive volumes since these particles are only able to deposit this amount of charge at the end of their trajectories.

Thus, the 14 MeV neutron MCU events are largely caused by alpha particles produced in $^{28}\text{Si}(n,\alpha)^{25}\text{Mg}$ reactions, which have a sufficient range to deposit femto-coulombs of charge in multiple cells. The $^{28}\text{Si}(n, n + \alpha)^{24}\text{Mg}$ reaction also contributes to the MCU events, however the cross section for this reaction is roughly an order

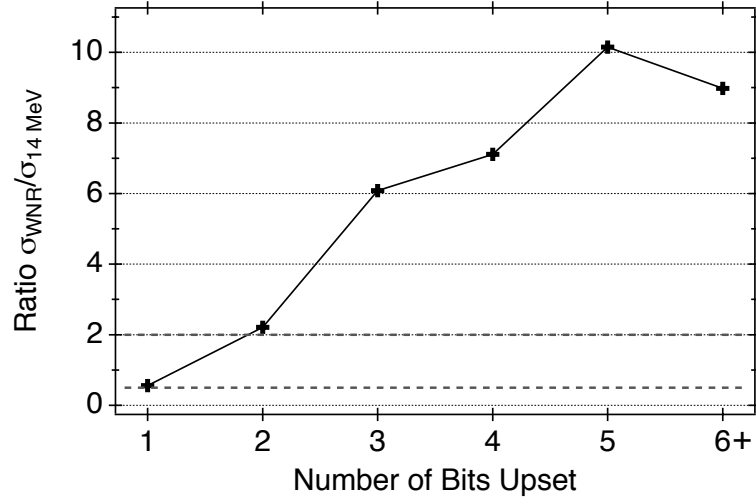


Figure 38 Ratio of simulated MCU response of 65 nm SRAM structure for WNR neutrons to 14 MeV neutrons. The dotted grey lines mark ratios of 0.5 and 2. Published in [15].

Table 4 14 MeV Neutron-Silicon Reactions Producing Ionizing Secondaries

Reaction	Cross section (b)
$^{28}\text{Si}(n, n)^{28}\text{Si}$ (Elastic)	0.662
$^{28}\text{Si}(n, n)^{28}\text{Si}$ (Inelastic)	0.522
$^{28}\text{Si}(n, p)^{28}\text{Al}$	0.279
$^{28}\text{Si}(n, d)^{27}\text{Al}$	0.019
$^{28}\text{Si}(n, \alpha)^{25}\text{Mg}$	0.178
$^{28}\text{Si}(n, n + p)^{27}\text{Al}$	0.075
$^{28}\text{Si}(n, n + \alpha)^{24}\text{Mg}$	0.018

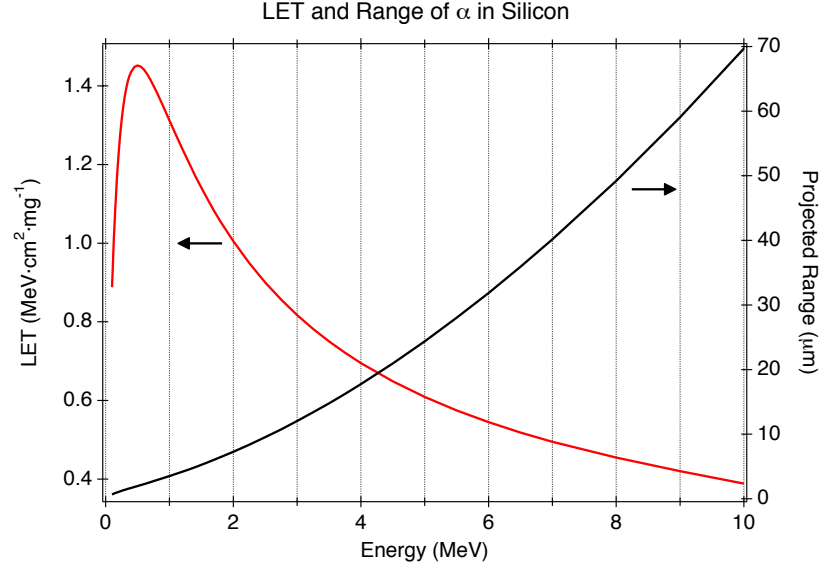


Figure 39 The range and LET of alpha particles in silicon. Data generated by SRIM [65].

of magnitude lower than the $^{28}\text{Si}(n,\alpha)^{25}\text{Mg}$ reaction. Fig. 39 shows the range and LET of energetic alpha particles in silicon. This figure shows that alpha particles can have a relatively long range while also having a sufficiently high LET over this range to deposit enough charge to cause upsets over multiple sensitive volumes. The MRED simulations show that this mechanism is the dominant one causing 14 MeV neutron-induced MCU events with cross sections roughly equal to those in Table 4.

The reason for the trend shown in Fig. 38 is that the high-energy neutrons from the WNR spectrum are able to produce silicon recoils with a range of several microns, and these recoils can cause high- Q_{crit} MCU events. It is important to note, however, that for an SRAM with Q_{crit} of about 1 fC, the MCU cross section for 14 MeV and WNR neutrons agrees to within a factor of 2. Given that the Q_{crit} of a device is not well defined, and can even vary for different sensitive nodes within a device [27], it is possible that a 14 MeV neutron beam could be used in place of the WNR neutrons for MCU testing of a device with a sufficiently low Q_{crit} . It should not be assumed, however, that this is the case for a device. At this point, only testing with WNR

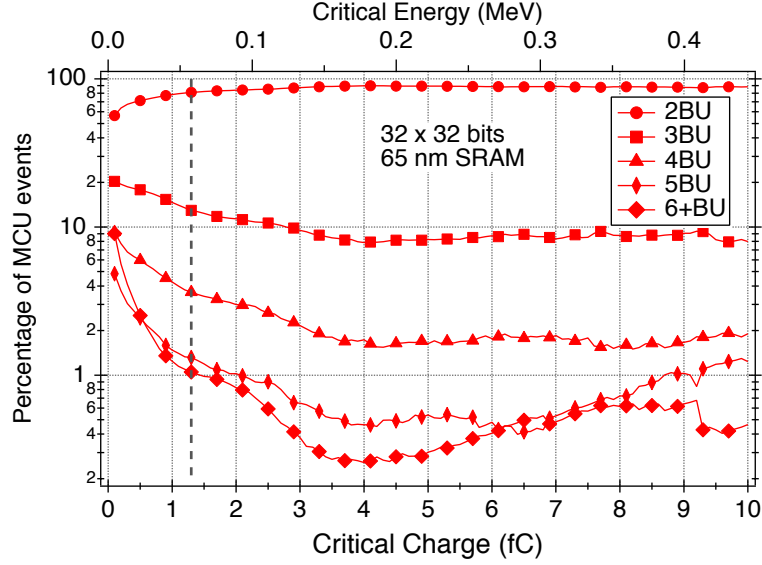


Figure 40 Computed percentage of total MCU response for 2 to 6+BU events in a 65 nm SRAM exposed to the WNR neutron spectrum. The dotted grey line marks the Q_{crit} of 1.3 fC. Published in [15].

neutrons is sure to give an accurate MCU cross section.

The percentage of the total MCU events for each MCU multiplicity is shown as a function of Q_{crit} in Fig. 40. These MCU events were simulated using the 65 nm SRAM structure in the WNR neutron environment. For a device with a Q_{crit} of 1.3 fC, 2BU events constitute 81% of the total MCU events, and this percentage increases to about 88% for higher Q_{crit} values. 3BU events constitute about 13% of the total MCU events at this Q_{crit} , and they continue to account for roughly 10% of the total MCU events for higher Q_{crit} values. Thus for an SRAM which doesn't employ bit interleaving techniques, the majority of MCU events are 2 or 3 bit upsets. However, for lower Q_{crit} values (<0.5 fC), the higher MCU multiplicities constitute a significant percentage of total MCU events.

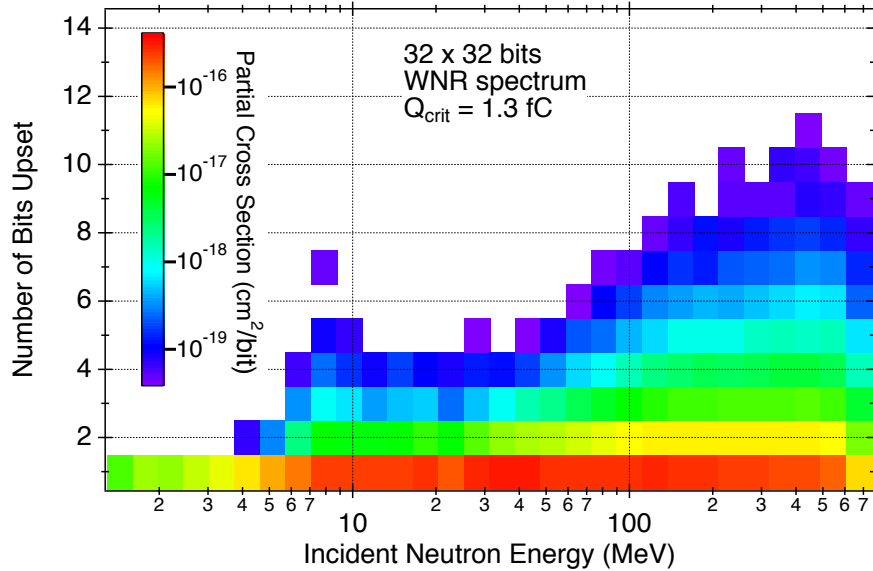


Figure 41 Simulated 3-D cross section plot for the 65 nm SRAM MCU response to the WNR neutrons for $Q_{\text{crit}} = 1.3 \text{ fC}$. Published in [15].

Effect of Neutron Energy on MCUs

In order to investigate the role that neutron energy plays in the MCU response to the WNR neutron spectrum, the simulation data from the 32×32 bit SRAM structure with only silicon overlayers were plotted in a 3-D cross section plot in Fig. 41. For this plot, the incident neutron energy was correlated with the resulting MCU event, and the events were histogrammed in logarithmically spaced bins. The neutron energies were also sampled logarithmically so that the same number of neutrons was simulated for each energy bin. The color scale represents a partial cross section, so that if all of the cross sections for a given MCU multiplicity are summed, the result would be the total MCU cross section. The WNR spectrum is factored into the cross section calculation so that events are weighted according to the corresponding neutron flux in Fig. 42.

Plotting the data in this way shows how neutrons of different energies contribute to the overall MCU response for the WNR spectrum. Fig. 41 shows that for the

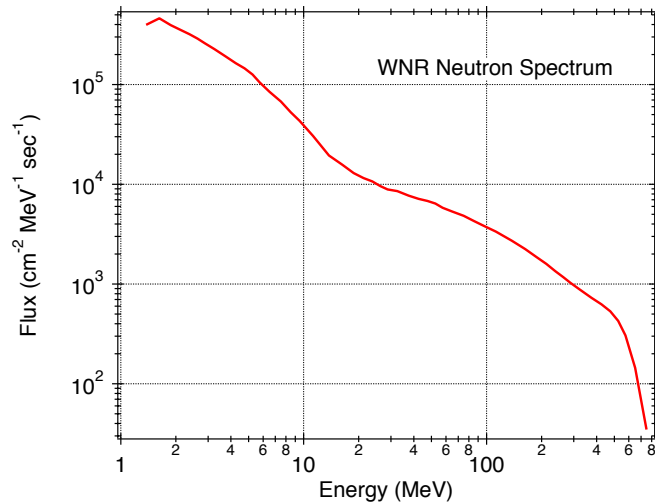


Figure 42 WNR neutron energy spectrum used in the computer simulations [15].

SBU response of this device, the high-energy neutrons (>100 MeV) contribute less to the overall SBU response than medium-energy neutrons (10-100 MeV). This is partially because the high-energy neutrons are about an order of magnitude lower in abundance (see WNR spectrum in Fig. 42). However, about 60% of the 2BU events are caused by high-energy neutrons and 80-90% of the 3+BU events are caused by neutrons with energy > 100 MeV.

For the 65 nm SRAM with a Q_{crit} of 1.3 fC, 89.7% of all of the simulated bit upsets were SBUs, and 10.3% were MCUs, the majority of these being 2BUs. This is in agreement with the data published in [47], which reported 11% of the upsets in the SRAM as MCU events in response to the terrestrial neutron energy spectrum. Fig. 41 shows MCU events in which ten or more bits are upset, while [47] doesn't show any MCU events with a multiplicity greater than five for a device with a Q_{crit} of 1.3 fC. The reason for this apparent disagreement is that the data in Fig. 41 were obtained by simulating a significantly higher neutron fluence than was simulated in [47], so that these low cross section MCU events could be observed.

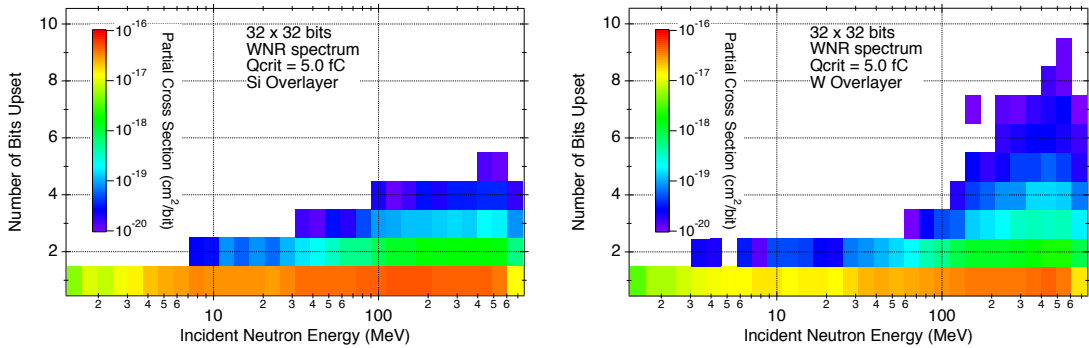


Figure 43 Simulated 3-D cross section plot for the 65 nm SRAM MCU response to the WNR neutrons for $Q_{\text{crit}} = 5.0$ fC. Plots are shown for the SRAM both with and without a W overlayer. Published in [15].

It is important to note the similarities between the experimental TOF data in Fig. 32 and the simulation results in Fig. 41. As was noted in section V, the charge collection events in Fig. 32 that deposit the most charge are caused by secondary particles that traverse this region at grazing angles, similar to trajectories that cause MCU events in the SRAM. We see that the high-energy neutrons are the cause of the majority of the high-charge-collection events, as well as the high-multiplicity MCU events.

The 3-D cross section plot for the SRAM with a W overlayer is very similar to Fig. 41 for a Q_{crit} of 1.3 fC, as one would expect given the data in Figs. 34 and 35. However, there is a difference in the 3-D plots for higher Q_{crit} values. Fig. 43 shows the 3-D cross section plots for SRAMs with only Si overlayers and a thin W overlayer respectively, assuming a Q_{crit} of 5 fC. These data show that nearly all of the 3+BU events are caused by neutron energies > 100 MeV for both overlayer configurations. Fig. 43 shows an increase in high MCU number cross section for the W overlayer SRAM, consistent with Fig. 35. For the W overlayer SRAM, high-energy neutrons cause all of the high multiplicity MCU events. By using MRED to replay these events, the mechanism of most of the 5+BU events is seen to be neutron-

induced fission fragments from a neutron-W collision. One of the energetic and highly ionizing fragments is emitted at a near 90 angle and travels down a column of cells in the SRAM, causing the MCU event. Since the neutron-induced fission cross section is negligible for neutron energies less than 100 MeV, only high-energy neutrons are able to produce these events.

Conclusions

Experimental data and simulations of 65 nm SRAMs presented here show that the presence of high-Z materials, like tungsten, can only increase the SEU cross section for high Q_{crit} (> 27 fC) devices and can only significantly increase the MCU cross section for devices with a $Q_{\text{crit}} > 16$ fC when exposed to the terrestrial neutron environment. This is due to the presence of high-energy (>100 MeV) neutrons. Simulations with a solid W overlayer show that for an unhardened devices with a Q_{crit} of 1-2 fC, the presence of W does not significantly effect the SEU or MCU cross section.

Simulations show that for 65 nm SRAMs with a $Q_{\text{crit}} < 27$ fC, a monoenergetic 14 MeV neutron beam can be used to estimate the SEU response to the terrestrial neutron environment within a factor of two, in agreement with [12]. However, a monoenergetic 14 MeV neutron beam is inadequate to estimate the 2BU response to the terrestrial neutron environment to within a factor of two, except for devices with a very low Q_{crit} (< 1.2 fC). 14 MeV neutrons are not able to adequately simulate the MCU response of devices in the terrestrial neutron environment for 3+BU events (for the device simulated here, these events have a cross-section lower than 10^{-16} cm²/bit i.e. a soft error rate lower than 1.5 FIT/Mb). The experimental data and simulations presented here demonstrate that 14 MeV neutrons produce far fewer high-LET secondary particles than terrestrial neutrons. Thus, in the context of [12], MCUs are similar to SEL in that 14 MeV neutrons should not be used as a substitute for the

response to a spallation neutron source; only high-energy particle beams may be used to obtain accurate SEL and MCU responses.

While the 65 nm SRAM structure simulated in this work shows an MCU percentage of 10.3%, this is not representative of all 65 nm SRAMs. Previous works have shown that the MCU percentage of 65 nm SRAMs can vary greatly and can be as high as 50% or more [81]. Based on the good agreement between simulations and measurements of the SRAM presented in this work and in [47], we have confidence that the simulation can be successfully extended to other SRAMs in which the MCU fraction is much higher.

CHAPTER VI

CONCLUSIONS

The research presented here gives new insights into the mechanisms of proton- and neutron-induced single event upsets (SEUs) relevant to modern-day devices. It is shown via experimental charge collection measurement and Monte Carlo simulations that the presence of tungsten (W) in modern day devices can have an impact on both proton- and neutron-induced SEUs. The mechanism for this is shown to be high-energy proton- and neutron-induced fission in the W nuclei. These induced fission events are seen to produce secondary particles with both a high linear energy transfer (LET) value and a high range and can cause an increase in both the SEU and MCU cross section of a device, depending on the critical charge, Q_{crit} .

The results of experimental time of flight measurements coupled with charge collection measurements and Monte Carlo simulations presented here demonstrate the effect that neutron energy can have on neutron-induced SEUs and MCUs. It is shown that high-energy neutrons are able to produce higher-LET secondary particles with a longer range compared to 14 MeV neutrons. However, it is shown that 14 MeV neutrons are able to cause the same SEU and MCU cross section in an SRAM device with a sufficiently low Q_{crit} . The mechanism for the 14 MeV neutron-induced MCU events is seen to be secondary alpha particles emitted from the $^{28}\text{Si}(n,\alpha)^{25}\text{Mg}$ reaction.

The effect of proton and neutron radiation on semiconducting devices will continue to be an important issue in the developing of new technologies. The research presented here provides a deeper understanding of the mechanisms behind proton-

and neutron-induced radiation effects. As semiconducting devices continue to shrink in size, these results will provide insight which will aid in the testing of devices and the understanding of future observations of radiation effects.

APPENDIX A

LINEAR ENERGY TRANSFER

Overview

The physics of energy loss of particles in matter dates back to the discovery of radioactivity and scientists became interested in how these emitted particles slowed down in matter. However, it wasn't until the atom was better understood that this energy loss could begin to be understood. Using the idea of an atom consisting of a dense, charged nucleus with orbiting electrons as the basis of his derivation, Niels Bohr presented the first unified theory of particle energy transfer, also called stopping power [82]. In his treatment, Bohr deduced that the energy loss to electrons would dominate over energy loss to the nucleus due to the small mass and large abundance of electrons as compared with the nuclei. The derivation was thus of classical Coulomb scattering between the incident ion and electrons modeled as harmonic oscillators.

A quantum mechanics treatment of the problem was done 20 years later by Hans Bethe who solved the problem of the incident ion interacting with an atom of harmonic oscillators in the first Born approximation [83, 84]. Later, Felix Bloch analyzed the differences between the two approaches and showed that the Bohr solution was valid for hard, close collisions, and the Bethe solution was valid for weak scattering [85]. Bloch provided a solution that reduced to the two previous theories in their respective limits in what is now known as the Bethe-Bloch theory. Correction terms have been added to the Bethe-Bloch equation semi-empirically as noted in refs [32, 85–87]. Newer theoretical approaches for calculating the energy loss of ions traversing a material have

been published [88], but the Bethe-Bloch theory still remains as the basis for solving for the energy loss of particles with velocities above 1 MeV/u for computer codes such as SRIM [65, 85]. This appendix briefly covers the basic physics involved in the energy loss calculations, and the limitations of the approximations and assumptions made.

Physics of LET

For energetic ions, the energy loss in materials falls generally along a straight track and most of the energy lost is transferred to the electrons in the material. Thus the use of the term linear energy transfer (LET). Although the energy lost by the ion is not exactly the same as the energy transferred to the material, the term LET is often used interchangeably with energy loss or stopping power. The average LET in a material is related to the cross section for individual collisions by

$$LET = \sum_i N_i \sum_n E_{n,i} \sigma_{n,i} \quad (6)$$

where N_i is the atomic density, and $\sigma_{n,i}$ is the cross section for the ion to raise the atom of type i to an energy level $E_{n,i}$ above its ground state. The cross section for a given atom of type i in the first order Born approximation with the electromagnetic interaction, V , between the ion and the target atom is taken as a differential with the final momentum p' as [83]

$$d\sigma_n = \frac{2\pi}{\hbar v} |\langle \mathbf{p}', n | V | \mathbf{p}, 0 \rangle|^2 \delta(E' + E_n - E) \frac{d\mathbf{p}'}{h^3}. \quad (7)$$

Here p , E , and v are the initial momentum, energy and velocity of the incident ion and the primed variables are after the collision. The equation is better put in terms of the momentum transfer $\mathbf{q} = \mathbf{p} - \mathbf{p}'$, since this relates to the kinetic energy

of the electron, Q . With the change of variables and some manipulation, eq. 7 can be rewritten as

$$d\sigma_n = \frac{m}{2\pi\hbar^4 v^2} |\langle \mathbf{p}', n | V | \mathbf{p}, 0 \rangle|^2 \left(1 + \frac{Q}{m_e c^2} \right) dQ. \quad (8)$$

The electromagnetic interaction contained in the Dirac brackets in eq. 8 is divided into two terms for the charge and the spin interactions. In the Coulomb gauge, these interactions are modeled by two terms: a static Coulomb potential, and by the emission and absorption of a virtual photon by the incident ion at position \mathbf{r} and the electron at position \mathbf{r}' . Sparing the details that can be found in ref. [86], eq. 8 becomes

$$d\sigma_n = \frac{2\pi z^2 e^4}{m v^2} Z \left[\frac{|F_n(\mathbf{q})|^2}{Q^2(1 + Q/m_e c^2)^2} + \frac{|\boldsymbol{\beta}_t \cdot \mathbf{G}(\mathbf{q})|^2}{[Q(1 + Q/m_e c^2) - E_n^2/2mc^2]^2} \right] \left(1 + \frac{Q}{m_e c^2} \right) dQ. \quad (9)$$

$$F_n(\mathbf{q}) = Z^{-1/2} \sum_j \langle n | e^{2\pi i \mathbf{q} \cdot \mathbf{r}_j / \hbar} | 0 \rangle$$

$$\mathbf{G}_n(\mathbf{q}) = Z^{-1/2} \sum_j \langle n | \boldsymbol{\alpha}_j e^{2\pi i \mathbf{q} \cdot \mathbf{r}_j / \hbar} | 0 \rangle$$

At this point, three regions are considered:

1. For low Q , $F_n(\mathbf{q})$ and $\mathbf{G}_n(\mathbf{q})$ are evaluated by expanding the exponential and keeping the lowest order terms. This assumes that \hbar/q is much smaller than r .
2. For intermediate Q , the transverse electromagnetic term, \mathbf{G}_n is taken to be negligible and the relativistic terms of order Q/mc^2 are dropped.

3. For high Q , the binding energy of the electrons are neglected and the initial and final states of the electrons are taken to be that of free electrons.

The theory at this point relies on the assumption that the three regions can accurately be pieced together. Eq. 9 is then integrated over region 1 from Q_{min} to Q_1 and summed with integrals over regions 2 from Q_1 to Q_2 and 3 from Q_2 to Q_{max} . The result of which is (with corrective factors C/Z and δ)

$$LET = N \sum_n E_n \int_{Q_{min}}^{Q_{max}} d\sigma_n \quad (10)$$

$$= \frac{4\pi z^2 e^4}{m_e v^2} NZ \left[\ln \left(\frac{2mv^2}{I} \right) - \ln(1 - \beta^2) - \beta^2 - \frac{C}{Z} - \frac{\delta}{2} \right]$$

where z and Z are the atomic number of the ion and the target atom respectively. The factor I is the mean excitation energy of the atomic electrons specific to a material. The terms v and β pertain to the incident ion. Note that the terms containing Q_1 and Q_2 cancel when adding the integrals. The constants are often lumped together, with the terms containing β in the brackets, so that the equation is written as

$$LET = K z^2 \frac{Z}{A} \frac{1}{\beta^2} \left[f(\beta) - \ln(I) - \frac{C}{Z} - \frac{\delta}{2} \right]. \quad (11)$$

The assumption made in region 1 (low Q) fails if the electron velocity is comparable to the ion velocity. While this assumption holds for most electrons, it fails for some of the more tightly bound electrons. The semi-empirical correction factor C/Z is thus called the “inner shell correction” and is meant to correct for these failures. The region 1 assumption that leads to the expansion of the exponentials also fails if $\mathbf{q} \cdot \mathbf{r}$ is not much smaller than \hbar . In other words, if the material is dense and electrons from neighboring atoms interact. This failure is corrected, also semi-empirically, with the correction factor δ .

The term in brackets in eq. 11 is the first term $L_0(\beta)$ from eq. 1, and is written as the first term in the expansion of the stopping number $L(\beta)$. The higher order expansion terms, $L_1(\beta)$ and $L_2(\beta)$ (not appearing in eq. 11) are called the Barkas and Bloch correction factors respectively. The Barkas correction is meant to correct for failures of the Born approximation. Since the next factor in the Born expansion contains a term proportional to the cube of the incident particle's charge, charged pions and heavy ions deviate from the predictions of eq. 11. The Bloch correction factor originates from Bloch's analysis of Bohr's and Bethe's approach to the calculation of energy loss, and the attempt to marry the two theories. $L_2(\beta)$ has changed over the years to more of an empirical form [89], but remains part of the general LET equation. The final LET equation then takes the form shown in eq. 1.

It is important to note that the calculation of LET with equation 1 yields only an average value. Since the collisions are quantum mechanical in nature, there will exist a statistical variation in the actual energy transferred, and the number of collisions that take place. This variation is referred to as straggling. This is a more serious consideration for thin volumes, since the fluctuations in energy deposited are a greater percentage of the overall energy deposited. The origins have been investigated theoretically [86], however the accuracy of the theory over a wide range of thicknesses and energies is still a subject of continued research [85,90].

Accuracy of LET Theory

Many difficulties arise in the assessment of the accuracy of the LET theory. Experimental results for LET in bulk materials can differ between experiments by a few percent due to differences in the actual atomic structure of the materials. For thin materials and low energies, the nuclear stopping power can become significant [90], causing the LET to deviate from the Bethe-Bloch theory which ignores the nuclear

collisions.

Other aspects to consider are the semi-empirical corrections in the equation that are fitted for certain ions, materials, and energies and then extrapolated for others. However, it should be noted that the total contribution to the calculated LET from the Barkas and Bloch corrections for incident protons is less than 1% for all energies above 10 MeV and less than 0.1% for energies above 100 MeV, while at 1 MeV they are as high as 10% [32]. So for many high energy LET calculations, these corrections are minor. In fact, it has been seen that the Bethe-Bloch theory agrees with experimental data from 46 different papers to about 2% on average [32].

The validation and adjustment of the correction factors in the LET theory is an ongoing work, however the overall accuracy of the theory has been very good with an average agreement with experimental data of less than 5% [65].

APPENDIX B

MRED STANDARD MODE EXAMPLE CODE

This Appendix contains an example of Python code written to interface with MRED version 9.2.0 on ACCRE in the standard mode. The code simulates incident particles (protons by default) of a given energy (200 MeV by default) incident on the diodes described in section III. Certain lines of code were too long for the page width and were split to span two or more lines.

```
import base64
import cPickle
import sys
import os

#-----
# Option Parsing
#-----
from optparse import OptionParser

parser=OptionParser(usage="myScript [OPTIONS]")
parser.disable_interspersed_args()
# Options for run
parser.add_option("", "--suv", action='store_true', dest="enableSUV", default=False, help="Use the GEANT4 OpenGL viewer")
parser.add_option("", "--nIons", action='store', dest="nIons", type="int", default=100, help="The number of particles to run. Default=100")
parser.add_option("", "--particle", action='store', dest="particle", type="str", default="proton", help="Particle species. Default='proton' ")
parser.add_option("", "--beamE", action='store', dest="beamE", type="float", default=200.0, help="Beam energy (MeV). Default=200")
parser.add_option("", "--beamZ", action='store', dest="beamZ", type="int", default=1, help="Beam atomic number")
parser.add_option("", "--beamA", action='store', dest="beamA", type="int", default=1, help="Beam atomic weight")
parser.add_option("", "--runName", action='store', dest="runName", type="str", default="test", help="File name to save the hdf5 file. Default='test' ")
parser.add_option("", "--rangeCuts", action='store', dest="rangeCuts", type="float", default=100.0, help="Physics Range Cuts in micrometers. Default=100")
parser.add_option("", "--csMult", action='store', dest="csMult", type="float", default=400, help="Hadronic Cross Section Multiplier. Default 400")
parser.add_option("", "--histMin", action='store', dest="histMin", type="float", default=0, help="Minimum Energy for Histogram (MeV). Default=0")
parser.add_option("", "--histMax", action='store', dest="histMax", type="float", default=100, help="Maximum Energy for Histogram (MeV). Default=100")
parser.add_option("", "--histScale", action='store', dest="histScale", type="str", default='linear', help="Log or linear scale for histogram. Default=linear")
parser.add_option("", "--gunDir", action='store', dest="gunDir", type="int", default=0, help="Direction of incident beam in degrees. Default=0 (normal incidence)")
```

```

#Physics List Options
parser.add_option("", "--hadPhys", action='store', dest="hadPhys", type="str", default="CEM", help="Calls
a certain hadronic physics model. Options are: 'CEM', 'BinaryCascade', 'BertiniCascade', 'INCL_ABLA',
'G4QMD', 'JQMD' and 'PHITS'. Defaults to CEM, but goes to BertiniCascade if nothing else called.")

(options, args) = parser.parse_args(run_args[1:])

#-----
#   Define Physics
#-----

PyG4Core.ExecuteCommand('/control/verbose 2')
if mred.physics.list_name == 'PhysicsList':
# -----
# PenelopeQED is the default E&M model. Select one from the list.
#mred.physics.addModule('Standard')
mred.physics.addModule('StandardScreened')
#mred.physics.addModule('EmLowEnergyQED')
#mred.physics.addModule('EmPenelopeQED')
# -----
# These are for elementary particles. Normally use them all.
mred.physics.addModule('HadronElastic')
mred.physics.addModule('HadronInelastic')
mred.physics.addModule('PiKinElastic')
#-----
#   Hadronic Physics
#-----
if options.hadPhys=="PHITS":
    mred.physics.addModule('NucleonHadronicPHITS') # Experimental
elif options.hadPhys=="JQMD":
    mred.physics.addModule('NucleonHadronicJQMD') # Experimental
else:
    mred.physics.addModule('NucleonHadronic')
    if options.hadPhys=="CEM":
mred.physics.module_dict['NucleonHadronic'].SetUseCEM(True)
    else:
mred.physics.module_dict['NucleonHadronic'].SetUseCEM(False)
    if options.hadPhys=="BinaryCascade":
        mred.physics.module_dict['NucleonHadronic'].SetUseBinaryCascade(True)
    elif options.hadPhys=="G4QMD":
mred.physics.module_dict['NucleonHadronic'].SetProtonsUseQMD(True)
    elif options.hadPhys=="INCL_ABLA":
mred.physics.module_dict['NucleonHadronic'].SetUseInclAblaCascade(True)
#mred.physics.module_dict['NucleonHadronic'].SetInclAblaUseStrictEnergyLimit(True)
    else:
mred.physics.module_dict['NucleonHadronic'].SetUseBertiniCascade()
    if options.hadPhys != 'BertiniCascade': print "***Hadronic Physics not valid, using Bertini Cascade***"
mred.physics.module_dict['NucleonHadronic'].SetUseHPNNeutrons(True)
# -----
#   Ion Nuclear Physics
#-----
# 'AltIonInelastic' is the default ion-ion model
#
# The following are for using G4QMD
#mred.physics.addModule('IonInelasticG4QMD')
# The following can be used together to pick the FRAG model to replace GEM.
# This is a one-way choice. It is not possible to go back to GEM.
#mred.physics.module_dict['IonInelasticG4QMD'].GetG4QMDModel().UnUseGEM()
#mred.physics.module_dict['IonInelasticG4QMD'].GetG4QMDModel().UseFRAG()
#
mred.physics.addModule('IonInelastic')
#mred.physics.addModule('AltIonInelastic')
#mred.physics.addModule('IonInelasticJQMD')
#mred.physics.addModule('IonInelasticPHITS')
#mred.physics.addModule('IonInelasticLAQGSM')

```

```

#mred.physics.addModule('IonAbrasion')
#mred.physics.addModule('IonAbrasionEMD')
# -----
mred.physics.module_dict['Decay'].SetIncludeRadioactiveDecay(False)
# -----
# These can be used to turn on and set the threshold for Penelope transport.
#mred.physics.module_dict['StandardScreened'].SetUsePenelope(True)
#mred.physics.module_dict['StandardScreened'].SetPenelopeThreshold(50.*keV)
# -----
# These commands set up the cross section biasing wrapper. They will only have
# an effect on processes defined by Geant4 reference physics lists if those
# processes have been explicitly wrapped.
mred.physics.use_multiplier_primary_only=True
mred.physics.use_track_weighting=True
print "cross_section_wrapper_info = %s" % mred.physics.cross_section_wrapper_info

#-----
# Range Cuts
#-----
mred.physics.range_cuts = options.rangeCuts*1.0*um

#-----
# Cross Section Multiplier
#-----
mred.physics.hadronic_cross_section_multiplier = options.csMult

#-----
# Device Definition
#-----

import G4Support

# Enable the necessary materials in addition to Si
sio2=mred.materials.enableMaterial('SiO2')
w=mred.materials.enableMaterial('tungsten')
mred.materials.enableMaterial('TiSi2')
al=mred.materials.enableMaterial('aluminum')

# Create an instance of a RPP device
d=mred.setDevice('rpp')
d.wafer_material='silicon'

waferSize=((300.+100.)*um, (2*780.+30.+100.)*um, 57.36*um)

d.wafer_size=waferSize

d.first_layer_depth=0.0*um

d.wafer_z_offset=0.0*um

#-----
# M1Layer
#-----
box1=PyG4Core.G4Box("box1", 0.5*300.*um, 0.5*(2*780.+30.)*um, 0.5*1.3*um)
M1layer = G4Support.LogicalVolume(box1, material=sio2, name="M1layer")
nm="m1layer"
b = PyG4Core.G4Box(nm, 0.5*300.*um, 0.5*780.*um, 0.5*1.3*um)
lv = G4Support.LogicalVolume(b, material=al, name=nm, color=(1.,0.,0.))
G4Support.Placement(lv, name=nm, parent=M1layer, pos=(0.*um, 0.5*(780.+30.)*um, 0.*um))

#-----
# PlugLayer
#-----
box2=PyG4Core.G4Box("box2", 0.5*300.*um, 0.5*(2*780.+30.)*um, 0.5*0.5*um)
pluglayer = G4Support.LogicalVolume(box2, material=sio2, name="pluglayer")

```

```

for i in range(149):
    for j in range(287):
        nm = "plug[%d,%d]" % (i,j)
        b=PyG4Core.G4Box(nm, 0.25*um, 0.25*um, 0.25*um)
        lv=G4Support.LogicalVolume(b, material=w, name=nm, color=(1.,1.,1.))
        G4Support.Placement(lv, name=nm, parent=pluglayer, pos=(2.0*(i-74)*um, (2.7*(j-143)+0.5*(780+30))
            *um, 0.*um))

#-----
#   M2Layer
#-----
box3=PyG4Core.G4Box("box3", 0.5*300.*um, 0.5*(2*780.+30.)*um, 0.5*1.2*um)
M2layer = G4Support.LogicalVolume(box3, material=sio2, name="M2layer")
nm="m2layer"
b = PyG4Core.G4Box(nm, 0.5*300.*um, 0.5*780.*um, 0.5*1.2*um)
lv = G4Support.LogicalVolume(b, material=al, name=nm, color=(1.,0.,0.))
G4Support.Placement(lv, name=nm, parent=M2layer, pos=(0.*um, 0.5*(780.+30.)*um, 0.*um))

#-----
#   StripLayer
#-----
box4=PyG4Core.G4Box("box4", 0.5*300.*um, 0.5*(2*780.+30.)*um, 0.5*0.9*um)
striplayer = G4Support.LogicalVolume(box4, material=sio2, name="striplayer")
for i in range(286):
    for j in range(3):
        nm = "strip[%d]" % (3*i+j)
        b=PyG4Core.G4Box(nm, 0.5*300*um, 0.5*0.4*um, 0.5*0.9*um)
        lv=G4Support.LogicalVolume(b, material=w, name=nm, color=(1.,1.,1.))
        G4Support.Placement(lv, name=nm, parent=striplayer, pos=(0.0*um, (2.7*(i-143)+0.5*(780.+30.))*um
            + 0.9*j*um, 0.*um))
b=PyG4Core.G4Box("strip[%d]" % 3*286, 0.5*300*um, 0.5*0.4*um, 0.5*0.9*um)
nm = "strip[%d]" % 3*286
lv=G4Support.LogicalVolume(b, material=w, name=nm, color=(1.,1.,1.))
G4Support.Placement(lv, name=nm, parent=striplayer, pos=(0.0*um, (2.7*(286-143)+0.5*(780.+30.))*um,
0.*um))

#-----
#   Set Layers
#-----
d.setLayers([
((300.*um, (2*780.+30.)*um, 1.2*um), 'SiO2', ''),
mredPy.TargetLayerLV(M1layer),
mredPy.TargetLayerLV(pluglayer),
mredPy.TargetLayerLV(M2layer),
mredPy.TargetLayerLV(striplayer),
((300.*um, (2*780.+30.)*um, 0.04*um), 'TiSi2', ''),
((300.*um, (2*780.+30.)*um, 0.12*um), 'silicon', ''),
((300.*um, (2*780.+30.)*um, 2.1*um), 'silicon', 'dect'),
((300.*um, (2*780.+30.)*um, 50.0*um), 'silicon', '')
])

#-----
#   Sensitive Volumes
#-----
sd = mred.detector_dict['dect']

# Create one for diode with W overlayers
sv_W = sd.addSensitiveVolume()
sv_W.setSize((300.*um, 780.*um, 2.1*um))
sv_W.center = (0., 0.5*(780.+30.)*um, -22.37*um)
sv_W.weight=1.

# Create one for diode with no W overlayers
sv_noW = sd.addSensitiveVolume()
sv_noW.setSize((300.*um, 780.*um, 2.1*um))

```

```

sv_noW.center = (0., -0.5*(780.+30.)*um, -22.37*um)
sv_noW.weight=1.

d.register()

#-----
# Saving Histogram
#-----

mred.init()
mred.accumulate_histograms=True
mred.setDefaultHistogram(options.histMin*MeV, options.histMax*MeV, 2000, options.histScale)

myFilePath = '/home/clemenm1/SNL_Bulk_Diodes/hdf5_output/'

if batch_vars:
if os.path.exists(myFilePath + batch_vars.runName):
    print "\nOutput directory exists!"
    else:
        os.mkdir(myFilePath + batch_vars.runName)
        print "\nOutput directory CREATED!"
        mred.hdf5.file_path=str(myFilePath + batch_vars.runName)
        mred.hdf5.file_name=str(batch_vars.runName + "%03d.hdf5" % batch_vars.index)
else:
if os.path.exists(myFilePath + options.runName):
    print "\nOutput directory exists!"
    else:
        os.mkdir(myFilePath + options.runName)
        print "\nOutput directory CREATED!"
        mred.hdf5.file_path=str(myFilePath + options.runName)
        mred.hdf5.file_name=str(options.runName +'.hdf5')

mred.hdf5.include_energies=False
mred.hdf5.write_output_files=True
mred.hdf5.include_energies=False
mred.hdf5.include_hits=False
mred.hdf5.include_histograms=True
mred.hdf5.include_tracks=False

mred.gun.setParticle(options.particle)
mred.gun.energy=options.beamE*MeV

mred.gun.random_spatial_sampling='directionalFlux'
mred.gun.random_use_device_radius=False
mred.gun.random_box_size=waferSize

if options.gunDir==60:
    mred.gun.direction = (2,0,1)

if options.gunDir==85:
    mred.gun.direction = (11.43,0,1)

mred.progress_interval=options.nIons/100

if options.enableSUV:
    mred.suv()

mred.beamOn(options.nIons)

print "\nFluence Unit: ", mred.gun.fluence_unit
print "Beam Energy(MeV): ", options.beamE
print "Beam direction: ", options.gunDir
print "particle: ", options.particle
print "Hadronic Physics Model Selected: ", options.hadPhys
print "Hadronic Cross Section Multiplier: ", options.csMult

```

```
print "\n"
```

APPENDIX C

MRED SINGLE EVENT MODE EXAMPLE CODE

This Appendix contains an example of Python code written to interface with MRED version 9.2.0 on ACCRE in single event mode. The code simulates incident particles (neutrons by default) incident on a 32×32 bit 65 nm SRAM using nested sensitive volumes. The code records the weights SBU and MCU events to allow for cross section calculations. Certain lines of code were too long for the page width and were split to span two or more lines.

```
from PyG4Core import G4Colour as G4Color
import base64
import cPickle
import sys
import os

#-----
# Option Parsing
#-----
from optparse import OptionParser

parser=OptionParser(usage="myScript [OPTIONS]")
parser.disable_interspersed_args()
# Options for run
parser.add_option("", "--suv", action='store_true', dest="enableSUV", default=False, help="Use the GEANT4
OpenGL viewer")
parser.add_option("", "--nIons", action='store', dest="nIons", type="int", default=100, help="The number
of particles to run. Default=100")
parser.add_option("", "--particle", action='store', dest="particle", type="str", default="neutron", help=
"Particle species. Default='neutron' ")
parser.add_option("", "--nspectrum", action='store_true', dest="nspectrum", default=False, help=
"Use the LANL neutron spectrum")
parser.add_option("", "--jedecSpectrum", action='store_true', dest="jedecSpectrum", default=False, help=
"Use the JEDEC NYC neutron spectrum")
parser.add_option("", "--triumfBL2C", action='store_true', dest="triumfBL2C", default=False, help="Use
the TRIUMF BL2C (up to 200 MeV) neutron spectrum")
parser.add_option("", "--beamE", action='store', dest="beamE", type="float", default=14.0, help="Beam
energy (MeV). Default=14")
parser.add_option("", "--beamZ", action='store', dest="beamZ", type="int", default=1, help="Beam atomic
number")
parser.add_option("", "--beamA", action='store', dest="beamA", type="int", default=1, help="Beam atomic
weight")
parser.add_option("", "--runName", action='store', dest="runName", type="str", default="test", help="File
```

```

name to save the hdf5 file. Default='test' ")
parser.add_option("", "--rangeCuts", action='store', dest="rangeCuts", type="float", default=100.0, help=
"Physics Range Cuts in micrometers. Default=100")
parser.add_option("", "--csMult", action='store', dest="csMult", type="float", default=400, help="Hadronic
Cross Section Multiplier. Default 400")
parser.add_option("", "--gunDir", action='store', dest="gunDir", type="int", default=0, help="Direction of
incident beam in degrees. Default=0 (normal incidence)")
parser.add_option("", "--minE", action='store', dest="minE", type="float", default=1, help="Minimum Valid
total energy for each sd in keV. Default=1 keV")
parser.add_option("", "--numRows", action='store', dest="numRows", type="int", default=32, help="Number
of rows in the SRAM. Default=32")
parser.add_option("", "--numCols", action='store', dest="numCols", type="int", default=32, help="Number
of columns in the SRAM. Default=32")
parser.add_option("", "--tungsten", action='store_true', dest="tungsten", default=False, help="Puts a 0.3
um thick W layer over the cell layer")
parser.add_option("", "--qcrit", action='store', dest="qcrit", type="float", default=1.0, help="Qcrit for
Replay. Default 1.0 fC.")

#Physics List Options
parser.add_option("", "--hadPhys", action='store', dest="hadPhys", type="str", default="CEM", help="Calls
a certain hadronic physics model. Options are: 'CEM', 'BinaryCascade', 'BertiniCascade', 'INCL_ABLA',
'G4QMD', 'JQMD' and 'PHITS'. Defaults to CEM, but goes to BertiniCascade if nothing else called.")

#Replay Options
parser.add_option("", "--replaySeeds", action='store', dest="replaySeeds", type="str", default=None, help=
"Random Seeds for single replay")
parser.add_option("", "--replayPickle", action='store', dest="replayPickle", type="str", default=None, help=
"File name for pickled list of random seeds")

(options, args) = parser.parse_args(run_args[1:])

class Device:
    '''A class object representing a semiconductor device. A device consists of a name, critical energy,
and a group of sensitive volumes. Each device maintains indices into an MRED sensitive volume list
and its own energy deposition histogram. Although the device has an Ecrit, it does not filter events
in the histogram. The entire energy deposition distribution is available for the user. The Ecrit is
only used to determine a coincident upset.'''
    def __init__(self, name=None):
        self.name=name
        self.Ecrit=0.0
        self.sd=None
        self.group=None
        self.sv_idx_vector=[]

#-----
# Define Physics
#-----

PyG4Core.ExecuteCommand('/control/verbose 2')
if mred.physics.list_name == 'PhysicsList':
# -----
# PenelopeQED is the default E&M model. Select one from the list.
#mred.physics.addModule('Standard')
mred.physics.addModule('EmStandardScreened')
#mred.physics.addModule('EmLowEnergyQED')
#mred.physics.addModule('EmPenelopeQED')
# -----
# These are for elementary particles. Normally use them all.
mred.physics.addModule('HadronElastic')
mred.physics.addModule('HadronInelastic')
mred.physics.addModule('PiKinElastic')
#-----
# Hadronic Physics
#-----
if options.hadPhys=="PHITS":

```

```

mred.physics.addModule('NucleonHadronicPHITS') # Experimental
elif options.hadPhys=="JQMD":
mred.physics.addModule('NucleonHadronicJQMD') # Experimental
else:
mred.physics.addModule('NucleonHadronic')
if options.hadPhys=="CEM":
mred.physics.module_dict['NucleonHadronic'].SetUseCEM(True)
else:
mred.physics.module_dict['NucleonHadronic'].SetUseCEM(False)
if options.hadPhys=="BinaryCascade":
    mred.physics.module_dict['NucleonHadronic'].SetUseBinaryCascade(True)
elif options.hadPhys=="G4QMD":
mred.physics.module_dict['NucleonHadronic'].SetProtonsUseQMD(True)
elif options.hadPhys=="INCL_ABLA":
mred.physics.module_dict['NucleonHadronic'].SetUseInclAblaCascade(True)
#mred.physics.module_dict['NucleonHadronic'].SetInclAblaUseStrictEnergyLimit(True)
else:
mred.physics.module_dict['NucleonHadronic'].SetUseBertiniCascade()
if options.hadPhys != 'BertiniCascade': print "***Hadronic Physics not valid, using Bertini Cascade***"
mred.physics.module_dict['NucleonHadronic'].SetUseHPNNeutrons(True)
# -----
# Ion Nuclear Physics
#-----
# 'AltIonInelastic' is the default ion-ion model
#
# The following are for using G4QMD
#mred.physics.addModule('IonInelasticG4QMD')
# The following can be used together to pick the FRAG model to replace GEM.
# This is a one-way choice. It is not possible to go back to GEM.
#mred.physics.module_dict['IonInelasticG4QMD'].GetG4QMDModel().UnUseGEM()
#mred.physics.module_dict['IonInelasticG4QMD'].GetG4QMDModel().UseFRAG()
#
mred.physics.addModule('IonInelastic')
#mred.physics.addModule('AltIonInelastic')
#mred.physics.addModule('IonInelasticJQMD')
#mred.physics.addModule('IonInelasticPHITS')
#mred.physics.addModule('IonInelasticLAQGSM')
#mred.physics.addModule('IonAbrasion')
#mred.physics.addModule('IonAbrasionEMD')
# -----
mred.physics.module_dict['Decay'].SetIncludeRadioactiveDecay(False)
# -----
# These can be used to turn on and set the threshold for Penelope transport.
#mred.physics.module_dict['StandardScreened'].SetUsePenelope(True)
#mred.physics.module_dict['StandardScreened'].SetPenelopeThreshold(50.*keV)
# -----
# These commands set up the cross section biasing wrapper. They will only have
# an effect on processes defined by Geant4 reference physics lists if those
# processes have been explicitly wrapped.
mred.physics.use_multiplier_primary_only=True
mred.physics.use_track_weighting=True
print "cross_section_wrapper_info = %s" % mred.physics.cross_section_wrapper_info

#-----
# Range Cuts
#-----
mred.physics.range_cuts = options.rangeCuts*1.0*um

#-----
# Cross Section Multiplier
#-----
mred.physics.hadronic_cross_section_multiplier = options.csMult

#####
# Create a layered device

```

```

#####
d=mred.setDevice('rpp')
mred.materials.enableBasicElectronicMaterials()
mred.materials.enableMaterial('air')

if options.tungsten: mred.materials.enableMaterial('tungsten')

# Create the layered device for an array of devices. This stack is created to
# include extra material around the array. Because of this, the sensitive
# detector is not the entire width of the silicon layer. I have also omitted
# the oxide material for STI instead lumping it into the silicon layer. This
# will hopefully avoid the boundary stepping problem with energy deposition
# seen in other simulations.

# A list of semiconductor devices
deviceList=[]

layers = []
nCols=options.numCols
nRows=options.numRows
scalingParameter=1

margin=20.0
substrateDepth=10
cellWidth=0.975*scalingParameter
cellLength=0.475*scalingParameter
layerWidth=(nCols * cellWidth + margin) * micrometer
layerLength=(nRows * cellLength + margin) * micrometer
print "Cell Size %g x %g" % ( cellWidth, cellLength )

#A solid block of Si with a W layer next to the sensitive volumes.
if options.tungsten:
layers.append(((layerWidth, layerLength, 4.19*micrometer), 'silicon'))
layers.append(((layerWidth, layerLength, 0.3*micrometer), 'tungsten'))
else:
layers.append(((layerWidth, layerLength, 4.49*micrometer), 'silicon'))

layers.append(((nCols * cellWidth*micrometer, nRows * cellLength*micrometer, 5.0*micrometer), 'silicon',
'default'))
layers.append(((layerWidth, layerLength, substrateDepth*micrometer), 'silicon'))
d.setLayers(layers)
d.wafer_material='silicon'

mred.device.register(d.g4PV())
mred.init()

sd = mred.sd_vector[0]
print "Configuring sensitive detector %s" % ( sd.name )
mred.runAct.SetAutoGenerateHistogramsFlag(False)
mred.accumulate_histograms=False

# Create each device as a group of associated sensitive volumes
zoffset=(d.wafer_dimensions[2]/um / 2.0) - (substrateDepth+5.0)

# According to Jeff Black, the columns are divided into 16 groups of 32.
# Each of bit in a 16-bit word is then separated by 32 columns. If a
# checkerboard pattern is written to the array, there will be blocks of
# 0's and 1's. In that sense, we are always simulated all 0's or all 1's.
# Also, although the cells are mirrored, the sense amp polarities run the same
# way therefore assume that a logic 0 results in a sensitive volume on the
# left of the cell and a logic 1 results in a sensitive volume on the right.
# Finally, assume that the block cells being simulated are the least
# significant bit.
nwellWidth=0.368*scalingParameter
pwellWidth=0.607*scalingParameter

```

```

pattern=int('0xAAAA',16)
for row in range(nRows):
    for col in range(nCols):
        device=Device('r%d_c%d' % (row, col))
        device.group=sd.addSensitiveVolume('group')
        device.group.on=True
        device.group.weight=1
        device.Ecrit=device.group.min_valid_total_energy=0.*keV

        data=pattern&1
        evenRow=bool(row%2)
        evenCol=bool(col%2)
        # Calculate the extremes of the cell
        cellXmin = (col*cellWidth) - (nCols*cellWidth)/2.0
        cellXcenter = (col*cellWidth) - (nCols*cellWidth)/2.0 + cellWidth/2.0
        cellXmax = (col*cellWidth) - (nCols*cellWidth)/2.0 + cellWidth
        cellYmin = (row*cellLength) - (nRows*cellLength)/2.0
        cellYcenter = (row*cellLength) - (nRows*cellLength)/2.0 + cellLength/2.0
        cellYmax = (row*cellLength) - (nRows*cellLength)/2.0 + cellLength
        # Calculated the center of the sensitive volume based on data, column,
        # and row.
        if data == 0:
            xoffset = cellXmin + 0.15*scalingParameter
        else:
            xoffset = cellXmax - 0.15*scalingParameter
        if evenRow:
            yoffset = cellYmax - 0.237*scalingParameter # 0.2
        else:
            yoffset = cellYmin + 0.237*scalingParameter

        depth = 0.450*scalingParameter
        # Calibrated for TAMU N LET = 0.6 ~ 550 MeV
        sv=device.group.add('rpp')
        sv.setCenter(vector3d(xoffset,yoffset,zoffset+depth/2.0)*micrometer)
        sv.setSize(vector3d(0.110*scalingParameter,0.140*scalingParameter,depth*scalingParameter)*
micrometer)
        sv.on=True
        sv.weight=0.75 # 0.70
        sv.cpp_sv.SetDisplayColour(PyG4Core.G4Colour(0,1,0,min(1,sv.weight)))

        # Calibrated for LBNL B LET = 0.89 ~ 105 MeV
        sv=device.group.add('rpp')
        sv.setCenter(vector3d(xoffset,yoffset,zoffset+depth/2.0)*micrometer)
        sv.setSize(vector3d(0.110*scalingParameter,0.180*scalingParameter,depth)*micrometer)
        sv.on=True
        sv.weight=0.23 # 0.23
        sv.cpp_sv.SetDisplayColour(PyG4Core.G4Colour(0,1,0,min(1,sv.weight)))

        # Calibrated for TAMU Ne LET = 2.8 ~ 250 MeV
        sv=device.group.add('rpp')
        sv.setCenter(vector3d(xoffset,cellYcenter,zoffset+depth/2.0)*micrometer)
        sv.setSize(vector3d(0.11*scalingParameter,cellLength+0.1,depth)*micrometer)
        sv.on=True
        sv.weight=0.07 # 0.07
        sv.cpp_sv.SetDisplayColour(PyG4Core.G4Colour(0,1,0,min(1,sv.weight)))

        # Guess for PMOS
        sv=device.group.add('rpp')
        sv.setCenter(vector3d(cellXcenter,cellYcenter,zoffset+depth/2.0)*micrometer)
        sv.setSize(vector3d(0.088*scalingParameter,cellLength,depth)*micrometer)
        sv.on=True
        sv.weight=0.07 # 0.07
        sv.cpp_sv.SetDisplayColour(PyG4Core.G4Colour(0,1,0,min(1,sv.weight)))

```

```

# Pwell
# 1um at 0.07 give FIT ~240, but ion is 4e-9, or 0.75um at 0.09, or 0.6 at 0.116
depth2=0.475*scalingParameter
sv=device.group.add('rpp')
if data == 0:
    sv.setCenter(vector3d(cellXmin+0.05,cellYcenter,zoffset+depth+depth2/2.0)*micrometer)
else:
    sv.setCenter(vector3d(cellXmax-0.05,cellYcenter,zoffset+depth+depth2/2.0)*micrometer)
sv.setSize(vector3d(pwellWidth-0.1,cellLength,depth2)*micrometer) # 0.2
sv.on=True
sv.weight=0.07 # 0.10 7 0.02
sv.cpp_sv.SetDisplayColour(PyG4Core.G4Colour(0,1,0,min(1,sv.weight)))

# Nwell
# 1um at 0.07 give FIT ~240, but ion is 4e-9, or 0.75um at 0.09, or 0.6 at 0.116
depth2=0.475*scalingParameter
sv=device.group.add('rpp')
sv.setCenter(vector3d(cellXcenter,cellYcenter,zoffset+depth+depth2/2.0)*micrometer)
sv.setSize(vector3d(nwellWidth,cellLength,depth2)*micrometer) # 0.2
sv.on=True
sv.weight=0.07 # 0.10 7 0.02
sv.cpp_sv.SetDisplayColour(PyG4Core.G4Colour(0,1,0,min(1,sv.weight)))

depth3=0.5*scalingParameter
sv=device.group.add('rpp')
sv.setCenter(vector3d(cellXcenter,cellYcenter,zoffset+depth+depth2+depth3/2.0)*micrometer)
sv.setSize(vector3d(cellWidth,cellLength,depth3)*micrometer) # 0.2
sv.on=True
sv.weight=0.02 # 0.10 7
sv.cpp_sv.SetDisplayColour(PyG4Core.G4Colour(0,1,0,min(1,sv.weight)))

deviceList.append(device)

# This is really only enabled for efficiency. We don't want to enter the single
# event callback for every particle, so putting a small, but meaningful filter
# here will help a lot. If the model has been calibrated, this should be set
# just below the critical energy.
sd.use_weighted_as_total=True
sd.min_valid_total_energy=options.minE*keV

#-----
# Saving File
#-----

myFilePath = '/home/clemen1/MBU/Output/'

if batch_vars:
if os.path.exists(myFilePath + batch_vars.runName):
    print "\nOutput directory exists!"
    else:
        os.mkdir(myFilePath + batch_vars.runName)
        print "\nOutput directory CREATED!"
file_name=str(myFilePath + batch_vars.runName + "/" + batch_vars.runName + "%03d.pickle" %
batch_vars.index)
text_file_name=str(myFilePath + batch_vars.runName + "/" + batch_vars.runName + "%03d.txt" %
batch_vars.index)
else:
    if os.path.exists(myFilePath + options.runName):
        print "\nOutput directory exists!"
    else:
        os.mkdir(myFilePath + options.runName)
        print "\nOutput directory CREATED!"
        file_name=str(myFilePath + options.runName + "/" + options.runName + ".pickle")
        text_file_name=str(myFilePath + options.runName + "/" + options.runName + ".txt")

```

```

#-----
# SCU & MCU processing variables
#-----

global SCU_sum, MCU2_sum, MCU3_sum, MCU4_sum, MCU5_sum, MCU6p_sum
global SCU_num, MCU2_num, MCU3_num, MCU4_num, MCU5_num, MCU6p_num, SCU_x
listSize = int((50-0)/0.1)
SCU_sum = [0]*listSize; MCU2_sum = [0]*listSize; MCU3_sum = [0]*listSize; MCU4_sum = [0]*listSize;
MCU5_sum = [0]*listSize; MCU6p_sum = [0]*listSize
SCU_num = [0]*listSize; MCU2_num = [0]*listSize; MCU3_num = [0]*listSize; MCU4_num = [0]*listSize;
MCU5_num = [0]*listSize; MCU6p_num = [0]*listSize
SCU_x = [0]*listSize

#-----
# Particle beam
#-----

mred.gun.random_energy_sampling='uniform'
mred.gun.random_spatial_sampling='directionalFlux'
mred.gun.random_use_device_radius=False

if options.nspectrum:
#measured neutron flux at LANSCE
mred.gun.setEnergySpectrumFile('/usr/local/radefects/data/environments/LANL_neutrons/nLANLENormand.dat')
elif options.jedecSpectrum:
mred.gun.setEnergySpectrumFile('/usr/local/radefects/data/environments/NYC_neutrons/NYC_neutron_flux.dat')
elif options.triumfBL2C:
#FLUKA calculation of neutron flux in BL2C beamline
mred.gun.setEnergySpectrumFile('/home/clemenm1/local/TRIUMF_BL2C_nFlux.dat')
else:
mred.gun.energy=options.beamE*MeV

mred.gun.setParticle(options.particle)

mred.gun.random_box_size=d.wafer_dimensions

if options.gunDir==60:
mred.gun.direction = (2,0,1)
elif options.gunDir==85:
mred.gun.direction = (11.43,0,1)
else:
mred.gun.direction = (0,0,1)

mred.progress_interval=options.nIons/100
#mred.include_particles="True"

if options.enableSUV:
mred.suv()

#####
## Write File Headers
#####

if options.replayPickle:
pickOutFile = options.replayPickle + "_replayedEvents.txt"
FILE = open(pickOutFile, 'w')
else:
FILE = open(text_file_name, 'w')
#FILE.write("For each event - Random Seeds, SV index and Charge collected above 1 keV in a %i x %i SV
matrix with 65nm SV dim:\n" % (nCols, nRows) )

def singleEventCallback(evt):
    #I want to save:

```

```

# 1. all the charge coll events with the index of the SV.
# 2. the random seeds for each event
# 3. weight (variance is weight^2 so no need to record it)
# 4. the processed data - pickle file

global deviceList, SCU_sum, MCU2_sum, MCU3_sum, MCU4_sum, MCU5_sum, MCU6p_sum, SCU_num, MCU2_num,
MCU3_num, MCU4_num, MCU5_num, MCU6p_num

randomSeeds=mred.last_random_seeds
weight = mred.evtAct.ComputeEventWeight(evt)

if (options.replaySeeds or options.replayPickle):
    myTrackDict = mred.evtAct.get_track_dict(evt)

    for i in range(1,len(myTrackDict) + 1):
        particle_name = myTrackDict[i].GetParticleName()
        initial_kinetic_energy = myTrackDict[i].GetInitialKineticEnergy()
        LET = mred.LET(particle_name, 'silicon', initial_kinetic_energy)
        angle = math.degrees(myTrackDict[i].GetInitialMomentumDirection().getTheta())
        if LET > 0.5:
            if options.replayPickle:
                if (angle > 30):
                    FILE.write("\nNeutron E: %0.1f, Particle: %s, Energy:
                    %0.1f, LET: %0.2f, angle: %0.1f "
                    %(myTrackDict[1].GetInitialKineticEnergy(),
                    particle_name, initial_kinetic_energy, LET, angle))
                else:
                    print "Particle #i: %s, angle: %0.1f, Energy: %0.1f,
                    LET: %0.2f" %(i, particle_name, angle,
                    initial_kinetic_energy, LET)

            sys.stdout.flush()

Qs=[0]*len(deviceList)
aboveCharge=0
for i in range(len(deviceList)):
    Qs[i] = deviceList[i].group.total_energy/0.0225
    if Qs[i] > 0.04: # 1 keV
        if options.replaySeeds:
            # print SV index with charge collected
            print "(%i, %.2f)," % (i,Qs[i])
        else:
            # write SV index with charge collected
            FILE.write("(%i, %.2f)," % (i,Qs[i]))
        aboveCharge+=1

if aboveCharge>0:
    myTrackDict = mred.evtAct.get_track_dict(evt)
    nEnergy = initial_kinetic_energy = myTrackDict[1].GetInitialKineticEnergy()
    if options.replaySeeds:
        print "Random Seeds: (%d, %d), weight: %0.2e, En: %0.2f" %(randomSeeds[0],
        randomSeeds[1], weight, nEnergy)
    else:
        #write random seeds and weight and neutron Energy
        FILE.write("(%d, %d),%0.2e,E%0.2e\n" % (randomSeeds[0], randomSeeds[1],
        weight, nEnergy))

qi=0
qf=50
qstep=0.1
qloops=int((qf-qi)/qstep)

for j in xrange(qloops):
    good=0
    qcrit=j*qstep+qi
    for i in range(len(deviceList)):

```

```

        if(Qs[i] > qcrit):
            good += 1
    SCU_x[j] = qcrit

    if(good == 1):
        SCU_sum[j] += weight
        SCU_num[j] += 1
    elif(good == 2):
        MCU2_sum[j] += weight
        MCU2_num[j] += 1
    elif(good == 3):
        MCU3_sum[j] += weight
        MCU3_num[j] += 1
    elif(good == 4):
        MCU4_sum[j] += weight
        MCU4_num[j] += 1
    elif(good == 5):
        MCU5_sum[j] += weight
        MCU5_num[j] += 1
    elif(good > 5):
        MCU6p_sum[j] += weight
        MCU6p_num[j] += 1

    sys.stdout.flush()

#####
# Filters
#####
if options.particle == "neutron":
    mred.filter.on=True
    mred.filter.verbose=False
    mred.filter.include_particles=True
    mred.filter.include_scatters=True
    mred.filter.include_nuclear_elastic=True
    mred.filter.include_coulomb_elastic=True

if options.replaySeeds:
    print "Replaying event %s" % (options.replaySeeds)
    mred.random_seeds=eval(options.replaySeeds)
    mred.runSingleEventMode(1,function=singleEventCallback)
elif options.replayPickle:
    print "Replaying seeds from file: %s" %(options.replayPickle)
    ofileName = options.replayPickle + ".pickle"
    ofile = open(ofileName, 'r')
    pickleSeeds=cPickle.load(ofile)
    ofile.close()
    for i in range(len(pickleSeeds)):
        nextSeeds=(pickleSeeds[i][0], pickleSeeds[i][1])
        mred.random_seeds=nextSeeds
        mred.runSingleEventMode(1, function=singleEventCallback)
else:
    mred.runSingleEventMode(options.nIons,function=singleEventCallback)

FILE.close()

print "\nFluence Unit: ", mred.gun.fluence_unit
if options.nspectrum:
    print "LANL neutron spectrum used"
    print "Spectrum Integral: ", mred.gun.energy_spectrum.spectrum.integral()
elif options.jedecSpectrum:
    print "JEDEC NYC neutron spectrum used"
    print "Spectrum Integral: ", mred.gun.energy_spectrum.spectrum.integral()
elif options.triumfBL2C:
    print "TRIUMF BL2C neutron spectrum used"
    print "Spectrum Integral: ", mred.gun.energy_spectrum.spectrum.integral()

```

```

else:
    print "Beam Energy(MeV): ", options.beamE
    print "Beam direction: ", options.gunDir
    print "particle: ", options.particle
    print "Hadronic Physics Model Selected: ", options.hadPhys
    print "Hadronic Cross Section Multiplier: ", options.csMult
    print "\n"

q=int(options.qcrit*10)
print "SCU_sum: ", SCU_sum[q], "SCU_num: ", SCU_num[q]
print "2CU_sum: ", MCU2_sum[q], "MCU2_num: ", MCU2_num[q]
print "3CU_sum: ", MCU3_sum[q], "MCU3_num: ", MCU3_num[q]
print "4CU_sum: ", MCU4_sum[q], "MCU4_num: ", MCU4_num[q]
print "5CU_sum: ", MCU5_sum[q], "MCU5_num: ", MCU5_num[q]
print "6pCU_sum: ", MCU6p_sum[q], "MCU6p_num: ", MCU6p_num[q]

data = {"SCU_sum": SCU_sum, "SCU_num": SCU_num,
        "MCU2_sum": MCU2_sum, "MCU2_num": MCU2_num,
        "MCU3_sum": MCU3_sum, "MCU3_num": MCU3_num,
        "MCU4_sum": MCU4_sum, "MCU4_num": MCU4_num,
        "MCU5_sum": MCU5_sum, "MCU5_num": MCU5_num,
        "MCU6p_sum": MCU6p_sum, "MCU6p_num": MCU6p_num,
        "SCU_x": SCU_x}

pickleFile=open(file_name, 'w')
cPickle.dump(data, pickleFile)
pickleFile.close()

```

BIBLIOGRAPHY

- [1] G. E. Moore, "Cramming more components onto integrated circuits," *Electronics*, vol. 38, Apr 1965.
- [2] J. Wallmark and S. Marcus, "Minimum size and maximum packing density of nonredundant semiconductor devices," *Proc. of the IRE*, vol. 50, pp. 286–298, 1962.
- [3] D. Binder, E. Smith, and A. Holman, "Satellite anomalies from galactic cosmic ions," *IEEE Trans. on Nucl. Sci.*, vol. NS-22, no. 6, pp. 2675–2680, 1975.
- [4] T. May and M. Woods, "Alpha-particle-induced soft errors in dynamic memories," *IEEE Trans. on Elec. Dev.*, vol. ED-26, no. 1, pp. 2–9, 1979.
- [5] C. Howe, R. Weller, R. Reed, M. Mendenhall, R. Schrimpf, K. Warren, D. Ball, L. Massengill, K. LaBel, J. Howard, and N. Haddad, "Role of heavy-ion nuclear reactions in determining on-orbit single event error rates," *Nuclear Science, IEEE Transactions on*, vol. 52, pp. 2182–2188, Dec 2005.
- [6] J. Schwank, M. Shaneyfelt, J. Baggio, P. Dodd, J. Felix, V. Ferlet-Cavrois, P. Paillet, D. Lambert, F. Sexton, G. Hash, and E. Blackmore, "Effects of particle energy on proton-induced single-event latchup," *Nuclear Science, IEEE Transactions on*, vol. 52, pp. 2622–2629, Dec 2005.
- [7] P. Goldhagen, J. M. Clem, and J. Wilson, "The energy spectrum of cosmic-ray induced neutrons measured on an airplane over a wide range of altitude and latitude," *Radiation Protection Dosimetry*, vol. 110, pp. 387–392, Aug 2004.
- [8] E. Normand, "Single event upset at ground level," *IEEE Trans. Nucl. Sci.*, vol. 43, pp. 2742–2750, Dec 1996.
- [9] J. Baggio, V. Ferlet-Cavrois, and D. Lambert, "Neutron and proton-induced single event upsets in advanced commercial fully depleted soi srams," *Nuclear Science*, Jan 2006.
- [10] S. P. Platt, A. V. Prokofiev, and C. X. Xiao, "Fidelity of energy spectra at neutron facilities for single-event effects testing," *IEEE Inter. Rel. Phys. Symp.*, pp. 411–415, May 2010.
- [11] C. Dyer, A. Hands, K. Ford, A. Frydland, and P. Truscott, "Neutron-induced single event effects testing across a wide range of energies and facilities and implications for standards," *IEEE Trans. Nucl. Sci.*, vol. 53, pp. 3596–3601, Dec 2006.

- [12] E. Normand and L. Dominik, “Cross comparison guide for results of neutron see testing of microelectronics applicable to avionics,” *Radiation Effects Data Workshop (REDW), 2010 IEEE*, p. 8, 2010.
- [13] M. Martone, M. Angelone, and M. Pillon, “The 14 mev frascati neutron generator,” *J. Nucl. Mat.*, pp. 1661–1664, Jan 1994.
- [14] M. A. Clemens, N. C. Hooten, V. Ramachandran, N. A. Dodds, R. A. Weller, M. H. Mendenhall, R. A. Reed, P. E. Dodd, M. R. Shaneyfelt, J. R. Schwank, and E. W. Blackmore, “The effect of high-z materials on proton-induced charge collection,” *IEEE Trans. Nucl. Sci.*, vol. 57, pp. 3212–3218, Dec 2010.
- [15] M. Clemens, B. Sierawski, K. Warren, M. Mendenhall, N. Dodds, R. Weller, R. Reed, P. Dodd, M. Shaneyfelt, J. Schwank, S. Wender, and R. Baumann, “The effects of neutron energy and high-z materials on single event upsets and multiple cell upsets,” *IEEE Trans. Nucl. Sci.*, vol. 58, no. 6, pp. 2591 – 2598, 2011.
- [16] J. Barth, C. Dyer, and E. Stassinopoulos, “Space, atmospheric, and terrestrial radiation environments,” *Nuclear Science, IEEE Transactions on*, vol. 50, pp. 466 – 482, Jun 2003.
- [17] F. W. Sexton, “Measurement of single event phenomena in devices and ics,” *IEEE NSREC Short Course, New Orleans, LA*, 1992.
- [18] E. G. Stassinopoulos, “Microelectronics for the natural radiation environments of space,” *IEEE NSREC Short Course*, 1990.
- [19] J. L. Barth, “Applying computer simulation tools to radiation effects problem,” *IEEE NSREC Short Course*, 1997.
- [20] C. S. Dyer, “Radiation effects in the new millennium—old realities and new issues,” *IEEE NSREC Short Course*, 1998.
- [21] J. Mazur, “Radiation effects—from particles to payloads,” *IEEE NSREC Short Course*, 2002.
- [22] J. F. Ziegler, “Terrestrial cosmic rays,” *IBM J. Res. Development*, vol. 40, no. 1, pp. 19–39, 1996.
- [23] “Creme96: Cosmic ray effects on micro electronics website (1997). [online]. currently available at <https://creme.isde.vanderbilt.edu/>.”
- [24] “Measurement and reporting of alpha particle and terrestrial cosmic ray-induced soft errors in semiconductor devices,” *JEDEC Standard - JESD89A*, Oct 2006.
- [25] H. Barnaby, “Total-ionizing-dose effects in modern cmos technologies,” *IEEE Trans. Nucl. Sci.*, vol. 53, pp. 3103–3121, Jan 2006.

- [26] J. Srour, C. J. Marshall, and P. W. Marshall, "Review of displacement damage effects in silicon devices," *IEEE Trans. Nucl. Sci.*, vol. 50, pp. 653–670, Jan 2003.
- [27] P. E. Dodd and L. W. Massengill, "Basic mechanisms and modeling of single-event upset in digital microelectronics," *IEEE Trans. Nucl. Sci.*, vol. 50, pp. 583–602, Jan 2003.
- [28] T. Holman, "Radiation hardening techniques for analog and mixed-signal integrated circuits." From EECE 304 class lecture, 2008.
- [29] R. Baumann, "The impact of technology scaling on soft error rate performance and limits to the efficacy of error correction," *Proc. Int. Electron Device Meeting*, pp. 329–332, 2002.
- [30] R. L. Pease, "Total-dose issues for microelectronics in space systems," *IEEE Trans. Nucl. Sci.*, vol. 43, no. 2, pp. 442–452, 1996.
- [31] A. R. Frederickson, "Upsets related to spacecraft charging," *IEEE Trans. Nucl. Sci.*, vol. 43, no. 2, pp. 426–441, 1996.
- [32] J. Ziegler, "Stopping of energetic light ions in elemental matter," *Journal of Applied Physics*, Jan 1999.
- [33] W. Shockley, "Problems related to p-n junctions in silicon," *Solid State Electron*, vol. 2, pp. 35–67, 1961.
- [34] N. Dodds, R. Reed, M. Mendenhall, R. Weller, M. Clemens, P. Dodd, M. Shaneyfelt, G. Vizkelethy, J. Schwank, V. Ferlet-Cavrois, J. Adams, R. Schrimpf, and M. King, "Charge generation by secondary particles from nuclear reactions in beol materials," *IEEE Trans. Nucl. Sci.*, vol. 56, pp. 3172 – 3179, Dec 2009.
- [35] L. Massengill, "Practical considerations in applying electronics to space systems," *IEEE NSREC Short Course*, 1992.
- [36] K. Warren, "Sensitive volume models for single event upset analysis and rate prediction for space, atmospheric, and terrestrial radiation environments," *Ph.D. Dissertation*, Jun 2010.
- [37] R. Lacoë, "Radiation effects in advanced commercial technologies: How device scaling has affected the selection of spaceborne electronics," *IEEE NSREC Short Course*, 2003.
- [38] P. Dodd, "Radiation effects in the space telecom environment: Ii. basic mechanisms for single-event effects," *IEEE NSREC Short Course*, 1999.

- [39] M. McMahan, “The berkeley accelerator space effects (base) facility – a new mission for the 88-inch cyclotron at lbl,” *Nuclear Instruments and Methods in Physics Research B*, vol. 241, pp. 409–413, Nov 2005.
- [40] “<http://cyclotron.tamu.edu/>.”
- [41] C. C. Foster, S. L. Casey, A. L. Johnson, P. Miesle, N. Sifri, A. H. Skees, and K. M. Murray, “Opportunities for single event and other radiation effects testing and research at the indiana university cyclotron facility,” *IEEE Radiation Effects Data Workshop*, pp. 84–87, Mar 1996.
- [42] “Test procedures for the measurement of single-event effects in semiconductor devices from heavy ion irradiation,” *JESD57*, Oct 1996.
- [43] R. A. Weller, M. H. Mendenhall, R. A. Reed, R. D. Schrimpf, K. M. Warren, B. D. Sierawski, and L. W. Massengill, “Monte carlo simulation of single event effects,” *IEEE Trans. Nucl. Sci.*, vol. 57, pp. 1726–1746, Aug 2010.
- [44] S. Buchner, J. Langworthy, W. Stapor, A. B. Campbell, and S. Rivet, “Implications of the spatial dependence of the single-event-upset threshold in srams measured with a pulsed laser,” *IEEE Trans. Nucl. Sci.*, vol. 41, no. 6, pp. 2195 – 2202, 1994.
- [45] K. Warren, L. Massengill, R. Schrimpf, and H. Barnaby, “Analysis of the influence of mos device geometry on predicted seu cross sections,” *IEEE Trans. Nucl. Sci.*, vol. 46, no. 6, pp. 1363 – 1369, 1999.
- [46] B. Sierawski, J. Pellish, R. Reed, R. Schrimpf, K. Warren, R. Weller, M. Mendenhall, J. Black, A. Tipton, M. Xapsos, R. Baumann, X. Deng, M. Campola, M. Friendlich, H. Kim, A. Phan, and C. Seidleck, “Impact of low-energy proton induced upsets on test methods and rate predictions,” *IEEE Trans. Nucl. Sci.*, vol. 56, no. 6, pp. 3085 – 3092, 2009.
- [47] B. D. Sierawski, K. M. Warren, R. A. Reed, R. A. Weller, M. M. Mendenhall, R. D. Schrimpf, R. C. Baumann, and V. Zhu, “Contribution of low-energy (10 mev) neutrons to upset rate in a 65 nm sram,” *IEEE Inter. Rel. Phys. Symp.*, pp. 395 – 399, 2010.
- [48] N. Seifert, B. Gill, and K. Foley. . . , “Multi-cell upset probabilities of 45nm high-k+ metal gate sram devices in terrestrial and space environments,” *IEEE International Reliability Physics Symposium (IRPS)*, Jan 2008.
- [49] A. Tipton, J. Pellish, R. Reed, R. Schrimpf, R. Weller, M. Mendenhall, B. Sierawski, A. Sutton, R. Diestelhorst, G. Espinel, J. Cressler, P. Marshall, and G. Vizkelethy, “Multiple-bit upset in 130 nm cmos technology,” *IEEE Trans. Nucl. Sci.*, vol. 53, no. 6, pp. 3259 – 3264, 2006.

- [50] A. Kobayashi, D. Ball, K. Warren, R. Reed, N. Haddad, M. Mendenhall, R. Schrimpf, and R. Weller, “The effect of metallization layers on single event susceptibility,” *Nuclear Science, IEEE Transactions on*, vol. 52, no. 6, pp. 2189–2193, 2005.
- [51] R. A. Reed, R. A. Weller, R. D. Schrimpf, M. H. Mendenhall, K. M. Warren, and L. W. Massengill, “Implications of nuclear reactions for single event effects test methods and analysis,” *IEEE Trans. Nucl. Sci.*, vol. 53, pp. 3356–3362, Dec 2006.
- [52] P. J. McNulty, G. E. Farrell, and W. P. Tucker, “Proton-induced nuclear reactions in silicon,” *Nuclear Science, IEEE Transactions on*, vol. 28, pp. 4007–4012, Dec 1981.
- [53] P. J. McNulty, “Microelectronics for the natural radiation environments of space,” *IEEE NSREC Short Course*, 1990.
- [54] R. Reed, R. Weller, M. Mendenhall, J.-M. Lauenstein, K. Warren, J. Pellish, R. Schrimpf, B. Sierawski, L. Massengill, P. Dodd, M. Shaneyfelt, J. Felix, J. Schwank, N. Haddad, R. Lawrence, J. Bowman, and R. Conde, “Impact of ion energy and species on single event effects analysis,” *IEEE Trans. Nucl. Sci.*, vol. 54, pp. 2312–2321, Dec 2007.
- [55] K. Warren, B. Sierawski, R. Reed, R. Weller, C. Carmichael, A. Lesea, M. Mendenhall, P. Dodd, R. Schrimpf, L. Massengill, T. Hoang, H. Wan, J. D. Jong, R. Padovani, and J. Fabula, “Monte-carlo based on-orbit single event upset rate prediction for a radiation hardened by design latch,” *IEEE Trans. Nucl. Sci.*, vol. 54, pp. 2419–2425, Dec 2007.
- [56] K. Pomorski and J. Dudek, “Nuclear liquid-drop model and surface-curvature effects,” *Phys. Rev. C*, vol. 67, p. 044316, Jan 2003.
- [57] B. A. Brown and B. H. Wildenthal, “Status of the nuclear shell model,” *Ann. Rev. Nucl. Part. Sci.*, vol. 38, pp. 29–66, Jan 1988.
- [58] G. R. Satchler, “Introduction to nuclear reactions,” *John Wiley & Sons*, 1980.
- [59] S. Mongelli, J. Maiorino, S. Anefalos, A. Deppman, and T. Carluccio, “Spallation physics and the ads target design,” *Bra. J. of Phys.*, vol. 35, no. 3B, pp. 894–897, 2005.
- [60] W. G. Lynch, “Nuclear fragmentation in proton- and heavy-ion-induced reactions,” *Annual Review of Nuclear and Particle Science*, vol. 37, no. 1, pp. 493–535, 1987.

- [61] V. Viola, K. Kwiatkowski, L. Beaulieu, D. Bracken, H. Breuer, J. Brzychczyk, R. de Souza, D. Ginger, W.-C. Hsi, R. Korteling, T. Lefort, W. Lynch, K. Morley, R. Legrain, L. Pienkowski, E. Pollacco, E. Renshaw, A. Ruangma, M. Tsang, C. Volant, G. Wang, S. Yennello, and N. Yoder, “Light-ion-induced multifragmentation: The isis project,” *Physics Reports*, vol. 434, no. 1-2, pp. 1 – 46, 2006.
- [62] A. V. Prokofiev, “Compilation and systematics of proton-induced fission cross-section data,” *Nuclear Instruments and Methods in Physics Research Section A: Accelerators, Spectrometers, Detectors and Associated Equipment*, vol. 463, no. 3, pp. 557 – 575, 2001.
- [63] V. Karnaukhov, “Nuclear multifragmentation and phase transitions in hot nuclei,” *Physics of Particles and Nuclei*, Jan 2006.
- [64] N. A. Dodds, “Charge generation by secondary particles from nuclear reactions in back end of line materials,” *Master’s Thesis*, Dec 2009.
- [65] J. Ziegler, “Srim-2003,” *Nuclear Inst. and Methods in Physics Research*, Jan 2004.
- [66] P. E. Dodd, F. W. Sexton, and P. S. Winokur, “Three-dimensional simulation of charge collection and multiple-bit upset in si devices,” *IEEE TRANSACTIONS ON NUCLEAR SCIENCE*, vol. 41, pp. 2005–2017, Dec 1994.
- [67] J. Allison *et al.*, “Geant4 developments and applications,” *Nuclear Science, IEEE Transactions on*, vol. 53, pp. 270–278, Feb 2006.
- [68] M. H. Mendenhall and R. A. Weller, “A probability-conserving cross-section biasing mechanism for monte-carlo variance reduction with application to geant4,” *Nucl. Inst. Meth. Phys. Res. A*, vol. 667, pp. 38–43, Jan 2012.
- [69] M. Sabra, R. Weller, M. Mendenhall, R. Reed, M. Clemens, and A. Barghouty, “Validation of nuclear reaction codes for proton-induced radiation effects: The case for cem03,” *IEEE Trans. Nucl. Sci.*, vol. 58, no. 6, pp. 3134 – 3138, 2011.
- [70] M. S. Sabra, M. A. Clemens, R. A. Weller, M. H. Mendenhall, A. F. Barghouty, and F. B. Malik, “Validation of nuclear reaction models of 180mev proton-induced fragmentation of ^{27}Al ,” *Nucl. Inst. Meth. Phys. Res., B*, vol. 269, pp. 2463–2468, Nov 2011.
- [71] S. Mashnik, A. Sierk, K. Gudima, and M. Baznat, “Cem03 and laqgsm03—new modeling tools for nuclear applications,” *J. Phys: Conf. Ser.*, vol. 41, pp. 340–351, Jan 2006.
- [72] K. Niita, T. Sato, H. Iwase, H. Nose, and H. Nakashima, “Phits—a particle and heavy ion transport code system,” *Rad. Meas.*, vol. 41, pp. 1080–1090, Jan 2006.

- [73] S. G. Mashnik, “Validation and verification of mcnp6 against intermediate and high-energy experimental data and results by other codes,” *International Conference on Mathematics and Computational Methods Applied to Nuclear Science and Engineering (M&C 2011) Rio de Janeiro, RJ, Brazil, May 8-12, 2011*, pp. 1–15, Nov 2011.
- [74] R. A. Reed, P. W. Marshall, H. S. Kim, P. J. McNulty, B. Fodness, T. M. Jordan, R. Reedy, C. Tabbert, M. S. T. Liu, W. Heikkila, S. Buchner, R. Ladbury, and K. A. LaBel, “Evidence for angular effects in proton-induced single-event upsets,” *IEEE Trans. Nucl. Sci.*, vol. 49, pp. 3038–3044, Dec 2002.
- [75] A. Tipton, X. Zhu, H. Weng, J. Pellish, P. Fleming, R. Schrimpf, R. Reed, R. Weller, and M. Mendenhall, “Increased rate of multiple-bit upset from neutrons at large angles of incidence,” *IEEE Trans. Dev. Mat. Rel.*, vol. 8, no. 3, pp. 565 – 570, 2008.
- [76] T. Merelle, F. Saigne, B. Sagnes, G. Gasiot, P. Roche, T. Carriere, M.-C. Palau, F. Wrobel, and J.-M. Palau, “Monte-carlo simulations to quantify neutron-induced multiple bit upsets in advanced srams,” *IEEE Trans. Nucl. Sci.*, vol. 52, pp. 1538–1544, Dec 2005.
- [77] A. N. Smirnov, V. P. Eismont, N. P. Filatov, J. Blomgren, H. Conde, A. V. Prokofiev, P.-U. Renberg, and N. Olsson, “Measurements of neutron-induced fission cross sections for 209bi, natpb, 208pb, 197au, natw, and 181ta in the intermediate energy region,” *Phys. Rev. C*, vol. 70, p. 054603, Nov 2004.
- [78] N. F. Haddad, A. T. Kelly, R. K. Lawrence, B. Li, J. C. Rodgers, J. F. Ross, K. M. Warren, R. A. Weller, M. H. Mendenhall, and R. A. Reed, “Incremental enhancement of seu hardened 90 nm cmos memory cell,” *IEEE Trans. Nucl. Sci.*, vol. 58, pp. 975–980, Jun 2011.
- [79] E. Normand, “Extensions of the burst generation rate method for wider application to proton/neutron-induced single event effects,” *IEEE Trans. Nucl. Sci.*, vol. 45, no. 6, pp. 2904 – 2914, 1998.
- [80] M. Chadwick, P. Oblozinsky, M. Herman, N. Greene, R. McKnight, D. Smith, P. Young, R. MacFarlane, G. Hale, S. Frankle, A. Kahler, T. Kawano, R. Little, D. Madland, P. Moller, R. Mosteller, P. Page, P. Talou, H. Trellue, M. White, W. Wilson, R. Arcilla, C. Dunford, S. Mughabghab, B. Pritychenko, D. Rochman, A. Sonzogni, C. Lubitz, T. Trumbull, J. Weinman, D. Brown, D. Cullen, D. Heinrichs, D. McNabb, H. Derrien, M. Dunn, N. Larson, L. Leal, A. Carlson, R. Block, J. Briggs, E. Cheng, H. Huria, M. Zerkle, K. Kozier, A. Courcelle, V. Pronyaev, and S. C. vanderMarck, “Endf/b-vii.0: Next generation evaluated nuclear data library for nuclear science and technology,” *Nucleolar Data Sheets*, vol. 107, pp. 2931–3060, Dec 2006.

- [81] G. Gasiot, D. Giot, and P. Roche, “Multiple cell upsets as the key contribution to the total ser of 65 nm cmos srams and its dependence on well engineering,” *IEEE Trans. Nucl. Sci.*, vol. 54, no. 6, pp. 2468 – 2473, 2007.
- [82] N. Bohr *Phil. Mag.*, vol. 21, p. 212, 1913.
- [83] H. Bethe *Ann. Physik*, vol. 5, p. 325, 1930.
- [84] H. Bethe *Z. Phys.*, vol. 76, p. 293, 1932.
- [85] J. F. Ziegler, J. P. Biersack, and U. Littmark, *The Stopping and Range of Ions in Solids*, vol. 1. 1985.
- [86] U. Fano, “Penetration of protons, alpha particles, and mesons,” *Annual Review of Nuclear Science*, Jan 1963.
- [87] S. Ahlen, “Theoretical and experimental aspects of the energy loss of relativistic heavily ionizing particles,” *Rev. of Mod. Phys.*, vol. 52, no. 1, pp. 121–173, 1980.
- [88] P. Sigmund, R. Bimbot, H. Geissel, H. Paul, and A. Schinner, “Stopping of ions heavier than helium,” *ICRU Report 73. J. of the ICRU*, vol. 5, pp. 1–235, 2005.
- [89] H. Bishel *Phys. Rev. A*, vol. 41, p. 3642, 1990.
- [90] F. Allegrini, D. J. McComas, D. T. Young, J.-J. Berthelier, J. Covinhes, J.-M. Illiano, J.-F. Riou, H. O. Funsten, and R. W. Harper, “Energy loss of 1-50 keV h, he, c, n, o, ne, and ar ions transmitted through thin carbon foils,” *Review of Scientific Instruments*, vol. 77, no. 4, p. 044501, 2006.